2019

A Numerical Study of Granular Dam-Break Flows

Nuttita Pophet
University of Mississippi

Recommended Citation

Pophet, Nuttita, "A Numerical Study of Granular Dam-Break Flows" (2019). *Electronic Theses and Dissertations*. 1665.
https://egrove.olemiss.edu/etd/1665

A NUMERICAL STUDY OF GRANULAR DAM-BREAK FLOWS

A Dissertation
presented in partial fulfillment of requirements
for the degree of Doctor of Philosophy
in the National Center for Computational Hydroscience and Engineering
The University of Mississippi

by

Nuttita Pophet

May 2019

ABSTRACT

Granular flows are mass movements of mixtures of solid particles and interstitial fluid. Examples include landslides, debris flows and tailings dam-break flows. These types of flows are often catastrophic events, and cover a wide range of phenomena of interest to both scientists and engineers. The mechanical properties of granular materials and the hydraulic behavior of the flows originate from solid and fluid phases, their distribution and interaction. Understanding the behavior of these types of flows and developing reliable predictive models are important.

A new coupled model is developed in this work to be applied to the study of dam-break flows of solid-fluid mixture. The model is built by coupling solid-fluid mixture flow model, and porous media flow model. The emphasis of this study is on both dry granular flows where the interstitial fluid plays no significant role in the dynamic of the flows, and saturated granular flows. The homogeneous theory is adopted for the dry cases while the mixture model is used for the saturated cases. In the mixture model, a separate response between the solid and fluid phases is accounted for. The response from the fluid phase is obtained from the porous flow model through a coupling algorithm. New modules for constitutive relations and boundary conditions are developed together with a library for manipulating a simulation run. The model is validated through comparisons of the numerical results with laboratory experiments. The reproduction of granular dam-break flows is analysed and discussed.

Keyword: Numerical modeling, Dam-break flow, Granular Flow, Solid-fluid mixture

DEDICATION

My dissertation is dedicated to my loving parents, my sister and my family for their endless love, support and encouragement that becomes an invaluable source of strength along the duration of this study.

ACKNOWLEDGEMENTS

I would like to sincerely express my deepest appreciation to my advisor Dr. Mustafa Altinakar for his generous advice, encouragement and the support provided to me throughout my Ph.D. study at NCCHE. It was an excellent opportunity for me to work with him. I also express my appreciation to Dr. Yafei Jia, Dr. Robert Holt and Dr. Yavuz Ozeren for providing valuable comments and suggestions for my research and for serving as a member of my dissertation committee.

I would also like to thank my colleague Luc Rébillout for his help and support with experimental data. I would also like to acknowledge the friendship and help from NCCHE scientists, staffs and students. I will always gratefully remember Dr. Jack Asavanant and Dr. Mansour Ioualalen, my former supervisors, for introducing me to this field. Without their support and encouragement, I would have never come to this point.

Finally, I would like to thank NCCHE to have provided the financial support for my Ph.D. study and dissertation research.

TABLE OF CONTENTS

LIST OF FIGURES

LIST OF TABLES

LIST OF SYMBOLS

c	Cohesion
$\boldsymbol{D}$	Strain rate tensor
F_d	Drag Force
F_s	Surface tension force
$\boldsymbol{g}$	Gravitational acceleration vector
h	Pressure head
I	Inertial number
K	Hydraulic conductivity
K_r	Relative hydraulic conductivity
K_s	Saturated hydraulic conductivity
n	Porosity
$\boldsymbol{n}$	Unit vector normal
p	Pressure
p^*	Modified pressure
p_a	Atmospheric pressure
p_w	Water pressure
Q_s	Volumetric source/sink
S_s	Specific storage
S_w	Saturation ratio
$\boldsymbol{T}$	Stress tensor
$\boldsymbol{T}'$	Diffusion stress tensor

$\boldsymbol{T}_f$	Stress tensor of liquid phase
$\boldsymbol{T}_s$	Stress tensor of solid phase
t	Time
$\boldsymbol{u}$	Velocity vector
$\boldsymbol{u}_f$	Fluid velocity
$\boldsymbol{u}_s$	Particle velocity
V	Volume
V_f	Volume of fluid
$\boldsymbol{x}$	Position vector
η_{eff}	Effective viscosity
γ	Scalar function
κ	Curvature
μ	Coefficient of friction
μ_2	Dynamic friction angle
μ_s	Static friction angle
ϕ	Repose angle
ϕ_w	Volume fraction of water phase
ϕ_s	Volume fraction of solid phase
ρ	Density
ρ_f	Density of fluid
ρ_m	Mixture density
ρ_s	Density of solid particles

σ	Stress tensor
$\sigma\prime$	Effective stress
σ_n	Normal stress
τ	Shear stress
θ	Moisture content
θ_r	Residual moisture content
θ_s	Saturated moisture content

CHAPTER 1

INTRODUCTION

Granular flows, driven by gravity force, are mass movements of mixtures of solid particles and interstitial fluid. Examples include landslides (Yin et al. [90]), debris flows (Elverhøi et al. [16]; Iverson [37]), and tailings dam-break flows (Jeyapalan et al. [45]; Kossoff et al. [47]; Rico et al. [76]), for which the interstitial fluid is water and/or air. These types of flows can be extremely destructive for human lives and infrastructure. Understanding the dynamic behavior of these types of flows, and developing reliable predictive models are important.

The development of numerical models for granular flows centers around three main focuses: choice of a level of approximation of the flow field and pressure field in the model, choice of coupling between solid and fluid phases, and choice of a rheological model or a constitutive equation. Bulk behavior of granular flows such as front velocities, runout distances and deposition patterns has been extensively studied using numerical models based on different levels of simplification which may be broadly classified as: (i) depth-averaged models (Fraccarollo et al. [23]; George and Iverson [24]; Iverson [38]; Naef et al. [64]; Pouliquen and Forterre [72]); and (ii) full momentum balance 2D (vertical) or 3D models (Armanini [1]; Ionescu et al. [36]; Lagrée et al. [48]; Savage et al. [78]). For the depth-averaged models, due to depth integration of the equation of motion, vertical components of the flow field are neglected. The experimental data suggests that the replacement of the vertical distribution of velocity by a depth averaged velocity and the omission of vertical velocities does not reflect true flow behavior and may lead to incorrect predictions in regions of strong vertical velocity gradients. Moreover, because such models ignore the velocity component normal to the bed, they can account for solid-solid and solid-fluid interaction effects only in a rudimentary way (Iverson [38]).

Based on the level of coupling between solid and fluid phases, theoretical models can be categorized into: homogeneous flow models, mixture models and multiphase models (Manninen et al. [59]). Homogeneous flow models treat the mixture as a single-phase homogeneous material, and employ a non-Newtonian rheological model to incorporate the effect of solid-solid and solid-fluid interactions (Berzi et al. [4]). The rheology models adopted range from visco-plastic (Bingham [6]) to collisional regime (Bagnold [3]). However, as emphasized by Meng and Wang [60], although such simple models can describe the dynamic behavior of the mixture to some extent, they are unable to account for complex interactive coupling between the solid and fluid phases or the dynamic behavior of each phase.

In the multiphase models, the momentum and continuity equations of each phase are solved separately (e.g., Armanini [1]). Coupling is achieved through the pressure and inter-phase exchange coefficients. When there is a wide distribution of the particulate phase, or when the inter-phase laws are unknown or their reliability can be questioned, the mixture models is a good substitute for the multiphase approach (Fluent [20]). In the mixture model, the continuity and momentum equations for the mixture are solved together and the momentum equation contains an additional term representing the effect of velocity differences between the phases. Thus, this model can be used to simulate solid-fluid flows where the phases, move at different velocities, but assume a local equilibrium over short spatial length scale. In this way, the model can incorporate a separate response from the interstitial fluid and the solid phase.

Choice of a constitutive equation is an important consideration when modeling granular flows. Unlike Newtonian fluid, which is well described by the Navier-Stokes equations, no constitutive law can reproduce the diversity of behavior observed with a cohesionless granular material (Forterre and Pouliquen [22]). This difficulty originates from fundamental characteristics of granular matter such as negligible thermal fluctuation, highly dissipative interactions, and a lack of separation between the microscopic grain scale and the macroscopic scale of the flow (Goldhirsch [26]). As a result, granular flows are often divided into three regimes and the appropriate constitutive equation is chosen based on the flow regime. In a quasi-static regime, the deformations are very slow and the particles interact by frictional contacts. The most frequently adopted constitutive relation for the quasi-static regime is the shear rate-independent models based on Mohr-Coulomb (M-C) theory. A grain-inertia regime is the regime where the flow is very rapid and dilute, and the particles interact by collisions. The shear rate-dependent relationships are mostly based on the extension of the kinetic theory. In an intermediate regime, the material is dense but still flows like a liquid, the particles interacting with each other both by collision and friction. The so-called $\mu(I)$-rheology has been developed for this regime (MiDi [63]).

One of the greatest challenges in modeling granular-flow behavior involves flows of partially saturated grain-fluid mixtures. For example, a mass failure occurs in a partially saturated material, or even for a mass failure occurring in a saturated soil, a partially saturated mixture state can also develop during its motion due to substantial differences between velocities of the solid and fluid phases. These phenomena can be observed in both experiments and field observations. Watanabe [86] suggested the occurrence of an unsaturated layer in debris flow in laboratory flume experiments, especially for steep channels. Imaizumi et al. [35] observed some partly unsaturated debris flows in the upper Ichinosawa catchment, indicating the need to consider this unsaturated condition. Although a number of numerical models have been developed to describe granular flow behavior, they focus on either dry granular flows or flows of saturated grain-fluid mixtures. When these models are applied to simulate flow of partially saturated mixture, a non-physical result may arise with unrealistic grain concentration (Meng et al. [61]). Therefore, more sophisticated models are needed to simulate flows with variable saturation.

Most numerical studies on granular dam-break flows have focused on validation of numerical scheme by comparing simulation results with experimental works. In the comparison, some discrepancies may occur due to effects of gate motion and removal speeds. In experiments, the instantaneous dam-break is assumed by moving the gate with a removal time small enough not to significantly disturb the initial instants of the dam-break flow (Ferreira Aleixo et al. [18]). When the gate removal is considered instantaneous, the effect of a moving gate on experimental results can be neglected. However, as pointed out by Ye et al. [89] that even if the experiments follow the criterion of sudden removal, there still exists difference between numerical and experimental results. During the release time, the gate prevents the materials above the lip of the gate from moving forward. Meanwhile, the upward moving gate exert a strong shear force at the interface between the gate and the impounded material. The gate motion has seldom been considered in past studies (Ye et al. [89]).

1.1 Objectives of this work

In this PhD dissertation, the main focus is on the development of a coupled numerical model for partially saturated dam-break flows of grain-fluid mixture. To accomplish this, the three-dimensional model for grain-fluid mixture flow is coupled with the model for porous media flow. Both dry and saturated granular flows are investigated in this study. In dry granular flow, the interstitial fluid (air) plays no significant role in the dynamics of the flow. Thus, this type of flow can be described as single-phase, and the homogeneous theory is adopted in this study. The Coulomb-type model and the μ(I) rheological model are chosen for constitutive relations. For saturated granular flow, the dynamics of the flow depends partly on the interstitial fluid and grain-fluid interactions are important. The mixture theory is adopted in this case. Compared to the homogeneous model, the momentum equation in the mixture theory has an additional term accounted for velocity difference between the phases. The constitutive relation used in this model is the extended Coulomb-type model which is analogous to the Terzaghi's principle where the normal stress is decomposed as an effective stress and pore fluid pressure. This pore pressure is given by the porous flow model. In this way, the mixture model and the porous model are coupled, and they exchange necessary information. The coupled model is built on the open-source finite-volume platform OpenFOAM, which provides a library of numerical schemes necessary for the discretizations. Figure 1.1 shows the flowchart of this coupled model. To investigate the efficiency and accuracy of the coupling technique, the developed model is verified by experimental data of granular dam-break flows. It is noted that the terms solid, particle, and grain are used interchangeably in this dissertation.

1.2 Contributions of the present study

This study provides the following novel contribution to the field of granular flow and porous media flow:

- The coupled solver between the mixture model (*interFoam*) and the porous model (*porousInterFoam*) is developed in OpenFOAM. The coupled algorithm allows the model to account for a separate response between the solid and fluid phases. The coupled model is validated using laboratory experiments of Rébillout et al. [74].

- The Coulumb-type, the extended Coulomb-type and the $\mu(I)$ rheological models are implemented in OpenFOAM. These models are employed in *interFoam* solver to describe solid-solid and solid-fluid interactions in simulations of dry and saturated granular dam-break flows. The models are tested against experimental works of Rébillout et al. [74], Evangelista et al. [17], and Mangeney et al. [58].

- The influence of the gate motion on the dam-break flow is considered in this study. In order to accomplish this task, a python library is developed to track the movement of the gate and the cells that contribute the flow of mixture. The influence of the gate speed on dry granular dam-break flows is investigated in experimental works of

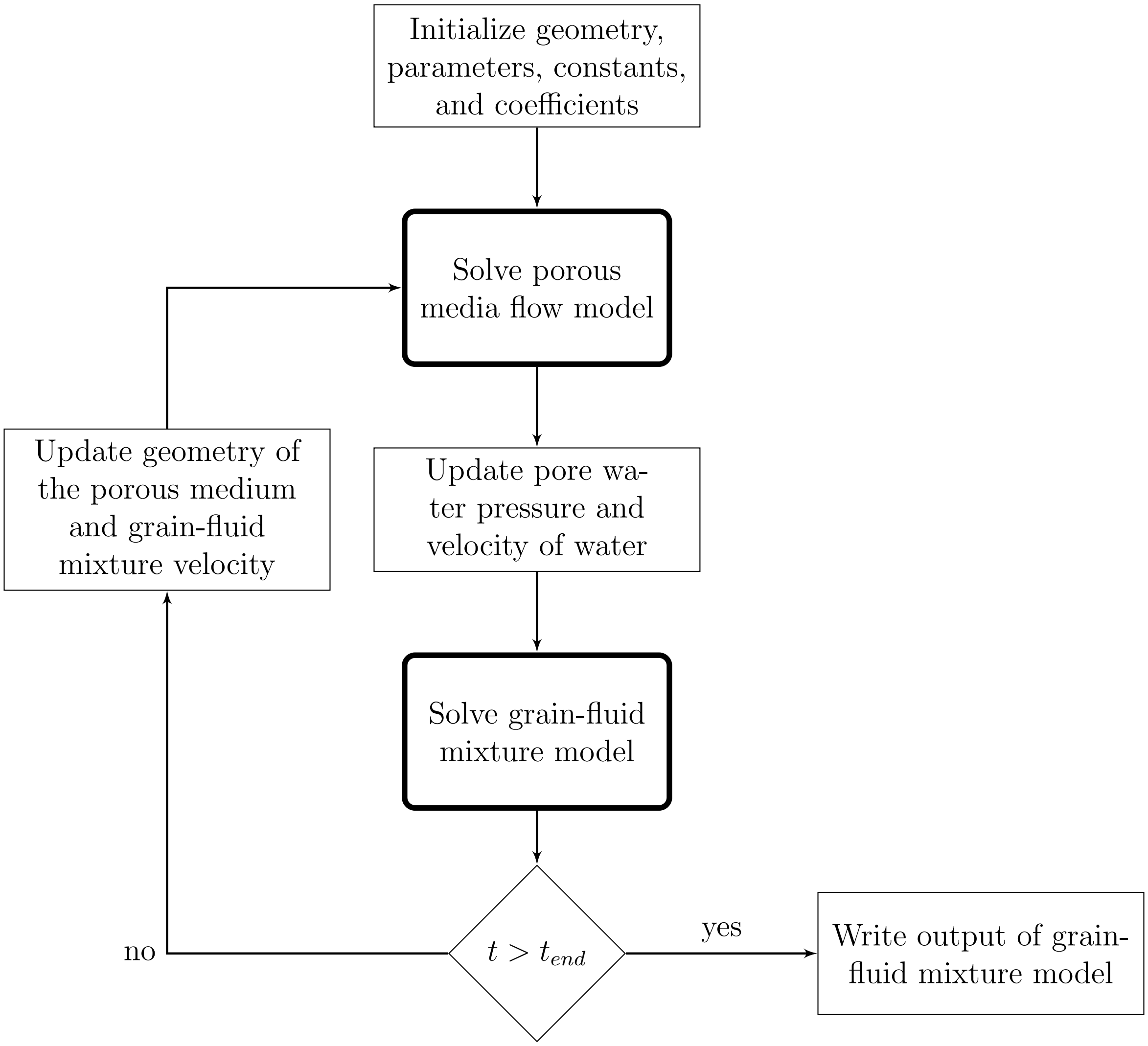

Figure 1.1: Flowchart of the coupled model.

Rébillout et al. [74] and Mangeney et al. [58].

- The *porousInterFoam* solver is modified by improving the way a porous zone is defined in the computational domain. In the original version of the solver, the porous zone is defined by a cell zone. This makes it difficult when dealing with a deforming porous medium. The modified *porousInterFoam* solver enables a simulation with deformable medium and is used to couple with the mixture model to study saturated granular dam-break flows.

- Two new boundary conditions are implemented in OpenFOAM: seepage and Coulomb slip. The seepage boundary condition is used in *suGWFoam*, a solver for variably saturated porous media flows. The Coulomb slip boundary condition is used in the mixture model.

1.3 Thesis outline

The remainder of this dissertation is organized as follows. Chapter 2 presents a literature review and describes the past and recent works on numerical simulation of granular flows and porous media flows. Chapter 3 presents finite volume discretization in OpenFOAM. In Chapter 4, the study of dry granular flow and the influence of gate motion is presented. The study of porous media flows is presented in Chapter 5. In Chapter 6, the development of the coupled numerical model and simulation results are presented. Finally, Chapter 7 provides summary, conclusion and future research.

CHAPTER 2

LITERATURE REVIEW

This chapter presents a comprehensive review of existing granular-flow models. The basic theories and concepts used in the models are described briefly. The description of flows in porous media is presented. Past attempts to investigate the influence of gate removal speeds to dam-break flows are also presented.

2.1 Physical concepts of grain-fluid mixture flows

2.1.1 Flow classification

Classifications of sediment-water mixture are generally based on type of material, movement mechanism, and concentration of sediment. These criteria can be obtained from direct observations, experimental process evaluations, morphological analysis of deposits, physical models or theoretical studies [52]. Mainali and Rajaratnam [57] followed classification given by Pierson and Costa [70] and Varnes [84]. The classification is depicted in 2.1. The sediment water flows can be grouped into three main bands: (i) ordinary streamflow, (ii) hyperconcentrated flow, and (iii) granular flow. Streamflow is, in the strict sense, water and entrained sediment and air flowing as a multiphase flow. For low sediment concentration, there is little interaction between particles and the flow behaves essentially as Newtonian fluid. When the concentration of suspended particles increases, the interactions are therefore no longer negligible. According to Beverage and Culbertson [5], hyperconcentrated flows are referred to mean flows with sediment concentrations by volume of 20-60% and have a mea-

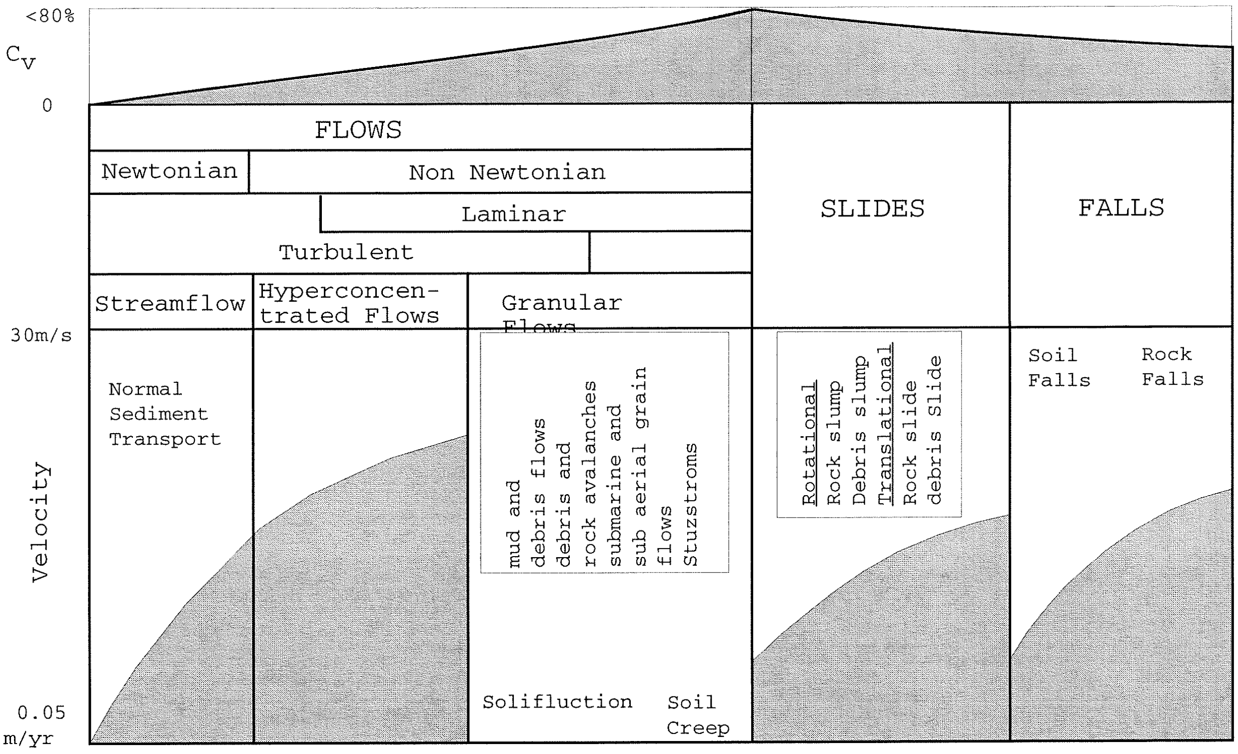

Figure 2.1: General classification of sediment gravity transport (picture taken from Mainali and Rajaratnam [57]).

surable but rather low yield stress. They still flow like non-Newtonian liquids. Granular flows possesses high concentrations of solids. The mixture may be in a saturated or unsaturated or dry state. In the unsaturated state, it may be partially dry with air filling some of its voids. In the saturated case, water can drain freely during continuous deformation. Any excess pressure is, therefore, immediately dissipated and interstitial fluid pressure is no longer greater than the hydrostatic pressure. The entire weight of the granular mass is sustained by contacts or collisions (Lorenzini and Mazza [52]).

2.1.2 Forces acting on particles

2.1.2.1 Particle/particle forces

In dry granular flows, particles interact via contact forces including collisions and long-lasting contacts. In dilute granular flows, energy dissipation occurs primarily via binary collisions. Unlike collision of molecules, a collision of two macroscopic grains is inelastic and thus dissipates energy (Delannay et al. [12]). In contrast, in dense granular flows, the collisions among particles are not instantaneous, but become long lasting and could involve various particles at the same time. In this situation, particles dissipate energy via enduring contacts which involve primarily solid friction.

2.1.2.2 Fluid/particle forces

When an interstitial fluid presents, particles are subjected to additional forces (Delannay et al. [12]). These fluid-particle forces can be divided into five main contributions: buoyancy force, local fluid acceleration force, drag force, virtual mass force, and lift force. Among these contributors, the buoyancy and drag forces are usually dominant.

There are three different definitions of the buoyancy force for fluid-particle system (Jamshidi and Mazzei [41]). The first definition considers the force to be equal to the weight of the fluid displaced by the particles. This definition is in line with the Archimedes principle. The second definition relates the force to the effective stress tensor of the fluid phase while the third definition, often found in the literature, retains only the isotropic part of the effective fluid stress tensor. These definitions lead to different values of the buoyancy force. However, the total fluid-particle interaction force needs to be calculated correctly. Hence, models that use different definition of the buoyancy force also need to use different expressions for the complementary force that makes up the overall fluid-particle interaction force.

In the presence of an interstitial fluid, a particle undergoes a fluid resistance force which is opposite to its relative motion (Delannay et al. [12]). This drag force, F_d, can be expressed as:

$$F_d = C(u_f - u_s) \tag{2.1}$$

where u_s and u_f are the velocities of the solid and fluid. The factor C depends on various parameters such as the particle Reynolds number and the local solid volume fraction.

2.2 Regimes of granular flow

A granular flow is a multiphase process, where momentum transport is mainly due to the dynamics of grains rather than to interstitial fluid (if present). A continuous approach is widely adopted to treat this type of flow, and in the last decades most efforts have been spent to determine the rheological laws governing these materials. A granular flow can undergo different rheological behavior, depending on the type of interactions occurring among particles. By considering the work of Lois et al. [51], three main regimes of granular flow have been identified.

- Quasi-static regime

  A quasi-static regime is a regime where particle concentration is high, when particles approach the random packing fraction, moving at very low shear rate. In this situation, particles remain stuck closely together and transfer of momentum originates mainly from prolonged and multi-grain contacts (Lorenzini and Mazza [52]). The stresses are therefore not governed by the applied strain, but mainly by the peripheral stresses. Granular mixtures in this category show the typical properties of a plastic material. When sufficient stress is applied to a granular mass such that the frictional bonds are broken, the mass starts to flow (Mainali and Rajaratnam [57]). This flow, mainly confined to shear bonds along the shear plane, involves multi-particle blocks moving relative to one another. This slow deformation maintained for a long period of time. Particles are close together and interact mainly through prolonged and multi-grain contacts.

  A large number of constitutive relations have been proposed to account for the mechanic behavior of the granular media in the quasi-static regime. A concept of describing the yielding of granular materials as a friction process is widely adopted. Granular materials tend to follow the Mohr-Coulomb criteria defined by:

$$\tau = c + \sigma_n \tan\phi \tag{2.2}$$

where τ is the shear stress, c is the cohesion, σ_n is the normal stress, and ϕ is the angle of internal friction. The first term on the right is the cohesion and the second term describes the friction resistance.

A water-saturated granular material is a two-phase material, with a separate response from the interstitial fluid and the solid phase. This leads to decomposing the normal stress as an effective stress σ' and pore water pressure p_w.

$$\sigma' = \sigma_n - p_w \tag{2.3}$$

In this case, the normal stress (σ_n) in equation 2.2 is replaced by the effective stress (σ'). This decomposition is know as Terzaghi's effective-stress principle (Terzaghi [82]). The most important aspect of this principle is that the shear resitance (τ) of saturated granular material decreases linearly with increasing pore pressure (p_w). Therefore, the ability of saturated granular material to resist shear is dependent on the state of pore pressure.

- Grain inertia regime

  In contrast to the quasi-static regime, when concentration is low and deformation is rapid, momentum is mainly transferred by particle collision (Lorenzini and Mazza [52]). Friction plays minor role. In this situation, particles tend to dispersed throughout the entire depth. This flow regime is termed the collisional regime, completely dynamic regime or the grain inertia regime. Most widely adopted concept for this regime is the analogy between the molecules of gases and particles in granular flows, where both constituents are free to move in every direction. An extension to the kinetic theory for dense gases (Jenkins and Savage [43]) has been developed for flows in this regime.

- Intermediate regime

  In this regime, the material is dense but still flows like a liquid. Particles interact with each other both by collision and friction. One of the most adopted models in the intermediate regime is the so-called $\mu(I)$ rheology proposed by Jop et al. [46]. The $\mu(I)$ model was derived by a scaling analysis of a compilation of experimental data obtained for granular flows in different configurations. It obtained a wide success among the scientific community for its simplicity and adaptability. Details of the $\mu(I)$ model will be introduced in Section 4.4.

2.3 Past attempts in modelling granular flows

The modeling effort of granular flows has its origins in two distinct tradition of science (Pitman and Le [71]). The first one is the pioneering work of Savage and Hutter [79] and the second point of departure is the mathematical and engineering work on particle-fluid flows (Jackson [40]).

In the pioneer work, Savage and Hutter [79] derived depth-averaged equations of motion for dry granular material flowing down an incline. These equations are simply shallow water or Saint-Venant equations. The granular material was described as frictional and modelled using a Coulomb-type friction law with a constant friction coefficient. The Savage-Hutter model was later extended to two dimension (Hutter et al. [32]), and suggested by Hutter and Koch [34] to extend to quasi-three dimensional basal surface. These approach has been further applied to study granular flows in simple situations such as flow along inclines and even some geophysical granular flow events (Gray et al. [27]; Pudasaini and Hutter [73]: Patra et al. [69]). Later, Hutter [33] examined the appropriateness of these models for various types of geophysical flows.

In the presence of interstitial fluid, the behavior of flows is altered and should be included in the constitutive behavior of the flowing material. Iverson [38] generalized the one-phase dry granular flow model of Savage and Hutter [79] to account for the presence of pore fluid at equilibrium pressure. This model was further developed by Iverson and Denlinger [39] into the coulomb mixture model, which can simulate grain-fluid flows from initiation to stopping stage without redefinition of rheological model. George and Iverson [24] considered effects of pore-pressure feedback accompanying debris deformation by formulating a new, depth-averaged mathematical model that simulate coupled evolution of granular dilatancy, solid and fluid volume fractions, pore fluid pressure, and flow depth and velocity during all stages of flow motions. Their numerical simulations match experimental data reasonably well.

Following the mathematical and engineering work on particle-fluid flows, granular flows are considered as a multiphase system of a mixture of solid, liquid and gas phases. If the flow phenomena are dominated by one phase, multiphase flow can be described as single phase flow and all effects of the secondary phases are neglected. However, if the secondary phases have an influence on the dynamic behavior of the mixture, they cannot be ignored. Depending on the level of coupling between the phases, the modelling approaches can be classified into homogeneous flow models, mixture models and multiphase models (Manninen et al. [59]). Combination of these models are also possible. In these models, each phase is usually treated as an inter-penertrating continuum with a phase volume fraction, which is analogous to the concept of assigning porosity in flow through a porous medium.

The homogeneous flow models are the simplest and most common formulations of the hydrodynamics of a mixture which refers to a motion of the center of mass of the system (Manninen et al. [59]). In these homogeneous flow models, the phases are strongly coupled. All phases are assumed to move at the same velocity. In the mixture models, gravity and centrifugal forces tend to cause velocity differences. A number of models have been developed based on the assumption of local equilibrium. However, when the phases are weakly coupled and there are regions of sudden acceleration, local equilibrium assumption cannot be established. In this situation, the full multiphase model consists of the continuity and momentum equations for each phase and the phase interactions are accounted for by interphase transfer terms. It should be noted that although the full multiphase equations are more advanced, the uncertainties in the closure relations can make them less reliable than simpler models. For this reason, the homogeneous models or the mixture models should be used whenever possible.

The governing equations of the homogeneous model and the mixture model are presented in Section 2.4. In this study, the homogeneous model is used to study dry granular dam-break flows presented in Chapter 4 and the mixture model is used to study saturated granular dam-break flows presented in Chapter 6.

2.4 Mass and momentum balances for granular flows

The main problem in studying solid-fluid mixture is to identify the constitutive relationship that describes the fluxes of mass, momentum and energy and to understand the mechanism that govern stress development (Lorenzini and Mazza [52]). There are two main approaches used to represent motion in granular flow studies: one assumes the hypothesis of granular flows as a homogeneous mixture and the other keeps the solid and liquid phases distinct and assumes a two-phase mixture. The balance equations of mass and momentum in each approach are presented below.

2.4.1 Mass and momentum balances for homogeneous mixtures

(Lorenzini and Mazza [52]) derived the mass and momentum conservation for a homogeneous liquid-grain flows as follow:

$$\bigtriangledown \cdot \mathbf{u} = 0 \tag{2.4}$$

$$\frac{\partial \rho_m \mathbf{u}}{\partial t} + \bigtriangledown \cdot (\rho_m \mathbf{u}\mathbf{u}) = \rho_m \mathbf{g} + \bigtriangledown \cdot \boldsymbol{T} \tag{2.5}$$

where $\mathbf{u}$ is the velocity vector, $\mathbf{g}$ is the gravitational acceleration vector, $\boldsymbol{T}$ is the stress tensor, p is pressure, and ρ_m is the density of the mixture with

$$\rho_m = \phi_s \rho_s + \phi_f \rho_f \tag{2.6}$$

where ϕ_s and ϕ_f are the volume fractions of the solid and liquid phases, and ρ_s and ρ_f are the density of the solid particles and the interstitial fluid.

2.4.2 Mass and momentum balances for two-phase mixture

The mass and momentum balance equations of a granular/debris flow can be borrowed, by making only minor modification, from the continuous theory of two-phase mixtures (Atkin and Craine [2]). Following this rule, the mass and momentum conservation equations for the granular flow solid and liquid constituents are separated but strongly coupled. Angular momentum equations and balances of thermodynamic energy are unnecessary by assuming all stress tensors is symmetric and the mixture is isothermal. The mass conservation equations (Iverson [38]) for the solid and fluid constituents are,

$$\frac{\partial(\rho_s \phi_s)}{\partial t} + \bigtriangledown \cdot (\rho_s \phi_s \mathbf{u}_s) = 0 \tag{2.7}$$

$$\frac{\partial(\rho_f \phi_f)}{\partial t} + \bigtriangledown \cdot (\rho_f \phi_f \mathbf{u}_f) = 0 \tag{2.8}$$

where $\mathbf{u}_s$ and $\mathbf{u}_f$ are the velocity of the solid and liquid phases. Equations 2.7 and 2.8 are coupled because the volume fractions of the solid and fluid constituents must obey $\phi_s + \phi_f = 1$. The momentum conservation equations are,

$$\frac{\partial \rho_s \phi_s \mathbf{u}_s}{\partial t} + \bigtriangledown \cdot (\rho_s \phi_s \mathbf{u}_s \mathbf{u}_s) = \rho_s \phi_s \mathbf{g} + \bigtriangledown \cdot \boldsymbol{T}_s - \boldsymbol{F} \tag{2.9}$$

$$\frac{\partial \rho_f \phi_f \mathbf{u}_f}{\partial t} + \bigtriangledown \cdot (\rho_f \phi_f \mathbf{u}_f \mathbf{u}_f) = \rho_f \phi_f \mathbf{g} + \bigtriangledown \cdot \boldsymbol{T}_f + \boldsymbol{F} \tag{2.10}$$

where $\boldsymbol{T}_s$ and $\boldsymbol{T}_f$ are the stress tensors of the solid and liquid phases, and $\boldsymbol{F}$ is the interaction force per unit volume that results from momentum exchange between the solid and fluid constituents.

Addition of equations 2.7 and 2.8 leads to the equivalent mass conservation equation of the mixture,

$$\frac{\partial \rho}{\partial t} + \bigtriangledown \cdot (\rho \mathbf{u}) = 0 \tag{2.11}$$

where ρ is the mixture density and u is the velocity defined by

$$\rho = \phi_s \rho_s + \phi_f \rho_f \tag{2.12}$$

$$\mathbf{u} = \frac{\phi_s \rho_s \mathbf{u}_s + \phi_f \rho_f \mathbf{u}_f}{\rho} \tag{2.13}$$

From these definitions, the mixture velocity is that of the center of mass (not volume) of a mixture volume element. Addition of equations 2.9 and 2.10 yields a momentum equation for the bulk mixture,

$$\frac{\partial \rho \mathbf{u}}{\partial t} + \bigtriangledown \cdot (\rho \mathbf{u}\mathbf{u}) = \rho \mathbf{g} + \bigtriangledown \cdot (\boldsymbol{T}_s + \boldsymbol{T}_f + \boldsymbol{T}') \tag{2.14}$$

where

$$\boldsymbol{T}' = -\phi_s \rho_s (\mathbf{u}_s - \mathbf{u})(\mathbf{u}_s - \mathbf{u}) - \phi_f \rho_f (\mathbf{u}_f - \mathbf{u})(\mathbf{u}_f - \mathbf{u}) \tag{2.15}$$

represents the contribution linked to the relative motion of the solid and fluid constituents in relation to the mixture as a whole. From mathematical point of view (Lorenzini and Mazza [52]), this term ($\boldsymbol{T}'$) results from the convective terms of equations 2.9 and 2.10 summed together do not give $\bigtriangledown \cdot \mathbf{u}\mathbf{u}$, the convective acceleration of the mixture. From physical point of view, $\boldsymbol{T}'$ indicates that the stresses in a two-phase mixture flow are more complex than those obtained by adding $\boldsymbol{T}_s$ and $\boldsymbol{T}_f$. The term $\bigtriangledown \cdot \boldsymbol{T}'$ is called the diffusion stress term (Manninen et al. [59]) representing the momentum diffusion due to the relative motions. Without this term, the mixture momentum equation 2.14 reduces to that of the homogeneous mixture equation 2.5 by substituting $\boldsymbol{T}_s + \boldsymbol{T}_f$ with $\boldsymbol{T}$.

2.5 Influence of gate removal in dam-break flows

In theoretical studies of dam-break flows, the solution is obtained under the assumption of instantaneous release of impounded material. In experimental studies, a release system is designed to remove gate in extremely short time to approximate the sudden release in theoretical studies. According to Lauber and Hager [49], the gate removal time has to be less than $\sqrt{2}\sqrt{(}h_0/g)$ to be considered as instantaneous. Under this condition, the effect of a moving gate on experimental results can be neglected.

Ozeren et al. [68] experimentally investigated dam-break flow characteristics at various gate removal speeds. Their experimental setup consisted of a reservoir and a downstream flood plain, which were separated by a sliding gate. The sliding gate was pulled upwards by a weight-dropping mechanism. The removal speed of the gate was controlled by setting different initial heights of the weight. They found that the results obtained for the gate removal analysis were in agreement with Lauber and Hager's criterion. That is there was no significant difference observed in terms of positive wave front propagation for gate removal speeds greater than approximately 1.4 m/s ($t \approx \sqrt{2}\sqrt{(}h_0/g)$). However, in numerical simulations, as pointed out by Ye et al. [89] that even if the experiments follow the criterion of sudden removal, there still exists difference in the flow behavior between numerical and experimental results. Therefore, the influence of the gate should be considered in numerical simulations of dam-break flows.

Ye et al. [89] investigated the gate motion effect on dam-break flows of water using a constrained interpolation profile (CIP)-based method to solve the Navier-Stokes equations with the free surface boundary condition to deal with the water-air-gate interactions. The movable gate was simulated by an immersed boundary method. Their numerical results shows that the gate motion has a significant influence in the water collapse process and cannot be neglected in the study of dam break. Ionescu et al. [36] investigated the influence of the gate on granular dam-break flows by simulating the gate removal with a constant lifting velocity measured in the experiments. The gate was considered as a simple rigid boundary under an assumption of no penetration condition and the friction between the gate and the granular material was neglect. They found that the gate has a significant impact on the flow dynamics of granular dam-break flow. However, the gate influence disappears in the deposit phase for the cases where the gate removal is not too slow.

2.6 Porous media flows

A porous medium is a multiphase system consisting of a solid phase and one or more fluid phases occupying the pore space. The different phases are separated from each other by abrupt interfaces. A porous medium is microscopically quantified by the geometrical characteristics of the void space and by relevant state variables for each phase. Fluid flow in porous media is of great importance in many areas of science and engineering including environmental engineering and groundwater hydrology.

According to Nield and Bejan [65], the treatment of flow through a porous medium depends largely on the scale in consideration. At a small scale (pore-scale), when a few small pores are considered, it is convenient to use the conventional fluid mechanics approach to describe the flow phenomenon in the pore space. However, when the scale is large (macro-scale), it is impractical to solve the microscopic conservation equations inside the pores due to the inability to describe the complex structure of the porous material. A preferable approach (Hassanizadeh and Gray [29]) is to average the microscopic equations inside the porous medium over a representative elementary volume (REV), the size of which is assumed to be much larger than the characteristic size of pore structures but much smaller than the domain. The details given below are limited to a macroscopic (continuum) approach and a porous medium consisting of three phases: a solid matrix phase (s), a liquid water phase (w) and an air phase (a).

2.6.1 Darcy's law

For a single-phase flow in porous media, the flow behavior is described by Darcy's law which can be written as

$$-\bigtriangledown p = \frac{\mu \boldsymbol{v}}{k} \tag{2.16}$$

where $\bigtriangledown p$ is the pressure gradient, μ is the viscosity, $\boldsymbol{v}$ is the superficial velocity, and k is the permeability. Combining Darcy's law with the law of conservation of mass, the governing equation is obtained.

$$-\bigtriangledown \cdot \left(\frac{k}{\mu} \bigtriangledown p\right) = 0 \tag{2.17}$$

Darcy's law can predict flow behavior properly when the flow is dominated by viscous effect or at low flow rates ($Re < 1$), when the flow rate and the pressure gradient have a linear relationship. However, as the flow rate (Re) increases, inertial forces become more significant. Many attempts have been made to correct the Darcy equation. Various terms, such as non-Darcy flow, turbulent flow, inertial flow, high velocity flow, etc., have been used to describe this behavior (Firoozabadi and Katz [19]). Forchheimer [21] added a second order of the velocity term to represent the microscopic inertial effect, and corrected the Darcy equation into the Forchheimer equation:

$$-\bigtriangledown p = \frac{\mu \boldsymbol{v}}{k} + \beta \rho \boldsymbol{v}^2 \tag{2.18}$$

where β is the non-Darcy coefficient and ρ is the fluid density.

For a two-phase flow, the description of Darcy's law is extended to a set of 2 equations for water phase and air phase. The Darcy equation can be written for each phase by introducing relative permeabilities and different pressure fields for the two fluids.

$$\boldsymbol{v}_w = -\frac{k_{r,w} k}{\mu_w} \bigtriangledown p_w \tag{2.19}$$

$$\boldsymbol{v}_a = -\frac{k_{r,a} k}{\mu_a} \bigtriangledown p_a \tag{2.20}$$

where $k_{r,w}$ and $k_{r,a}$ are the (phenomenological) relative permeabilities for water and air. The relative permeabilities inserted in Darcy's law are due to the fact that the flow of a fluid depends on the local configuration of the other fluid. These relative permeability functions are dependent on the saturation of their phase. Since the air saturation $S_a = 1 - S_w$, the saturation dependence can be expressed via the water saturation S_w only, i.e. $k_{r,w} = k_{r,w}(S_w)$ and $k_{r,a} = k_{r,a}(S_w)$. These functions are usually determined from experimental data, with different values in the case of drainage when compared to those in the case of imbibition. There exist several models proposed to describe these relationships and the best known functions are proposed by Brooks and Corey [8] and Van Genuchten [83].

Compared to a single-phase flow, two-phase flow is subject to viscous and capillary forces. The capillary forces arise from the microscopic curvature between the air and water phases. On the macroscopic scale, this curvature does not exist as individual pores are not visible in the continuum approach (Cense and Berg [10]). To stay consistent in the macroscopic view, the relation of phase pressure of air and water is defined as the capillary pressure-saturation function

$$p_c = p_a - p_w = p_c(S_w) \tag{2.21}$$

which is dependent on the water saturation S_w. From the detailed study of capillary effects, it is found that the fluid saturations have a strong influence on the capillary pressure. Many scientists came up with ideas to describe capillary pressure-saturation relationship. The best known relationships for air-water could be found in the literature from Brooks and Corey [8] and Van Genuchten [83].

2.6.2 Richards' equation

The two-phase model presented in the previous subsection can be simplified under the so-called passive gas phase assumption which assumes that the flow of air is negligible, and the pore air remain constantly at the ambient external atmospheric pressure throughout the partially saturated domain. That is, a constant atmospheric value is assumed for the air pressure. This assumption neglects the pressure gradient in the air phase and reduces the two-phase flow model to a single equation for the water phase. The combination of Darcy's law with an adapted law of conservation of mass yields

$$\frac{\partial \theta}{\partial t} - \bigtriangledown \cdot \left(\frac{k_{r,w} k_w}{\mu_w} \bigtriangledown p_w \right) = 0, \tag{2.22}$$

where θ is the volume metric water content. This equation is known as Richards' equation (Richards [75]). In order to complete Richards' equation to a closed system, a relation between pressure and saturation has to be defined and can be written as in equation 2.21. For convenience, it is often assumed that the reference atmospheric pressure $p_a = 0$ and equation 2.21 can be written as

$$p_c = p_a - p_w = -p_w. \tag{2.23}$$

For the values of the water pressure (p_w) smaller than the negative of the air entry pressure (p_e), $p_w < -p_e$, the water saturation (S_w) and relative permeability ($k_{r,w}$) can be computed from the analytical models (e.g. Brooks and Corey model or van Genuchten model). For the values of the water pressure which are larger than the negative of the air entry pressure, $p_w > -p_e$, the water saturation and water permeability are constant and equal to their maximum values. Richards' equation can be written in three forms: the pressure head-based form, the saturation based form, and the mixed form formulation. Each form has its strengths and drawbacks. The three different forms of the equations and the discussion on selecting a suitable form for a specific problem are presented in Section 5.2.

2.6.3 Volume-averaged Navier-Stokes equation for flow in porous media

The above mentioned mass conservative models encompasses only the mass balance equations for the fluid phases (water and/or air), and omits the transient term and the nonlinear inertial term in the momentum equation. Therefore, there is no mechanism to treat the unsteady evolution of flow fields, and the flow Reynolds number must be kept sufficiently small (Wang et al. [85]). Moreover, only flow problems inside the porous medium can be investigated. Therefore, a new model that is valid for pure fluid and moving porous regions in the entire domain is desired.

Several approaches based on Navier-Stokes equations have been purposed to model porous media flow. Differences are found in the different terms considered in the Navier-Stokes equation including choices of the superficial velocity. In addition to the phase averaged velocity (also called Darcy velocity) generally used for porous media flow, the intrinsic phase averaged velocity is also adopted in the literature. Yang et al. [88] used the intrinsic phase averaged velocity in the macroscopic equation, while employed the phase averaged velocity in the flow resistance term. In general, it is not clear which kind of volume-averaged velocity should be used for the case of moving porous medium. Recently, Wang et al. [85] derived the macroscopic equations for the incompressible flow in a moving porous medium and investigated Galilean invariance of the equations both with the intrinsic phase averaged velocity and the phase averaged velocity. The results show that the commonly used phase averaged velocity cannot serve as the superficial velocity. The intrinsic phase averaged velocity should be chosen for moving porous systems. In this study, the macroscopic equations derived by Wang et al. [85] are adopted and details of the equations are presented in Section 5.1.

CHAPTER 3

FINITE VOLUME DISCRETIZATION IN OPENFOAM

OpenFOAM, acronym for Open Source Field Operations and Manipulations, is an open source platform for solving partial differential equations using finite volume method on unstructured meshes. It incorporates a tensorial approach to computational continuum mechanics based on the object-oriented programming technique (Weller et al. [87]). It can be used to create a solver for complex physics problems that can be mathematically described in the form of differential equations with suitable boundary and initial conditions. In this Chapter, the general governing equation and finite volume discretization in OpenFOAM are presented. It is noted that, in this dissertation, OpenFOAM version 3.0.1 is used.

3.1 The general governing balance equation

The standard form of the transport equation for a scalar property ϕ is given by:

$$\underbrace{\frac{\partial}{\partial t}\rho\phi}_{\text{time accumlation}} = -\underbrace{\bigtriangledown\cdot(\rho \mathrm{U}\phi)}_{\text{convective transport}} + \underbrace{\bigtriangledown\cdot(\Gamma\bigtriangledown\phi)}_{\text{diffusive transport}} + \underbrace{S_\phi}_{\text{source terms}} \tag{3.1}$$

where ρ is the density, U is the velocity vector, Γ is the diffusion coefficient, that can be a scalar or a vector, and S_ϕ is any kind of sources or sinks that influence the quantity of ϕ. Deriving the mass, momentum and other conservative equations can be done by replacing the quantity ϕ by the quantity of interest. The details of derivation of the equations can be found in Holzmann [31].

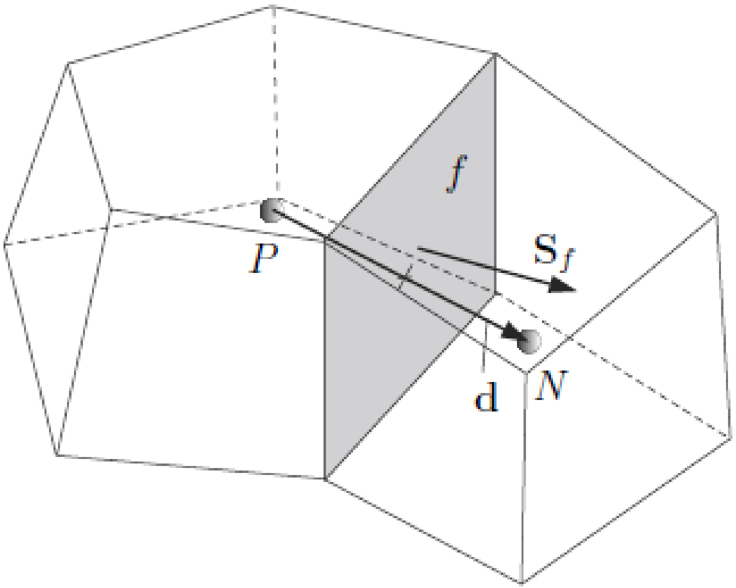

Figure 3.1: Parameters in finite volume discretization, picture taken from OpenFOAM [66].

3.2 Finite volume discretization in OpenFOAM

The finite volume method requires that Equation 3.1 is satisfied over the control volume V_p around the center point P in the integral form (see Figure 3.1):

$$\int_{t}^{t+\triangle t} \left[\frac{\partial}{\partial t} \int_{V_P} \rho \phi dV \right] dt = \int_{t}^{t+\triangle t} \left[- \int_{V_P} \bigtriangledown \cdot (\rho \mathrm{U} \phi) dV + \int_{V_P} \bigtriangledown \cdot (\Gamma \bigtriangledown \phi) dV + \int_{V_P} S_\phi dV \right] dt \quad (3.2)$$

The discretization of Equation 3.2 is presented briefly in details in the following section. More explanation on the discretization can be found in Jasak [42].

3.2.1 Discretization of spatial terms

The discretization of spatial terms can be split into two parts: the transformation of the volume and surface integrals into discrete sums and expressions that give the face values of the variable as a function of cell values. The discretization of the convection term, diffusion term, divergence, gradient and source term is described below.

3.2.1.1 Convection term

The convection term is integrated over a control volume and linearised as follows:

$$\begin{aligned} \int_V \bigtriangledown \cdot (\rho \mathrm{U} \phi)\ dV &= \int_S d\mathrm{S} \cdot (\rho \mathrm{U} \phi) \\ &= \sum_f \mathrm{S}_f \cdot (\rho \mathrm{U})_f \, \phi_f \\ &= \sum_f F \phi_f \end{aligned} \tag{3.3}$$

where F represents the mass flux through the face, $F = S_f \cdot (\rho \mathrm{U})_f$. Equation 3.3 requires the face value of ϕ_f calculated from the values in the cell centers, which can be obtained using a variety of schemes:

Central differencing (CD) is second-order accurate but unbounded

$$\phi_f = f_x \phi_P + (1 - f_x)\, \phi_N \tag{3.4}$$

where $f_x \equiv \frac{f\bar{N}}{P\bar{N}}$ where $f\bar{N}$ is the distance between face f and cell centre N and $P\bar{N}$ is the distance between cell centres P and N.

Upwind differencing (UD) determines ϕ_f from the direction of flow and is bounded at the expense of accuracy

$$\phi_f = \begin{cases} \phi_P & \text{for } F \geq 0 \\ \phi_N & \text{for } F < 0 \end{cases} \tag{3.5}$$

Blended differencing (BD) schemes combine UD and CD in an attempt to preserve both boundedness and accuracy of the solution,

$$\phi_f = (1 - \gamma)\, (\phi_f)_{UD} + \gamma\, (\phi_f)_{CD} \tag{3.6}$$

where γ is the blending coefficient, $0 \leq \gamma \leq 1$. This blending coefficient determines how much numerical diffusion will be introduced. In OpenFoam, there are several implementations of the Gamma differencing scheme to select the blending coefficient γ and it also offers other well-known schemes such as van Leer, SUPERBEE, MINMOD etc.

3.2.1.2 Diffusion term

The diffusion term is integrated over a control volume and linearised as follows:

$$\begin{aligned} \int\limits_V \bigtriangledown\left(\Gamma \cdot \bigtriangledown\phi\right)\, dV &= \int\limits_S d\mathrm{S} \cdot \left(\Gamma \bigtriangledown \phi\right) \\ &= \sum_f \Gamma_f \mathrm{S}_f \cdot \left(\bigtriangledown\phi\right)_f \end{aligned} \tag{3.7}$$

If the mesh is orthogonal, i.e. the length vector $\boldsymbol{d}$ and the face area vector S_f are parallel, the following expression can be used.

$$\mathrm{S}_f \cdot \left(\bigtriangledown\phi\right)_f = \left|\mathrm{S}_f\right| \frac{\phi_N - \phi_P}{|d|} \tag{3.8}$$

In the case of non-orthogonal meshes, an additional explicit term is introduced which is evaluated by interpolating cell centre gradients, themselves calculated by central differencing cell centre values.

3.2.1.3 Divergence

The divergence term for the scalar function ϕ is an explicit term that is distinguished from the convection term. It is not the divergence of the product of a velocity and dependent variable. The term is integrated over a control volume and linearised as follows:

$$\int\limits_V \bigtriangledown \cdot \phi \, dV = \int\limits_S dS \cdot \phi = \sum_f S_f \cdot \phi_f \tag{3.9}$$

3.2.1.4 Gradient

The gradient term for the scalar function ϕ can be evaluated in several ways. The discretization of Gaussian integration is performed by using the standard method of applying Gauss's theorem to the volume integral:

$$\int\limits_V \triangledown\phi \, dV = \int\limits_S dS\phi = \sum_f \phi_f \tag{3.10}$$

where ϕ_f can be evaluated by any face interpolation scheme. The surface normal gradient which is the gradient normal to a surface $n_f \cdot (\triangledown\phi)_f$ can be evaluated at cell faces using the scheme

$$(\triangledown\phi)_f = \frac{\phi_N - \phi_P}{|d|} \tag{3.11}$$

The scheme is analogous to that evaluated for the diffusion discretization scheme, and in the same manner, a correction can be introduced to improve the accuracy of this face gradient in the case of non-orthogonal meshes.

3.2.1.5 Source terms

Source terms for the scalar function ϕ can be specified in 3 ways: explicit, implicit and implicit/explicit. An explicit source term can be incorporated in to an equation simply as a field of values. An implicit source term is integrated over a control volume and linearised by

$$\int\limits_V \rho\phi \, dV = \rho_P V \phi_P \tag{3.12}$$

By using the implicit source term, the coefficient of the diagonal of the matrix is changed. Depending on the sign of the coefficient and matrix terms, this will either increase or decrease diagonal dominance of the matrix. Decreasing the diagonal dominance could cause instability during iterative solution of the matrix equation. Therefore, OpenFOAM provides a mixed source discretization procedure that is implicit when the coefficient is greater than zero, and explicit when the coefficient is less than zero.

3.2.1.6 Time derivative

The temporal derivative $\frac{\partial}{\partial t}$ is usually discretized using a first order or a second order accurate scheme in time. The term is discretized by simple differencing in time using: the unknown value $\phi_n \equiv \phi\left(t + \triangle t\right)$ at the time step that are solving for, the old values $\phi^0 \equiv \phi\left(t\right)$ known value from the previous time step, the old-old values $\phi^{00} \equiv \phi\left(t - \triangle t\right)$ known value from a time step previous to the last.

Euler implicit scheme, that is first order accurate in time:

$$\int\limits_V \frac{\partial \rho \phi}{\partial t}\, dV \approx V \frac{\left(\rho_P \phi_P\right)^n - \left(\rho_P \phi_P\right)^0}{\triangle t} \tag{3.13}$$

Backward differencing scheme, that is second order accurate in time:

$$\int\limits_V \frac{\partial \rho \phi}{\partial t}\, dV \approx V \frac{3\left(\rho_P \phi_P\right)^n - 4\left(\rho_P \phi_P\right)^0 + \left(\rho_P \phi_P\right)^{00}}{2 \triangle t} \tag{3.14}$$

CHAPTER 4

DRY GRANULAR DAM-BREAK FLOWS

This chapter presents the three-dimensional numerical model with InterFOAM. The model solves continuity and momentum equations using finite volume method on a Cartesian grid. The free surface is modeled using the VOF (Volume of Fluid) method with an additional artificial compression term. The constant friction model and the $\mu(I)$ model are described. The numerical model with the developed rheological formulas is tested against three laboratory experiments of dry granular dam-break flows in a rectangular channel on flat and inclined planes. The three experiments use different granular materials: PET pellets (Rébillout et al. [74]), sand (Evangelista et al. [17]), and glass beads (Mangeney et al. [58]). The comparisons of numerical and experimental results are presented. The influence of the gate removal and speeds on dry granular dam-break flows is investigated. A comment on selection of the constant friction and $\mu(I)$ rheology is discussed.

4.1 Governing equations

Granular/debris flows are usually treated as a motion of continuum despite the fact that they contain solid particles. This approximation makes the equations of mass and momentum conservation for granular flows similar to those for the motion of a generic fluid [52]. The governing equations can be written in the differential form as:

Conservation of mass:

$$\bigtriangledown \cdot \mathbf{u} = 0 \tag{4.1}$$

Conservation of momentum:

$$\frac{\partial \rho_m \mathbf{u}}{\partial t} + \bigtriangledown \cdot (\rho_m \mathbf{u}\mathbf{u}) = \rho_m \mathbf{g} + \bigtriangledown \cdot \boldsymbol{\sigma} \tag{4.2}$$

where:

$\mathbf{u}$ is the velocity vector;

$\mathbf{g}$ is the gravitational acceleration vector;

$\boldsymbol{\sigma}$ is the stress tensor. The stress tensor $\boldsymbol{\sigma}$ is generally expressed as $\boldsymbol{\sigma} = -p\mathbf{I} + \boldsymbol{\tau}$; where p is pressure, $\boldsymbol{\tau}$ is the shear stress tensor which is explained in the Appendix A and $\mathbf{I}$ is the unit tensor;

ρ_m is the density of the mixture with

$$\rho_m = (1 - n)\rho_s + n\rho_f \tag{4.3}$$

where n is the porosity, and ρ_s and ρ_f are the density of the solid particles and the interstitial fluid, respectively. For dry granular flow, the interstitial fluid is air. Since the density of air is very small compared to the density of the solid particles, the density of the mixture can be approximated as

$$\rho_m = (1 - n)\rho_s \tag{4.4}$$

4.2 VOF as Interface-capturing methodology

VOF (Volume of Fluid) method of interface-capturing belongs to the Euler-Euler framework where all phases are treated as continuous. The VOF model does not allow the phases to be inter-penetrating. In the VOF method, one momentum equation and one continuity equation are solved for mixture properties without slip velocity, meaning that all field variables are assumed to be shared between the phases. Physical properties of one fluid are calculated as weighted averages based on the volume fraction of the two fluids in one cell. To track the interface between two or more phases, an advection equation for a phase indicator function is solved. In order to obtain a sharp interface the discretization of the indicator function equation is crucial. Different techniques have been proposed for this. The momentum equation solved in the VOF method takes the form

$$\frac{\partial \rho \mathbf{u}}{\partial t} + \triangledown \cdot (\rho \mathbf{u}\mathbf{u}) = - \triangledown p + \rho \mathbf{g} + \triangledown \cdot \boldsymbol{\tau} - F_s \tag{4.5}$$

where F_s is the surface tension force which takes place only at the interface, and equation 4.1 for continuity remains the same. The granular mixture is treated as a non-Newtonian fluid with constant friction or $\mu(I)$ rheology which is explained in section 4.4. The air is modeled as a Newtonian fluid. The stress tensor $\boldsymbol{\tau}$ of equation 4.5 is defined as

$$\boldsymbol{\tau} = \eta(\triangledown \mathbf{u} + \triangledown \mathbf{u}^T) \tag{4.6}$$

where η is the kinematic viscosity of the respective fluid.

The volume of fluid in a cell is computed as $F_{vol} = \gamma V_{cell}$, where V_{cell} is the volume of a computational cell and γ is a scalar function used as the phase indicator. If a cell is completely filled with fluid then $\gamma = 1$ and if it is filled by air then $\gamma = 0$. At the interface the value of γ is between 0 and 1. This scalar function γ can be computed from a separate transport equation that takes the form:

$$\frac{\partial \gamma}{\partial t} + \triangledown \cdot (\gamma \mathbf{u}) = 0 \tag{4.7}$$

The necessary compression of the interface is achieved by introducing an artificial compression term into the phase fraction transport equation as follow:

$$\frac{\partial \gamma}{\partial t} + \triangledown \cdot (\gamma \mathbf{u}) + \triangledown \cdot (\gamma \left(1 - \gamma\right) \mathbf{u}_r) = 0 \tag{4.8}$$

where $\mathbf{u}_r = \mathbf{u}_1 - \mathbf{u}_2$ is the vector of relative velocity between the two fluids and $\mathbf{u}$ is the mean velocity, which is calculated as a weighted average of the velocities of the two phases:

$$\mathbf{u} = \gamma \mathbf{u}_1 + (1-\gamma)\,\mathbf{u}_2 \tag{4.9}$$

The artificial compression term is active only in the interface region due to the term $\gamma\,(1-\gamma)$.

The density at any point in the domain is calculated as a weighted averaged of the volume fraction of the two phases, γ as:

$$\rho = \gamma \rho_1 + (1-\gamma)\,\rho_2 \tag{4.10}$$

The subscripts 1 and 2 denote different fluids.

The surface tension force F_s is computed as:

$$F_s = \sigma \kappa\,(\mathbf{x})\,\mathbf{n} \tag{4.11}$$

where $\mathbf{x}$ is the position vector, $\mathbf{n}$ is the unit vector normal to the interface that can be calculated from $\mathbf{n} = \frac{\bigtriangledown\gamma}{|\bigtriangledown\gamma|}$, and κ is the curvature of the interface that can be calculated from $\kappa\,(\mathbf{x}) = \bigtriangledown\cdot\mathbf{n}$. In the case of granular material, the surface tension term is negligible. Hence, σ is set to zero in this study.

4.3 Final form of the momentum equation

To facilitate a more stable numerical solution, two terms in the momentum equation 4.5 need to be reformulated [77]: the modified pressure and the viscous stress term. The modified pressure is used as a dependent variable to simplify the specification of the pressure boundary conditions. It is defined as:

$$p^* = p - \rho\mathbf{g}\cdot\mathbf{x} \tag{4.12}$$

where p^* is the modified pressure, which is obtained by removing the hydrostatic pressure from the pressure. It is legitimate to do so since the motion of the flow does not depend on the absolute values of the pressure but on its gradient. This change of variable can be accounted for in the momentum equation by taking the gradient of equation 4.12 and substituting the result into the momentum equation. The gradient of 4.12 reads:

$$\begin{aligned} \bigtriangledown p^* &= \bigtriangledown p - \bigtriangledown(\rho \mathbf{g} \cdot \mathbf{x}) \\ &= \bigtriangledown p - \rho \mathbf{g} - \mathbf{g} \cdot \mathbf{x} \bigtriangledown \rho \end{aligned} \tag{4.13}$$

The use of the formulation in equation 4.13 leads to a simpler specification of the pressure boundary condition, and the inclusion of the term $\mathbf{g} \cdot \mathbf{x} \bigtriangledown \rho$ enables efficient numerical treatment of the steep density jump at the interface [77] between the two fluids.

To achieve a more efficient numerical evaluation, the viscous stress is reformulated as

$$\begin{aligned} \bigtriangledown \cdot \boldsymbol{\tau} &= \bigtriangledown \cdot \left(\eta \left(\bigtriangledown \mathbf{u} + (\bigtriangledown \mathbf{u})^T\right)\right) \\ &= \bigtriangledown \cdot (\eta \bigtriangledown \mathbf{u}) + \bigtriangledown \cdot \left(\eta (\bigtriangledown \mathbf{u})^T\right) \\ &= \bigtriangledown \cdot (\eta \bigtriangledown \mathbf{u}) + (\bigtriangledown \mathbf{u}) \cdot \bigtriangledown \eta + \eta \bigtriangledown (\bigtriangledown \cdot \mathbf{u}) \\ &= \bigtriangledown \cdot (\eta \bigtriangledown \mathbf{u}) + (\bigtriangledown \mathbf{u}) \cdot \bigtriangledown \eta \end{aligned} \tag{4.14}$$

The final form of the momentum equation is assembled from equations 4.5, 4.11, 4.13 and 4.14, the momentum equation expressed for the mixture flow is as follows:

$$\frac{\partial \rho \mathbf{u}}{\partial t} + \bigtriangledown \cdot (\rho \mathbf{u} \mathbf{u}) = - \bigtriangledown p^* + \bigtriangledown \cdot (\eta \bigtriangledown \mathbf{u}) + (\bigtriangledown \mathbf{u}) \cdot \bigtriangledown \eta - \mathbf{g} \cdot \mathbf{x} \bigtriangledown \rho + \sigma \kappa \bigtriangledown \gamma \tag{4.15}$$

The present mathematical model is given by the continuity equation **??**, phase fraction equation 4.8 and the momentum equation 4.15.

4.4 Viscous shear stress

The stress tensor $\boldsymbol{\sigma}$ can be written in terms of an effective viscosity as follows:

$$\boldsymbol{\sigma} = -p\mathbf{I} + \boldsymbol{\tau} \tag{4.16}$$

where p is the isotropic pressure, $\mathbf{I}$ is the unit tensor, and $\boldsymbol{\tau}$ is the shear stress tensor,

$$\boldsymbol{\tau} = 2\eta_{eff}(\|\boldsymbol{D}\|, p)\boldsymbol{D} \tag{4.17}$$

with

$$\eta_{eff}(\|\boldsymbol{D}\|, p) = \frac{\mu p}{\|\boldsymbol{D}\|} \tag{4.18}$$

where μ is the analogue of a coefficient of friction, $\boldsymbol{D} = \boldsymbol{D}(\mathbf{u}) = (\bigtriangledown\mathbf{u} + (\bigtriangledown\mathbf{u})^T)/2$ is the strain rate tensor, and $\|\boldsymbol{D}\|$ is second invariant of the strain rate tensor: $\|\boldsymbol{D}\| = \sqrt{2\boldsymbol{D_{ij}}\boldsymbol{D_{ij}}}$.

To write the above expression, a co-linearity between the shear stress and the strain rate tensors is assumed following the work of several previous authors [13, 14, 25]. Within this description, the granular mixture is then described as an incompressible non-Newtonian fluid, with an effective viscosity η_{eff} depending on both the shear rate and the pressure, a signature of the underlying frictional nature of the medium [22]. This description is similar to the one developed in other visco-plastic materials like mud. A flow threshold is given by a frictional Drucker-Prager criterion [15]: $|\boldsymbol{\tau}| > \mu_1 p$ is recovered when $\|D\|$ goes to zero and the viscosity diverges. In this study, the coefficient of friction μ in equation 4.18 is considered as constant (μ) and variable ($\mu(I)$):

- **The constant friction model**

  In the constant friction model, the frictional properties of the flow are related to the internal friction angle ϕ through a constant of proportional $\mu = \tan\phi$.

- **The variable friction $\mu(I)$ model**

  The friction coefficient $\mu(I)$ proposed by Jop et al. [46] can be written as

$$\mu(I) = \mu_s + \frac{\mu_2 - \mu_s}{I_0/I + 1} \tag{4.19}$$

  where μ_s and μ_2 are the static and dynamic angles, respectively. I_0 is a constant dependent on the material properties of the flow. I is known as the inertial number and is defined as

$$I = \frac{\|\boldsymbol{D}\| d}{\sqrt{p/\rho_p}} \tag{4.20}$$

  This number can be interpreted as the ratio between two time scales: the time of the microscopic rearrangements $d/\sqrt{p/\rho}$, where p is the pressure, d is the grain diameter, and ρ_p is the density of the grains and the macroscopic scale of the flow, which is assumed equal to the mean deformation $\|\boldsymbol{D}\|^{-1}$. According to these equations the friction angle increases during the transition from the quasi-static regime ($I \to 0$) to the kinetic regime ($I \gg I_0$). Despite its success, the $\mu(I)$ model has some important limits, which make it weak in situations different from those ones used to derive it [62]. One of them is that the model accounts for the presence of two angles, one of which is the dynamical angle. Physically this parameter depends on the flow-field and is hard to determine. It is not a constant as proposed by the authors.

4.5 Experimental setup

Three independent laboratory studies of dry granular dam-break flows are used to validate the numerical model. The three experiments are different in (i) the granular material, (ii) the initial column height and width, (iii) the slope of the channel, and (iv) the rheological models employed in numerical simulations. The description of the three different settings are given in Table 4.1.

Table 4.1: Experimental description.

Experiments	Rébillout et al. [74]	Evangelista et al. [17]		Mangeney et al. [58]
Granular material	PET pellets	sand (A)	sand (B)	glass beads
Particle diameter (mm)	2.867	0.2	1.6	0.7±0.1
Material density (kg/m^3)	1422	2680	2560	2500
Volume fraction	0.66	0.47	0.57	0.62
Bulk density (kg/m^3)	938	1259.6	1459.2	1550
Repose angle ($^\circ$)	30	36	41	25.5
Channel width (m)	0.5	0.4	0.4	0.1
Initial column height H_0 (m)	0.2, 0.3, 0.4	0.2, 0.3	0.2, 0.3	0.14
Initial column length L (m)	3.24	0.5	0.6	0.2
Aspect ratio (H_0/L)	0.06, 0.09, 0.12	0.4, 0.6	0.33, 0.5	0.7
Channel inclination ($^\circ$)	0	0	0	0, 10, 16, 22
Coefficient of friction	constant	constant	constant	constatn, $\mu(I)$

4.6 Treatment of the moving gate in numerical simulations

In the experiments, a gate is moved upward to release a granular mass. The movement of the gate can be simulated by considering the motion consisting of two stages: acceleration and uniform motion stages and is expressed as (Ye et al. [89]):

$$y(t) = \begin{cases} \frac{1}{2}at^2 & , t \leq t_0 \\ \frac{1}{2}at_0^2 + v_0(t - t_0) & , t > t_0 \end{cases} \tag{4.21}$$

where y is the vertical displacement of the gate, t is the time, v_0 is the velocity of the uniform motion stage, t_0 is the duration of the acceleration stage, and $a = v_0/t_0$ is the acceleration of the gate in the acceleration stage. Figure 4.1 shows vertical displacement of the gate in the experiments conducted by Rébillout et al. [74] and Mangeney et al. [58], and those used in the simulations. The duration of the acceleration stage of $t_0 = 0.013\,s$ (displayed with dash line in Figure 4.1) is chosen to fit the experimental data of Rébillout et al. [74]. The velocity of the uniform motion stage (v_0) is varied as 1.5, 3, 5, and 9 m/s. In the experiments

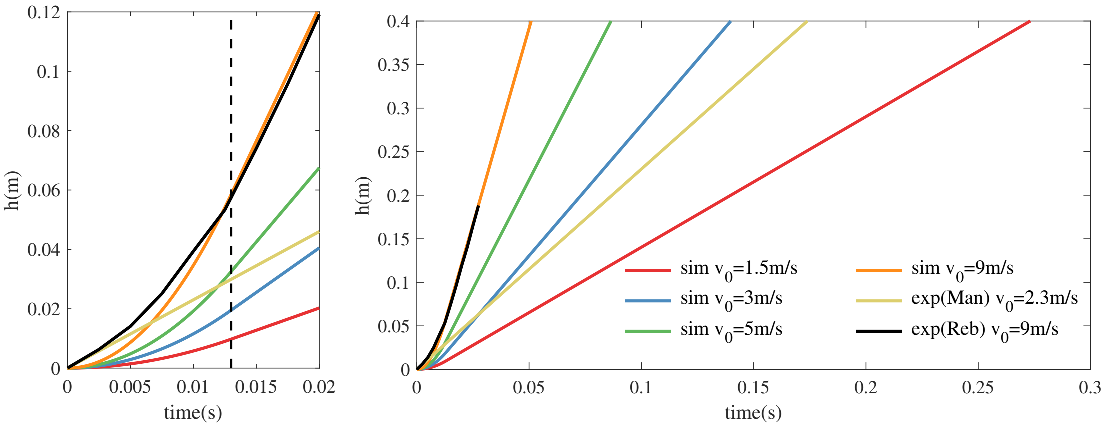

Figure 4.1: Vertical displacement of the gate in the simulations, the experiments by Rébillout et al. [74] (Reb): zoom-in view (left) and full view (right), and the experiments by Mangeney et al. [58] (Man).

conducted by Mangeney et al. [58], according to Ionescu et al. [36], the gate is assumed to move with uniform velocity of $v_0 = 2.3\, m/s$, which is adopted in this study. The summary of simulation settings of the dry granular dam-break flows with and without (sudden release) the gate is given in Table 4.2.

Table 4.2: Simulation settings for the cases with and without the gate.

Experiments	Rébillout et al. [74]	Evangelista et al. [17]	Mangeney et al. [58]
without the gate	✓	✓	✓
with the gate	✓	-	✓
v_0 (m/s)	1.5, 3, 5, 9	-	2.3
t_0 (s)	0.013	-	-
time that the gate completely removed (s)	0.27, 0.13, 0.08, 0.05	-	0.06

In the numerical implementation, the movement of the gate is simulated as a dynamic internal boundary condition. At simulation time $t = 0$, a zero thickness wall or baffle is created using utilities: topoSet and createBaffle in OpenFOAM. At time step $t = t_i$, the position of the gate lip is calculated. If this position passes the lower edge of a cell, a new baffle is created with the baffle position starting from the top edge of the cell as depicted in Figure 4.2. This step is repeated until the gate clears off. These processes are automated during simulations

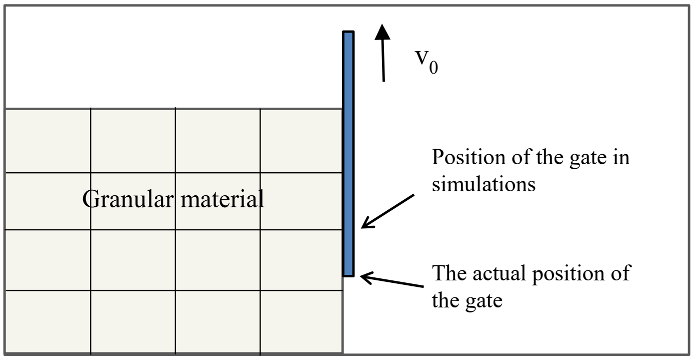

Figure 4.2: Sketch of the gate position in granular dam-break problems.

by using PyFoam utilities. At the upstream surface of the gate, no slip boundary condition is adopted.

4.7 Influence of grid resolution

In the VOF method, the interface region between two phases is typically smeared over a few grid cells and is therefore highly sensitive to grid resolution [11]. To test the sensitivity of the model to grid resolution, simulations with three different cell sizes of 5, 7.5, and 10 mm are performed using experimental setting of Rébillout et al. [74] with the particle diameter of 2.867 mm and the initial column height of 0.4 m. Thus, the cell sizes are about 1.7, 2.6 and 3.5 times the particle diameter. The total numbers of cells for each case are 300×100, 201×67 and 150×50. A time step of 0.0005 s is used for all test cases.

Figure 4.3 shows the granular mass profile for the simulations with different cell sizes. In early state of the flow (t = 0.18 and 0.57 s), a slight difference in height of the granular mass upstream of the gate location is observed, while there is no significant difference downstream of the gate. The final upstream slopes at rest are similar. The downstream surface profiles and the front location are slightly different. The cell size of 7.5 mm is chosen in the subsequent computations if not described otherwise. Figure 4.4 shows the granular mass profile for different volume fractions used to define the interface between air and the granular mass. The higher volume fraction gives the lower height of the profile

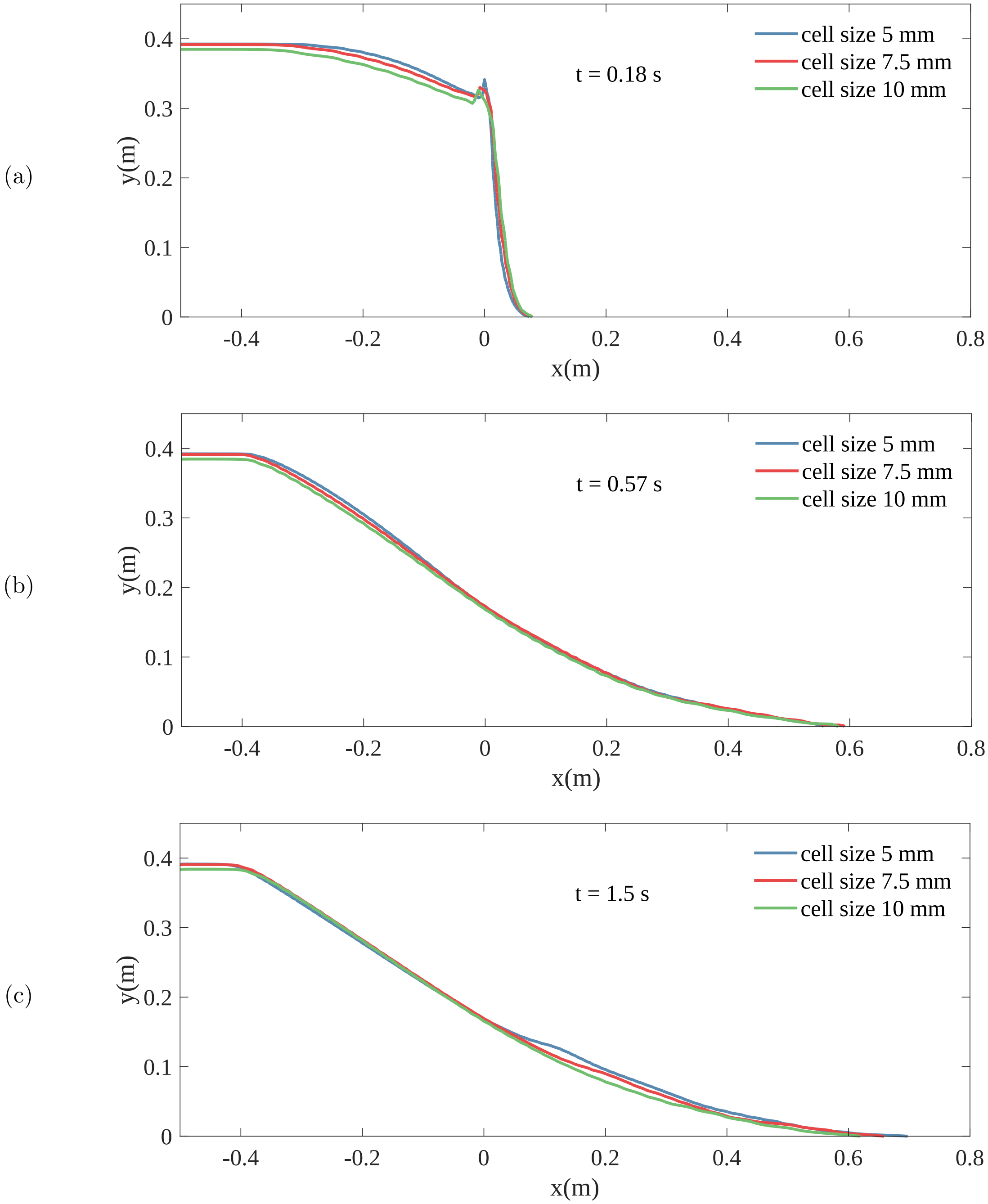

Figure 4.3: Comparison between the simulations with different cell sizes at time 0.18, 0.57 and 1.5 s. Surface is represented by $\gamma = 0.5$.

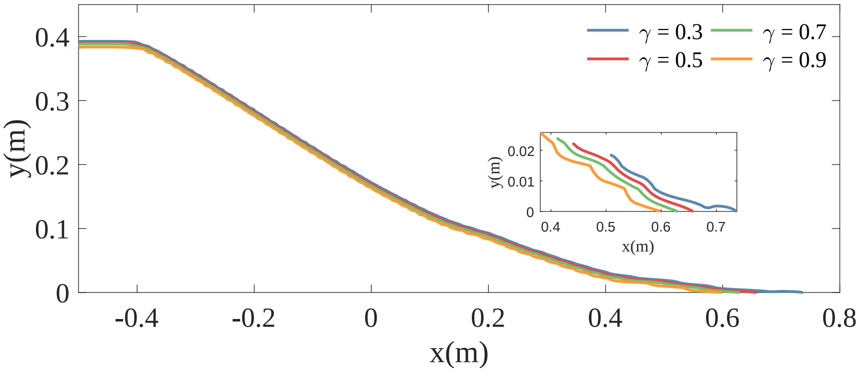

Figure 4.4: Comparison between the simulations with difference volume fractions at the final deposit.

and closer deposit of the front toe. The volume fraction $\gamma = 0.5$ is applied in the subsequent plots.

4.8 Comparisons between numerical simulations and experiments conducted by Rébillout et al. [74]

This section presents simulation results with and without the presentation of the gate movement in comparison with the experiments of Rébillout et al. [74]. In Subsection 4.8.1, the granular mass profiles and velocity fields of the simulations with and without the gate are presented along with experimental results. The initial column height of the granular mass is 0.4 m. The velocity of the gate in the uniform motion stage is $v_0 = 9\,m/s$. Pressure distribution, effective viscosity, and strain rate of the simulation with the gate are presented in Subsection 4.8.2. In Subsection 4.8.3, the granular mass profiles at the final deposit of the simulations with the gate for different initial column heights are presented along with experimental results. In Subsection 4.8.5, the propagation of the front toe for the simulations of 0.4-m initial column height with different gate speeds of 1.5, 3, 5, and 9 m/s and without the gate is presented along with the experimental result. The time step is 0.0005 s and the cell size is 7.5 mm for all cases. The constant friction model with $\mu = 0.56$ is used for all cases.

4.8.1 The granular mass profiles and velocity fields

Figure 4.5 shows the granular mass profile of the experiment with the initial column height of 0.4 m and of the simulations with and without the gate, and the velocity distribution for the simulation with the gate. The colors, representing velocity magnitude, show that the flow is concentrated only in a shallow sub-domain near the free surface as observed in the experiments. This is probably why depth-averaged models do not correctly represent details of the flow in the intermediate phases. In early state of the flow ($t = 0.18$ and $0.28\,s$), the shape of the granular mass with the gate shows better agreement with the experiment than that of the experiment without the gate. At $t = 0.5\,s$, the maximum velocity is concentrated at the front edge of the granular mass with the magnitude of about 1.5 m/s, and the shapes of the granular mass with and without the gate are similar. At $t = 0.75\,s$, the flow occurs only on a top thin layer of the granular mass. The front stops moving in the simulations but the top thin layer of the granular mass is still moving as can be seen with the velocity magnitude. At the final deposit ($t = 1.5\,s$), there is a slight difference between the shapes of the granular mass for the cases with and without the gate. The influence of the gate disappears in the deposition phase. The slopes of the final profile are in good agreement with the experiment.

4.8.2 Pressure distribution, effective viscosity, and strain rate

Figure 4.6 shows pressure distribution, effective viscosity, and strain rate in the granular mass at different times. Figure 4.6(a)-(c) shows that, at $t = 0.18\,s$, pressure varies from almost zero at the interface to about 4000 Pa near the bed, while, at $t = 0.28$ and $0.5\,s$, the maximum pressure near the bed is about 3000 Pa. In the flowing region (see the velocity field in Figure 4.5), the pressure distribution is quite regular with the maximum about 1500 Pa at the interface of the flowing and no-flowing region. Figure 4.6(d)-(f) shows that the effective viscosity varies from almost 0 $Pa \cdot s$ in the flowing region to over 100 $Pa \cdot s$ near the bed and has a similar distribution with the pressure field. In the flowing region, the effective

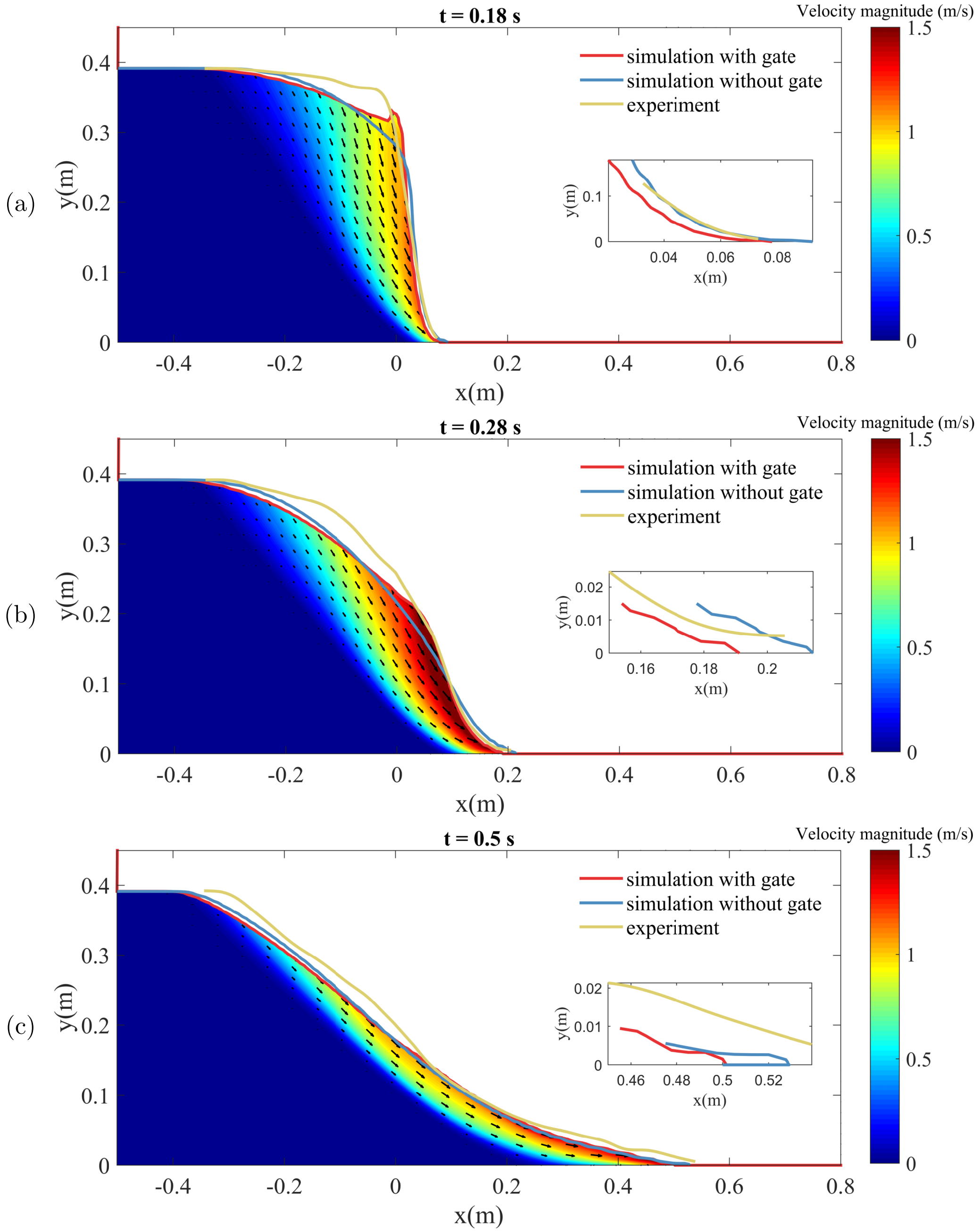

Figure 4.5: Comparison of the granular mass profiles between the experiment by Rébillout et al. [74] and simulations with and without the gate, and velocity magnitude for the simulation with the gate at time 0.18, 0.28, and 0.5 s.

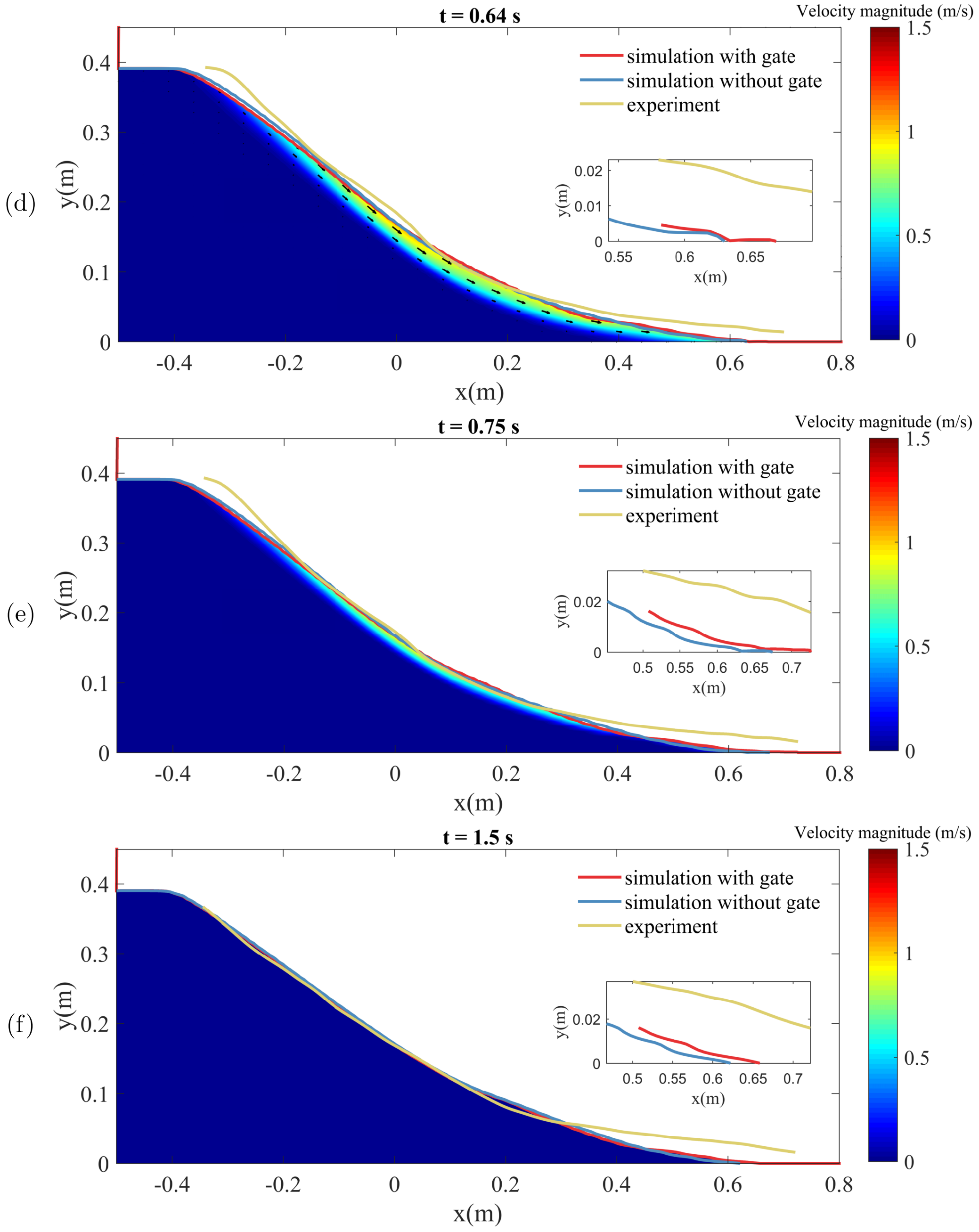

Figure 4.5: Comparison of the granular mass profiles between the experiment by Rébillout et al. [74] and simulations with and without the gate, and velocity magnitude for the simulation with the gate at time 0.64, 0.75 and 1.5 s (cont.)

viscosity is less than 1 $Pa \cdot s$. This small effective viscosity in the flowing region is directly related to the low pressure in this zone (Figure 4.6(a)-(c)). While the pressure and viscosity distributions within the flowing region is quite regular, the strain rate is concentrated near the front and near the bed (Figure 4.6(g)-(i)) with a maximum value above 60 s^{-1}.

In order to describe the flow/no-flow condition, a yield function $F = F(\|\tau\|, p)$ is defined. According to Ionescu et al. [36], F can be written as:

$$F(\|\tau\|, p) = \|\tau\| - \mu p \tag{4.22}$$

where τ is the shear stress, μ is the friction coefficient, p is the pressure, and the fluid is at rest if and only if $F(\|\tau\|, p) \leq 0$. The distribution of the yield function at different times is shown in Figure 4.7. The static/flowing transition is described with the zero contour lines. The zone corresponding to a positive value of the yield function represents the flowing region of the granular mass. It is noted that the positive value of the yield function near the back wall are due to the low pressure in this region. However, there is no flow of the granular material observed as can be seen in the plots of velocity in Figure 4.9.

4.8.3 The granular mass profiles for different initial heights

Figure 4.8 shows the granular mass profiles of the experiments and simulations for different initial column heights. It can be seen that slopes of the final deposits are well captured for all initial heights of 0.2, 0.3 and 0.4 m using one rheological parameter obtained from the experiments. However, there is a lack of similarity of the front between the simulations and experiments, especially for the cases with higher initial heights. This may be due to the no-slip boundary condition imposed at the bottom in the simulations which prevents the granular mass from sliding at the bed near the leading tip of the front.

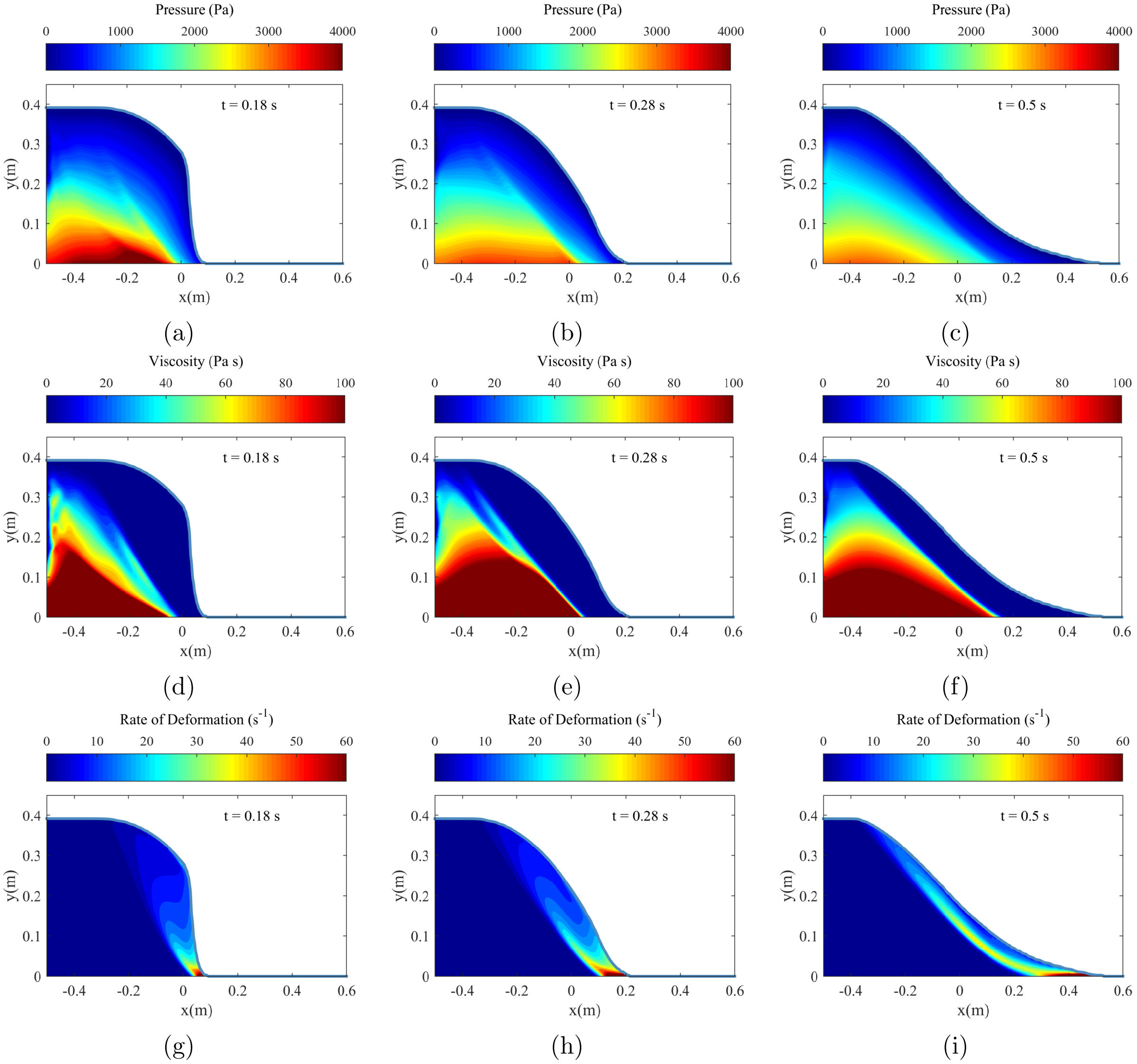

Figure 4.6: Pressure distribution p in Pa, effective viscosity η_{eff} in $Pa \cdot s$, and strain rate $\|\boldsymbol{D}\|$ in s^{-1} at time 0.18, 0.28, and 0.5 s.

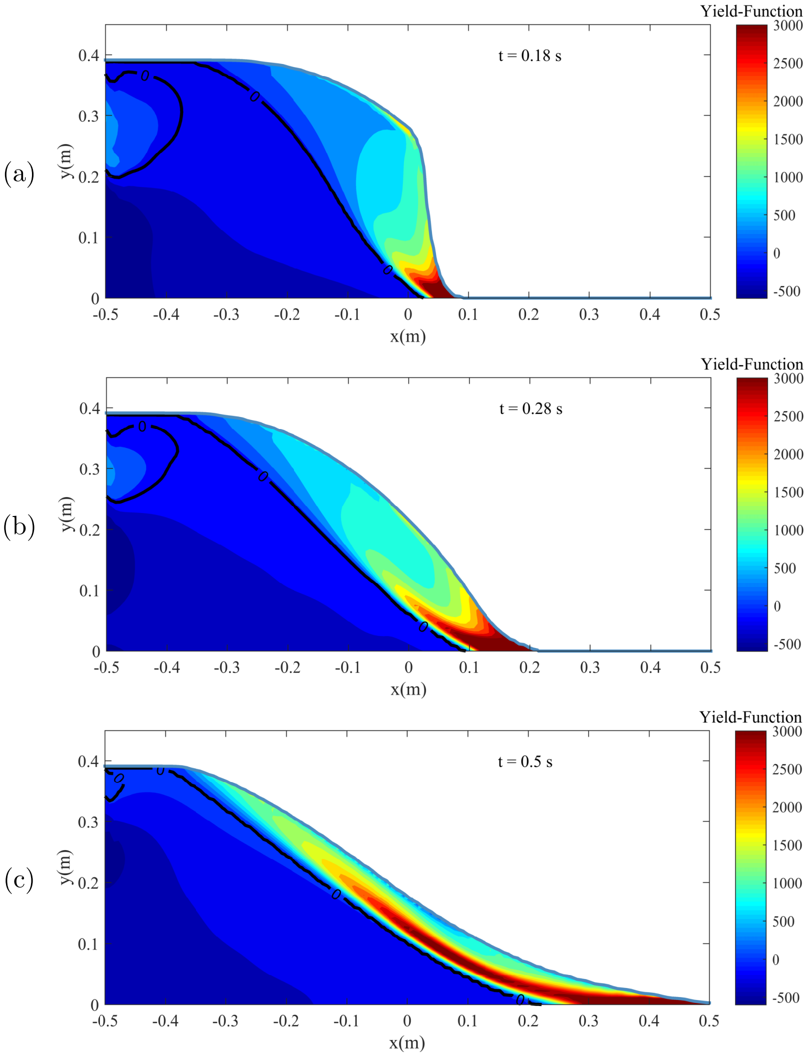

Figure 4.7: The distribution of yield function $F(\sigma) := \|\tau\| - \mu p$.

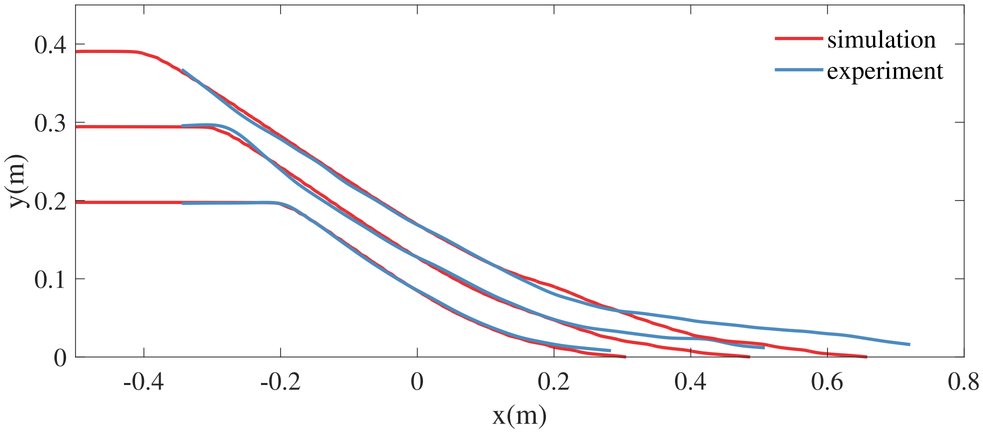

Figure 4.8: Granular mass profile for simulations and experiments conducted by Rébillout et al. [74] with different initial heights at the final deposit.

4.8.4 Velocity fields for the simulations with and without the gate

Figure 4.9 shows velocity magnitudes and velocity vectors for the simulation with (left) and without (right) the gate at different times. The simulation with the gate corresponds to the case with the gate removal speed of uniform velocity of $v_0 = 9\ m/s$ (see Table 4.2). At time $t = 0.02\ s$ (Figure 4.9(a)) where the gate bottom's edge position is at $y = 0.12\ m$, velocity magnitudes are larger for the case without the gate. That is because, for the case without the gate, particles are free to move while, for the case with the gate, about 70% of the column height is still blocked by the gate. At time $t = 0.04\ s$ (Figure 4.9(b)), where the gate bottom's edge position is at $y = 0.3\ m$, velocity magnitudes for the case without the gate are larger and particles are moving downwards. However, for the case with the gate, particles near the gate where $y > 0.2\ m$ are moving upwards as can be seen from the velocity vectors. At time $t = 0.051\ s$, the gate is already cleared off for the simulation with the gate. At later time ($t = 0.1$ and $0.18\ s$), even the directions of the flow in both cases are similar, differences in velocity magnitudes are observed.

4.8.5 Influence of gate removal speed

Figure 4.10 shows the propagation of the front toe for the simulations with different gate speed, without the gate, and the experiment. The leading tip of the front of the granular mass with faster removal case runs ahead of the slower gate motion case. In the slowest removal case, $v_0 = 1.2\,m/s$, the final deposit of the front toe is underestimated while the other three faster removal cases are similar and closer to the experiment. The simulation without the gate, at first, moves as fast as the cases with the gate and the experiment but later slows down and deposits far less than the other cases.

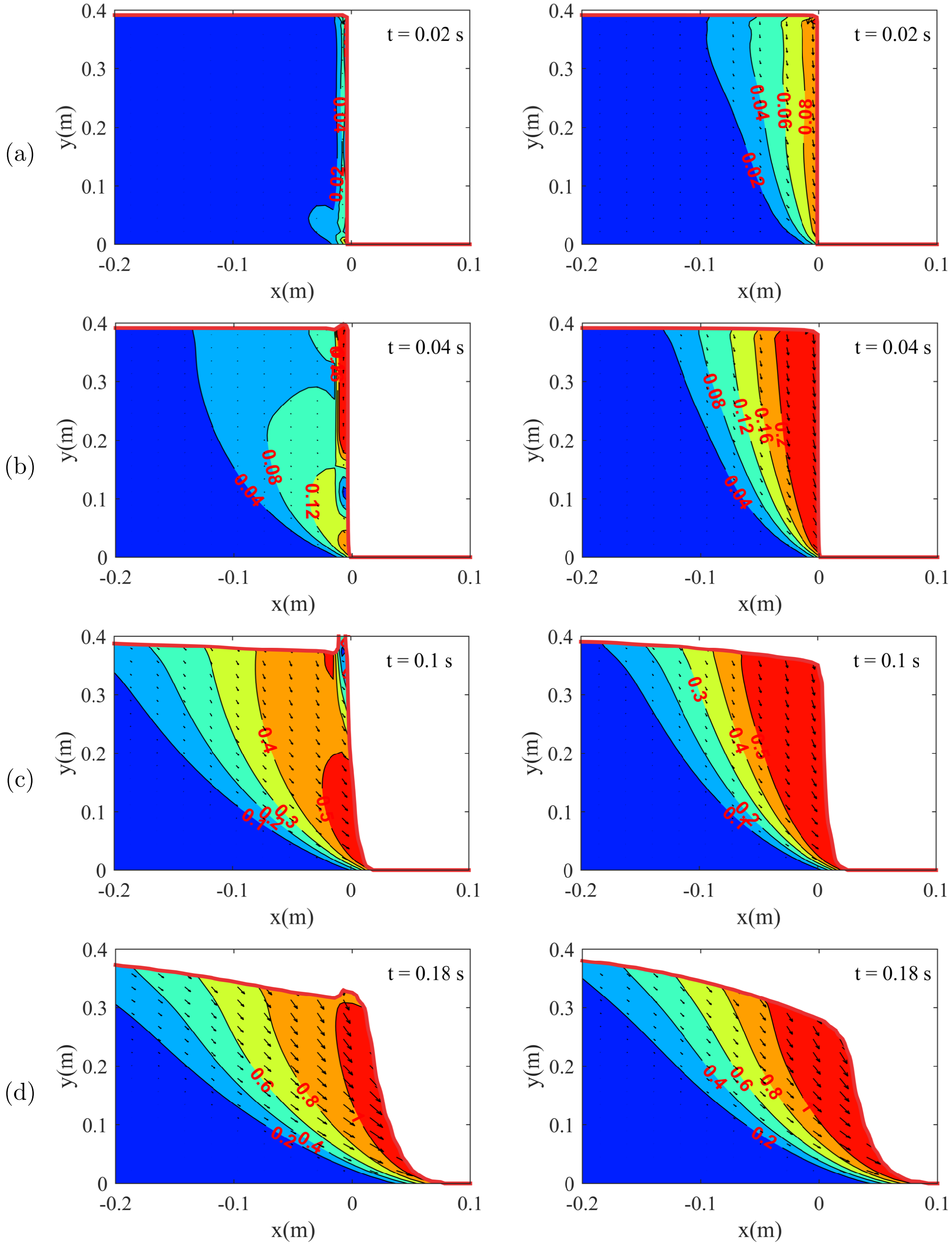

Figure 4.9: Velocity magnitudes and velocity vectors for the simulations with (left) and without (right) the gate at time t = 0.02, 0.04, 0.1 and 0.18s.

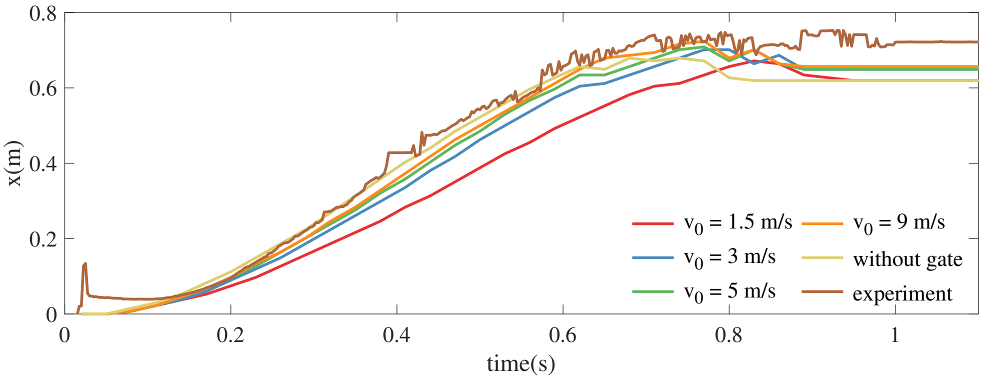

Figure 4.10: Propagation of the front toe for the simulations with different gate speeds, without the gate and experiments conducted by Rébillout et al. [74].

4.9 Comparisons between numerical simulations and experiments conducted by Evangelista et al. [17]

In this section, the simulation results are presented in comparison with the experiments of Evangelista et al. [17]. The details of the experimental setup are presented in Section 4.5. In the simulations, the time step is set to be 0.0005 s, while the cell size is 5 mm. The simulations were setup without the gate (sudden release). The constant friction model with $\mu = 0.65$ (tan32°) was used for all cases. Figure 4.11 shows the granular profiles at the final deposit. The simulation results show a good agreement with the experiments.

4.10 Comparisons between numerical simulations and experiments conducted by Mangeney et al. [58]

In this section, the simulation results are presented in comparison with the experiments of Mangeney et al. [58]. The details of the experimental setup are presented in Section 4.5 and sketch of the experimental setup is shown in Figure 4.12. In the simulations, the time step is set to be 0.0005 s, while the cell size is 0.25 cm. The gate is removed at a speed of $v_0 = 2.3\,m/s$ in the direction perpendicular to the bed. The sensitivity to the parameters of the $\mu(I)$ model is investigated. The different rheological formulas: the constant friction and $\mu(I)$ models is investigated. The simulation results obtained from the two rheological

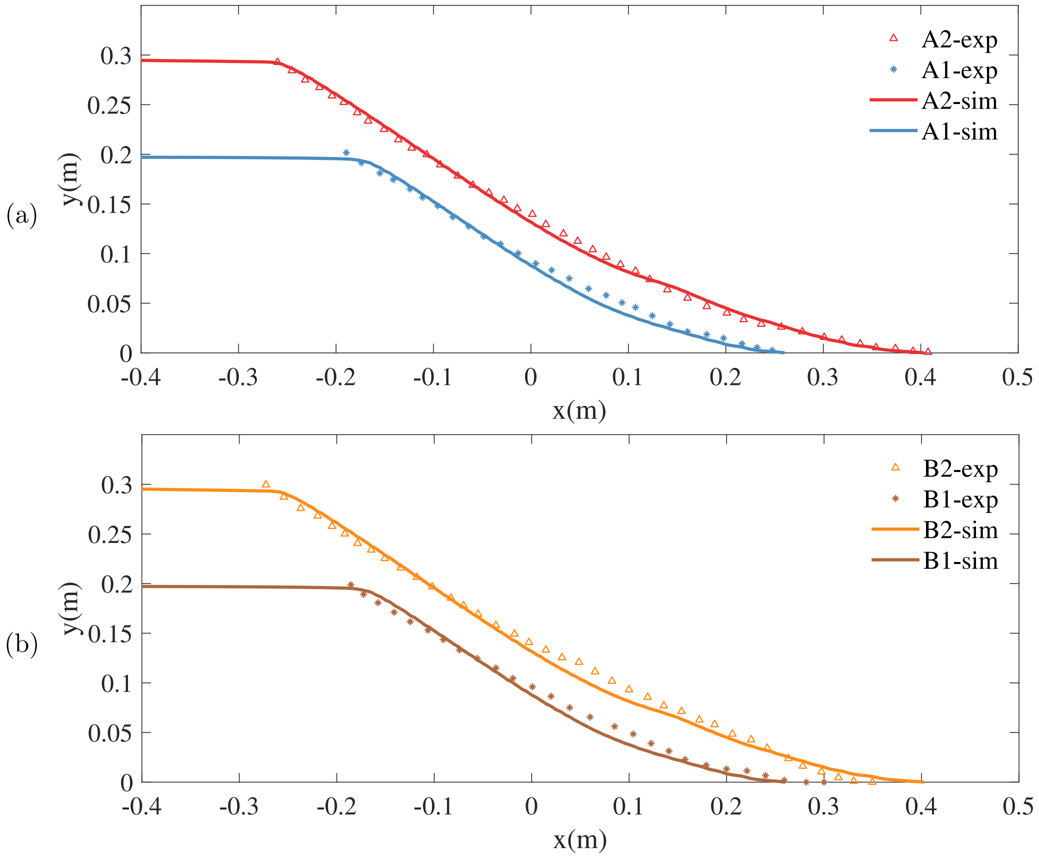

Figure 4.11: Comparison of the granular mass profiles between the experiments conducted by Evangelista et al. [17] and simulations at the final deposit for sand A and sand B.

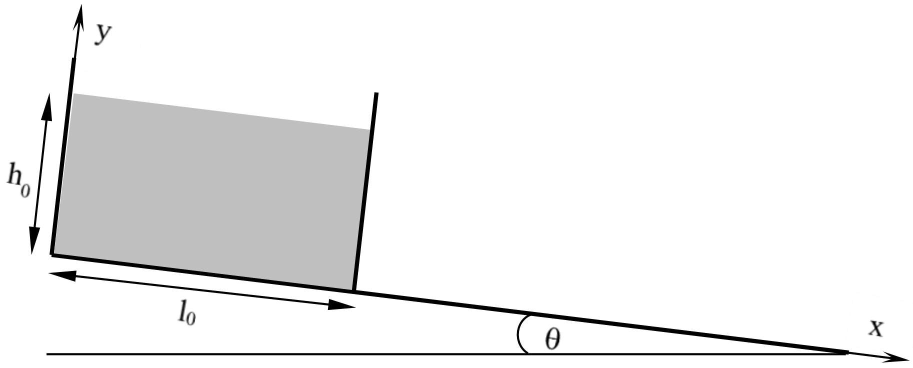

Figure 4.12: Sketch of experimental setup by Mangeney et al. [58].

models are compared with experimental results for different slopes of the channel bed.

4.10.1 Sensitivity to the parameters of the $\mu(I)$ rheology

The rheological parameters for the $\mu(I)$ model, which must be derived from the experiments, are μ_s, μ_2, and I_0. In this study, the rheological parameters of $(\mu_s, \mu_2, I_0) = (0.48, 0.73, 0.279)$ in Table 1 of Ionescu et al. [36] are adopted. The sensitivity test is performed with μ_s varying in the range [0.38,0.48], μ_2 varying in the range [0.68,0.78], and I_0 varying in the range [0.279,0.4]. While one parameter is varying, the other two are kept constant. Figure 4.13(a) shows the final deposit of the granular mass for different values of μ_s. It can be seen that a decrease of μ_s increases the displacement and decreases the column height. Figure 4.13(b) and (c) shows that a decrease in μ_2 results in the same effect, while a decrease in I_0 has the reverse effect. This behavior is as well observed in Lagrée et al. [48] and expected from the $\mu(I)$ dependence: a decrease in one parameter $(\mu_s, \mu_2, 1/I_0)$ increases the total friction (Lagrée et al. [48]).

4.10.2 Comparison between the constant friction and $\mu(I)$ models

The $\mu(I)$-rheology relates the frictional properties of the flow to the inertial number I which varies during the flow [48]; as seen in section 4.10.1, this model captures well the behavior of the dry granular dam-break flow. However, the performance of the $\mu(I)$ model

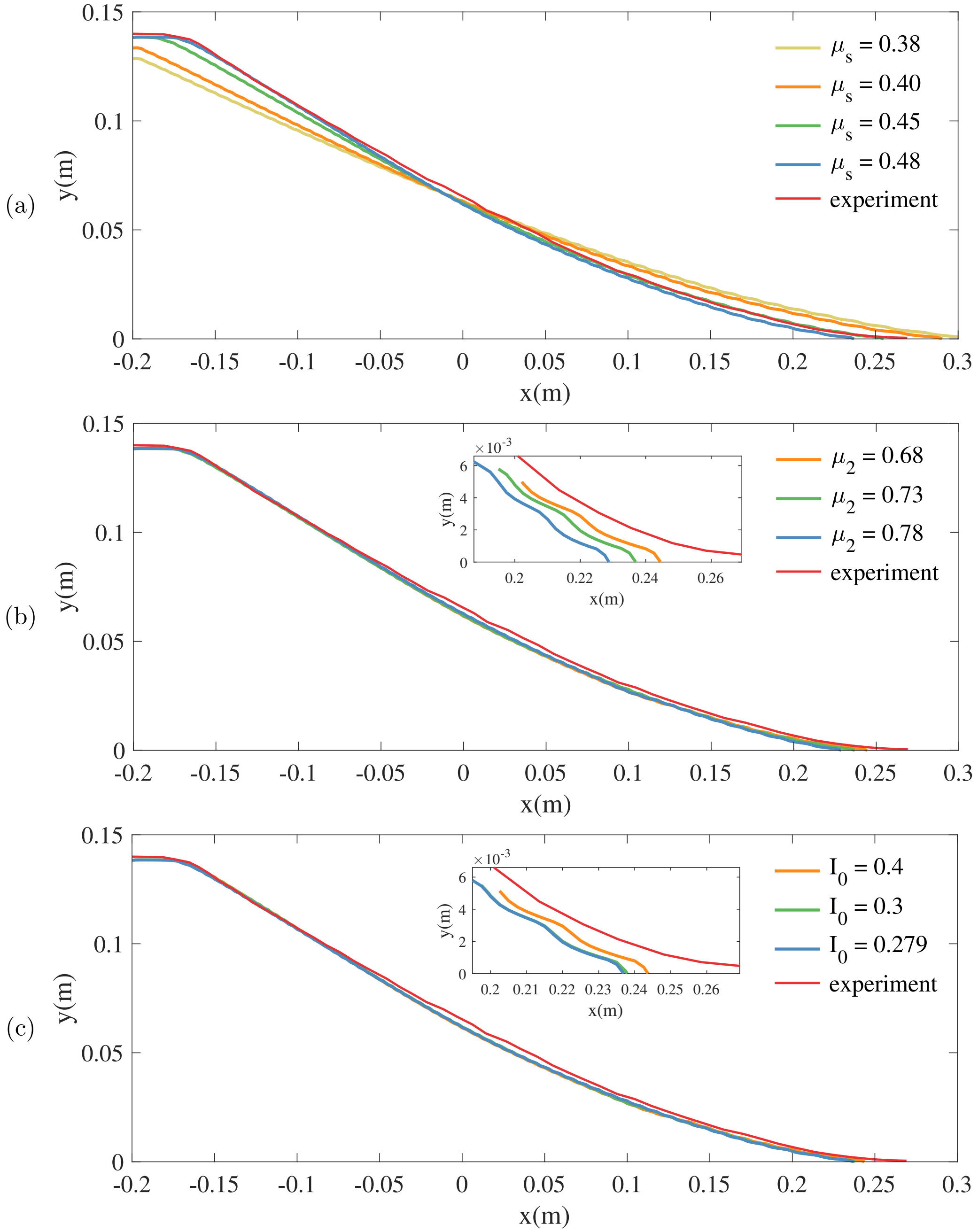

Figure 4.13: Granular mass profile at the final deposit for simulations and experiments of Mangeney et al. [58] ($\theta = 0°$) with different values of parameters in the $\mu(I)$ model.

compared to the simple constant friction model $\mu = \text{cst}$ is questionable. In this study, the simulations of dry granular dam-break flows using the two different models are performed. The parameters of the $\mu(I)$ model is adopted from Ionescu et al. [36], where $\mu_s = 0.48$, $\mu_2 = 0.73$, and $I_0 = 0.279$. For the constant friction model, μ is chosen to be $\mu = \mu_s = 0.48$. Figure 4.14 shows comparisons of the granular mass profiles obtained from experiments and simulations with the two different models at different times. In the early state of the flow ($t = 0.06\,s$), the profiles of the constant friction and $\mu(I)$ models show a good agreement. When the flow develops, the front tip of the constant friction model travels slightly faster than the $\mu(I)$ model. Using the constant friction model with $\mu = \mu_s = 0.48$ is equivalent to using the $\mu(I)$ model with $(\mu_s, \mu_2, I_0) = (0.48, 0.48, 0.279)$. As observed in section 4.10.1, a decrease of μ_2 increases the displacement and decreases the column height at the final deposit. However, as seen in Figure 4.14(a)-(c), in this case only small difference is found in the granular mass profiles obtained from the constant friction (using one parameter) and $\mu(I)$ (using three parameters) models.

4.10.3 Collapses over an inclined plane

Up to this section, simulations of dry granular flows have been performed only on a horizontal plane. Here, the collapses over inclined planes (see Figure 4.12) where $\theta = 10°$, $\theta = 16°$, and $\theta = 22°$ are simulated using the same sets of parameters. That is, $\mu_s = 0.48$, $\mu_2 = 0.73$, and $I_0 = 0.279$ for the $\mu(I)$ model and $\mu = \mu_s = 0.48$ for the constant friction model. Figure 4.15 shows the results. The $\mu(I)$ model captures the slope of the granular mass at the deposit. However, the front deposit are far less than the experiments for all three cases. This may be due to the no-slip boundary condition imposed at the bottom. As can be seen in Figure 16 of Ionescu et al. [36], the scenario with no-slip condition (with adherence) reduces the run-out distance by 10% compared with the scenario with the basal friction coefficient imposed at the bottom boundary condition. However, near the back wall, the scenario with no-slip condition reproduces the collapsed mass better. This is also observed

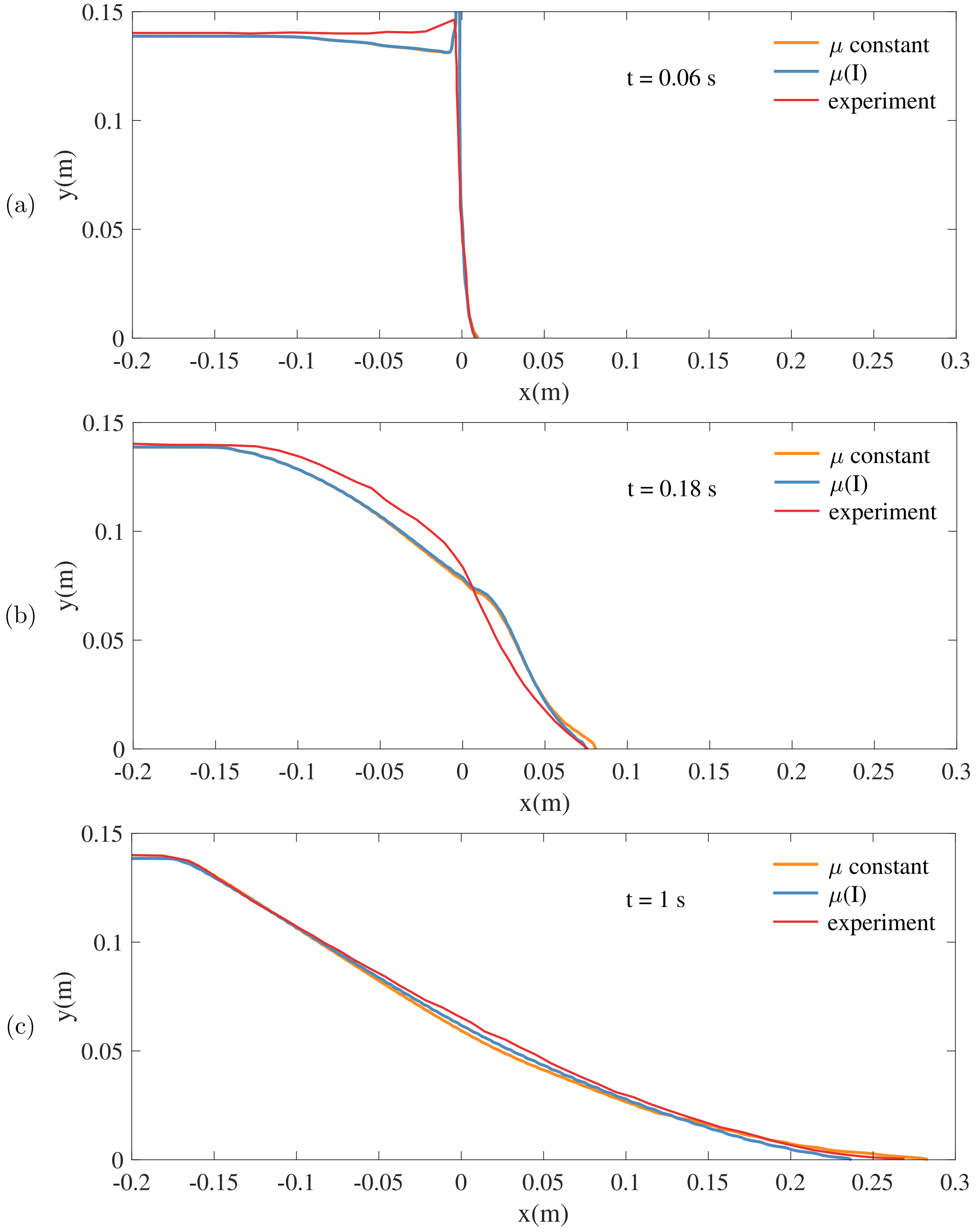

Figure 4.14: Granular mass profile at different times: (a) t = 0.06 s, (b) t = 0.18 s, and (c) t = 1 s for experiments of Mangeney et al. [58] and simulations over a horizontal plane ($\theta = 0°$) with the constant friction and $\mu(I)$ models.

in this study. The constant friction model is equivalent to the $\mu(I)$ model with parameters $(\mu_s, \mu_2, I_0) = (0.48, 0.48, 0.279)$. As expected, the column height at the deposit decreases and the displacement increases. For the case with $\theta = 10^\circ$, the difference between the simulation and experiment is small. The difference is more obvious in the case of $\theta = 16^\circ$ and $\theta = 22^\circ$ where the fronts hit the wall. In spite of the results, the constant friction model could still be used to obtain a good result but with the friction coefficient larger than 0.48.

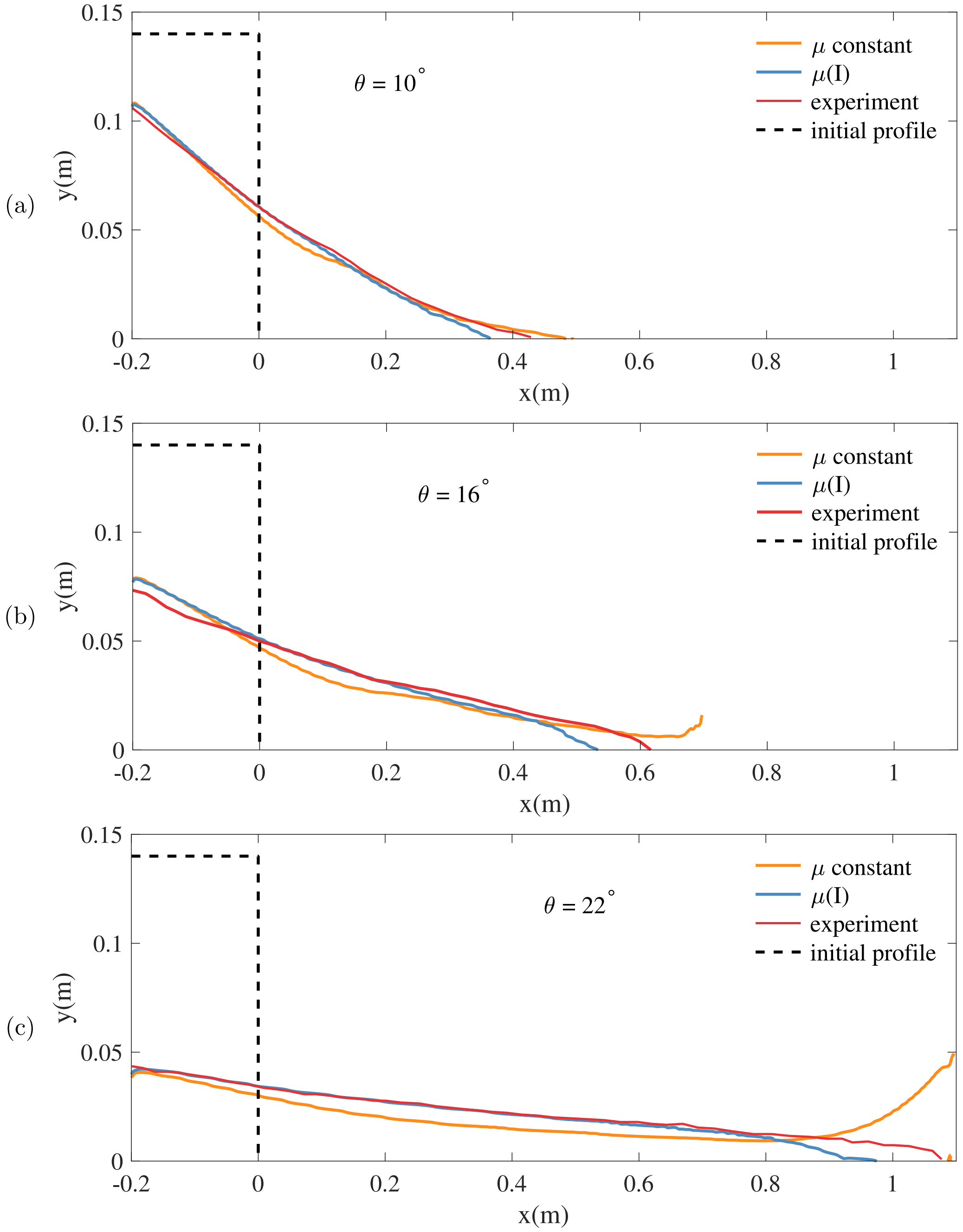

Figure 4.15: Granular mass profile at the final deposit for simulations and experiments of Mangeney et al. [58] with different slopes of channel bed: (a) $\theta = 0°$, (b) $\theta = 16°$, and (c) $\theta = 22°$.

CHAPTER 5

POROUS MEDIA FLOWS

This chapter presents the numerical models for flows in porous media using two different OpenFOAM solvers: *porousInterFoam* and *suGWFoam*. In *porousInterFoam* solver, the governing equation is the Navier-Stokes equation with additional terms to account for pressure drop due to consideration of a porous medium. This equation is based on the macroscopic equation derived by Wang et al. [85]. By using *porousInterFoam*, the flows inside and outside the porous medium are solved with the same set of equations. In *suGWFoam* solver, the nonlinear Richards' equation is solved in conjunction with the modified Picard iterative method. By using *suGWFoam*, variably saturated conditions in porous media can be investigated. Numerical simulations for verification and validation of the approaches used the steady and transient drainage experiments carried out in a 2D channel containing the clear water zone and the porous zone filled with granulated urea material saturated with water. Simulated water surface elevations are presented on the snapshots of the experiments.

5.1 Governing equations: Navier-Stokes equations

In this study, the macroscopic governing equations for the fluid flow in porous media derived by Wang et al. [85] are employed. The macroscopic equations is obtained by the technique of volume averaging of the microscopic continuity and momentum equations over a representative elementary volume (REV). The intrinsic phase average is used in the derivation and defined by

$$\langle \psi_f \rangle^f = \frac{1}{V_f} \int\limits_{V_f} \psi_f dV \tag{5.1}$$

where the subscript f means fluid quantity which refers to the portion of fluid existing within the gaps of the solid skeleton, V_f represents the volume of the fluid phase within the representative elementary volume V, and ψ_f is a quantity associated with the fluid phase. The intrinsic phase average can be related to the phase average (also called Darcy's quantities) with: $\langle \psi_f \rangle = n \langle \psi_f \rangle^f$, where n is the porosity, and is defined as $n = V_f/V$. As concluded by Wang et al. [85], the macroscopic conservation equations derived using intrinsic phase average velocity are Galilean invariant. The following macroscopic equations can be obtained

$$\bigtriangledown \cdot \langle u_f \rangle^f = 0 \tag{5.2a}$$

$$\frac{\partial \left(\rho_f \langle u_f \rangle^f\right)}{\partial t} + \bigtriangledown \cdot \left(\rho_f \langle u_f \rangle^f \langle u_f \rangle^f\right) = -\bigtriangledown \langle p_f \rangle^f + \mu \bigtriangledown \cdot \left[\bigtriangledown \left(\langle u_f \rangle^f\right) + \left[\bigtriangledown \left(\langle u_f \rangle^f\right)\right]^T\right] + \boldsymbol{F} \tag{5.2b}$$

where ρ_f is the fluid density, $\langle u_f \rangle^f$ is the intrinsic phase average velocity, p_f is the pressure, μ is the fluid dynamic viscosity and $\boldsymbol{F}$ is the total body force including the resistance from the porous medium and other external forces and defined by

$$\boldsymbol{F} = -\frac{\mu n}{K} \left(\langle u_f \rangle^f - \boldsymbol{V_p}\right) - \rho_f \frac{n^2 F_n}{\sqrt{K}} \left(\langle u_f \rangle^f - \boldsymbol{V_p}\right) \left|\langle u_f \rangle^f - \boldsymbol{V_p}\right| + \rho_f \boldsymbol{g}. \tag{5.3}$$

where K is the permeability, $\boldsymbol{g}$ is the gravitational acceleration, $F_n = 1.75/\sqrt{150 n^3}$ is the geometric function of the porous medium, and $\boldsymbol{V_p}$ is the velocity of the moving porous medium. In this Chapter, only static porous medium is considered and a moving porous medium is included later in Chapter 6. Hence, here $\boldsymbol{V_p}$ is set to zero. In the case as $n = 1$, i.e., in the absence of porous media, the value of K will become infinite, and Equation 5.2 reduces to the Navier-Stokes equations for pure fluid flows. By using Equation 5.2, the flows inside and outside the porous medium are solved with the same set of equations. This approach avoids the need to specify matching conditions at the pure fluid and porous medium interface, at which interface and jump conditions are defined for velocity and shear stresses [44]. Further details of the derivation can be found in Wang et al. [85].

The above equations are solved in OpenFOAM using the solver *porousInterFoam*. The governing equations for *porousInterFoam* solver are as follows:

$$\bigtriangledown \cdot \mathbf{u} = 0 \tag{5.4a}$$

$$\frac{\partial \rho \mathbf{u}}{\partial t} + \bigtriangledown \cdot (\rho \mathbf{u}\mathbf{u}) = -\bigtriangledown p + \rho \mathbf{g} + \mu \bigtriangledown \cdot \left(\bigtriangledown \boldsymbol{u} + (\bigtriangledown \boldsymbol{u})^T \right) + \boldsymbol{S} \tag{5.4b}$$

where $\boldsymbol{u} = \langle u_f \rangle^f$, $\rho = \rho_f$ and $p = p_f$ in the equations 5.2 and 5.3. The sink term, $\boldsymbol{S}$, is composed of two parts, a viscous loss term and an inertial loss term, creating a pressure drop that is proportional to the velocity and velocity squared, respectively. This term is defined by

$$\boldsymbol{S} = -\left(\mu \boldsymbol{D} + \frac{1}{2} \rho |\boldsymbol{u}| \boldsymbol{F} \right) \boldsymbol{u} \tag{5.5}$$

where the tensors $\boldsymbol{D}$ and $\boldsymbol{F}$ are the porosity parameters. In the case of simple homogeneous porous media, they can be represented by scalar d and f. In OpenFOAM, homogeneous directions are generally considered thanks to vector $\boldsymbol{d}$ and $\boldsymbol{f}$ that are defined in a local set of coordinates. If a homogeneous porous media is considered, it is possible to link directly the Darcy-Forcheimer equation (Eq. 2.18) to the solver parameter and by comparing with equation 5.3, the porosity parameters can be defined by

$$d = \frac{n}{K} \text{ and } f = \frac{2n^2 F_n}{\sqrt{K}}. \tag{5.6}$$

In this study, the permeability K is obtained from the laboratory test (Ozeren et al. [67]). The *porousInterFoam* solves Equation 5.4 using the VOF method as described in Section 4.2.

It is noted that the *porousInterFoam* solver already exists in OpenFOAM. However, the way it is implemented is only suitable for a static porous medium. In the existing *porousInterFoam*, a porous zone is created as a cell zone using *blockMesh* or *topoSet* utilities when creating mesh or before the simulation starts. During the simulation, the *porousZone* class is called to explicitly or implicitly calculate pressure drops in the created porous (or cell) zone. If this cell zone moves or changes the shape during the simulation, an extra step and computation time are required to select those porous cells and recreate them. Instead of using the existing *porousInterFoam*, the *interFoam* solver is modified by adding the source term S defined in equation 5.5 to the momentum equation. This term is multiplied by a mask function which allows to define both the porous area where the source term is active, and the free area where the classical momentum is solved. Deforming porous medium can be treated through the mask function. This modified *interFoam* solver is also called *porousInterFoam* since the concept of modeling porous media flow is the same, and only the implementation is different.

5.2 Governing equations: Richards equations

5.2.1 Richards equations

Flows in variably saturated porous media can be modeled by solving the mass conservation equation with the velocity expressed using Darcy's law. A commonly used model in soil science is the so-called Richards' equation [75]. This equation can be written in three standard forms: the pressure head-based form, the saturation based form, and the mixed form formulation.

- **Presure head-based form**:

$$[C(h) + S_s S_w]\frac{\partial h}{\partial t} = \bigtriangledown \cdot [K(h) \cdot \bigtriangledown (h + z)] + Q_s \tag{5.7}$$

- **Saturation-based form**:

$$\frac{\partial \theta}{\partial t} + S_s S_w \frac{\partial h}{\partial t} = \bigtriangledown \cdot [D(\theta) \cdot \bigtriangledown \theta] \bigtriangledown \cdot [K(h) \cdot \bigtriangledown z] + Q_s \tag{5.8}$$

- **Mixed form**:
$$\frac{\partial \theta}{\partial t} + S_s S_w \frac{\partial h}{\partial t} = \bigtriangledown \cdot [K(h) \cdot \bigtriangledown (h+z)] + Q_s \tag{5.9}$$

where $C(h)$ is the specific moisture capacity (L^{-1}) which is defined as

$$C(h) = \frac{\partial \theta}{\partial h}, \tag{5.10}$$

θ is the moisture content, h is the pressure head (L), Q_s is the volumetric source/sink $(L^{-3}T^{-1}L^{-3})$, S_s is the specific storage (L^{-1}), S_w is the saturation ratio (θ/n), n is the porosity, $K(h)$ is the hydraulic conductivity (L/T), and $D(\theta)$ is the hydraulic diffusivity (L^2T^{-1}).

As discussed in Liu [50], the pressure head-based form can be used for both saturated and unsaturated condition and gives good mass balance when the variation of h is small. However, this form suffers from severe mass balance error when water infiltrates into dry soils with highly nonlinear conditions unless very fine spatial and temporal discretizations are used in the numerical scheme (Celia et al. [9]). The saturation-based form demonstrates significantly improvement when modeling infiltration into very dry soils (Hills et al. [30]). Unfortunately, this form is not suitable for fully saturated conditions because hydraulic diffusivity $D(\theta)$ is infinity in saturated regions and a head-saturation relationship does not exist. In addition, it requires special treatments for soil discontinuities or layered soils (Hao et al. [28]). The mixed-form possess much better properties regarding mass conservation in simulating soil water problems with a sharp wetting front. However, large mass balance errors are encountered in simulations in which there is large amount of water moving through the bottom boundary (Hao et al. [28]). Each form of the Richards' equation has its strengths and drawbacks. Therefore, it is reasonable to combine them and switch between the forms according to the state of the modeled system.

The switching algorithm is proposed by Hao et al. [28], where the pressure head-based form and the mixed form are selected dynamically during the simulation. Within a time step, the magnitude of the pressure head change is calculated as $h_c = |h^{n+1} - h^n|$ and compared with a specified threshold value h_0, where the superscripts $n+1$ and n represent the values at current time step and previous time step, respectively. If $h_c < h_0$, the pressure head-based form is solved, otherwise the mixed form is solved. The threshold value depends on many factors and it affects the accuracy and convergence of the simulation (Hao et al. [28]). In this study, the value of $h_0 = 0.03\,m$ as suggested by Hao et al. [28] and used by Liu [50] is adopted.

5.2.2 Constitutive relations

The constitutive relations refer to the functional forms of the moisture content $\theta(h)$ and hydraulic conductivity $K(h)$. Using this formulation, the routines in the model should calculate the moisture content and hydraulic conductivity given the values of pressure head h. There have been numerous approaches proposed for constitutive relations. This section describes two commonly adopted models: the Brooks and Corey (1964) model and the van Genuchten (1980) model. In this study, the van Genuchten (1980) model is employed and has the following formulas for moisture content θ and the relative hydraulic k_r conductivity

$$\theta(h) = \begin{cases} \theta_r + \frac{\theta_s - \theta_r}{[1+(\alpha|h|)^n]^m} & \text{if} \quad h < 0 \\ \theta_s & \text{otherwise} \end{cases} \tag{5.11}$$

$$k_r(\theta) = \frac{K}{K_s} = \left(\frac{\theta - \theta_r}{\theta_s - \theta_r}\right)^{0.5} \left\{1 - \left[1 - \left(\frac{\theta - \theta_r}{\theta_s - \theta_r}\right)^{1/m}\right]^m\right\}^2 \tag{5.12}$$

where α and n are the parameters controlling the shape of the soil constitutive curves, and $m = 1 - 1/n$.

5.2.3 Boundary conditions

The specification of boundary conditions is required in order to obtain unique solutions to the Richards' equations. In *suGWFoam*, four types of basic boundary conditions are implemented which include fixed head h, fixed total head $h + z$, specific flux q, and fixed value at specified internal locations. Details and implementations of these boundary conditions can be found in Liu [50]. However, a seepage face boundary condition required in this study is not available in *suGWFoam*.

A seepage face is the boundary between a saturated flow field and the atmosphere, or between a saturated flow field and a stream channel, where water is free to exit from the subsurface (Scudeler et al. [81]). The seepage face can be treated as static or dynamic boundary conditions. In a static type, the seepage boundary that regulates subsurface drainage is often treated as a fixed Dirichlet condition, with atmospheric pressure assigned to the designated outflow cells. Alternatively, with a dynamic type, the position of the exit point along the seepage boundary can evolve over time depending on the location of phreatic surface. All cells below the exit point are at atmospheric pressure (a Dirichlet condition), allowing outflow to occur, while all cells above it are assigned a no-flow (Neumann) condition. The conceptual representation of the seepage face boundary conditions is presented in Figure 5.1.

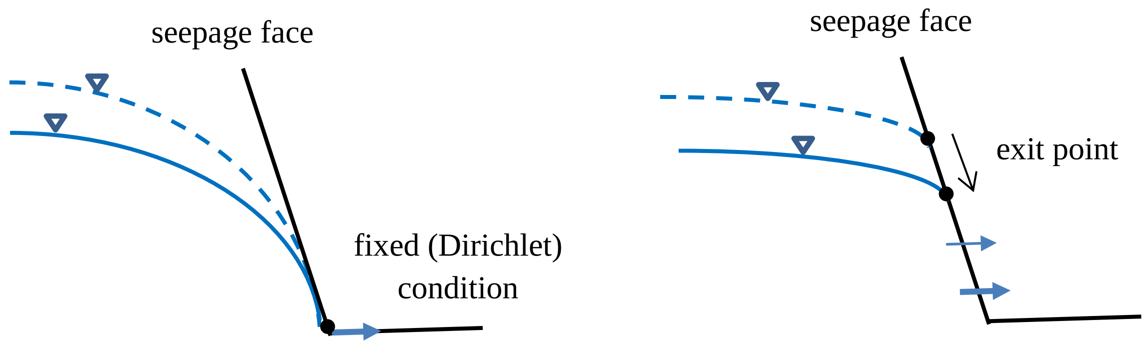

(a) static

(b) dynamic

Figure 5.1: Conceptual representation of the seepage face boundary conditions.

The dynamic boundary condition is employed in this study. At each iteration, the seepage face boundary is checked cell by cell to identify if the cell belongs to an outflow plane (below the exit point) or a no-flow plane (above the exit point). If a cell has zero or positive pressure, that cell belongs to an outflow plane. Otherwise, a no-flow condition is assigned. This process of checking and setting boundary cells is completed by using *groovyBC* library in OpenFOAM.

5.3 Experimental setup for transient drainage from porous media

The experiments conducted in the dam-break facility of NCCHE at the USDA-ARS National Sedimentation Laboratory in Oxford, Mississippi are used to validate the models. In these experiments, the channel consisting of a 0.5 m width, 0.6 m height and 3.24 m length was divided into: (i) the clear water zone, and (ii) the porous zone containing urea material saturated with water. The urea material used in the experiments and the experimental setup are shown in Figure 5.2 and Figure 5.3, respectively. Some of the intrinsic and bulk properties of the material are summarized in Table 5.1. In the table, D_m is the mean nominal, S_f is the shape factor, diameter, n is the porosity, ρ_{Urea} is the density of the Urea material, and K the (packed) hydraulic conductivity. At the beginning of the experiments, the gate attached to the end of the porous zone was removed. Water in the clear water zone seeped in to the porous zone while water in the porous zone seeped out of the medium through the seepage face at the gate side resulting in drops of the phreatic surface. Blue dye was added to the water in order to better identify the phreatic surface. The same experiment was repeated three times and are referred to as exp1, exp2, and exp3.

Figure 5.2: Urea material.

Table 5.1: Properties of the urea material (Ozeren et al. [67]).

d_{10} (mm)	d_{50} (mm)	d_{90} (mm)	D_m (mm)	S_f	n (packed)	ρ_{Urea} (kg/m^3)	K (mm/s)
1.762	2.237	2.639	2.055	0.447	0.422	1476	8.51

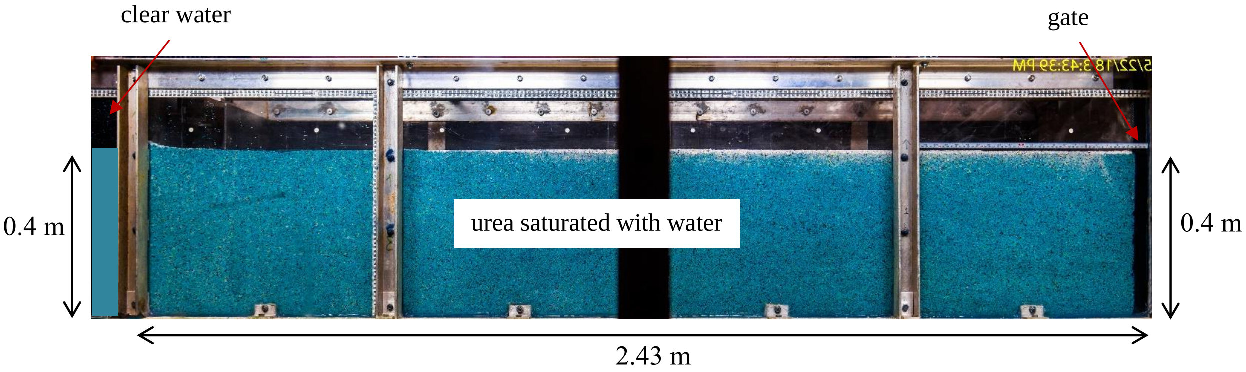

Figure 5.3: Experimental setup.

5.4 Simulation setup and results for transient drainage from porous media using Navier-Stokes equations

5.4.1 Simulation setup

In the numerical simulation, the computational domain (Figure 5.4) of a 4.67 m length and 0.5 m height is divided into three zones: (i) the porous zone containing the urea material saturated with water to a 0.4 m height, (ii) the clear water zone filled with water to the same height as the porous zone, and (iii) the empty cell zone. The slip wall boundary condition is used for the porous zone while the no-slip is employed at other boundaries except at the top and the right boundaries at which the outlet boundary condition is used. By modeling the flow in this way (see Section 5.1), there is no need to specify a boundary condition between the porous zone and the clear water zone, or the porous zone and the atmospheric (empty cell) zone. The time step is set to 0.01 s while the cell size is 0.01 m. The simulation results are compared with all three repeated experiments: exp1, exp2, and exp3. The comparisons are shown in the following section.

5.4.2 Simulation results

Figure 5.5 - 5.9 show the free surface elevations obtained from the simulation plotted over the snapshots of the three repeated experiments (exp1, exp2, and exp3) at time 0.4, 1,

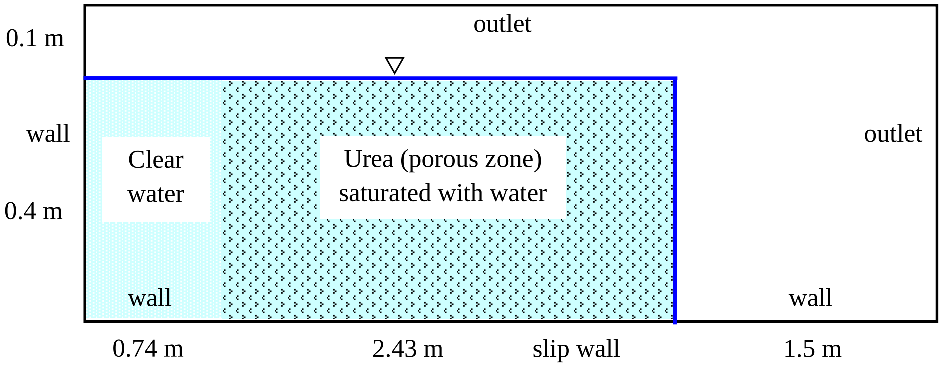

Figure 5.4: Computational domain for the Navier-Stokes equations with VOF method.

5, 10, 20, and 40 minutes. These elevations represented by the yellow lines correspond to the phreatic surfaces where pressure is zero. For the volume fraction (γ), as shown in Figure 4.4, only slight difference is observed in the free surface profile when using different values of volume fraction to plot the free surface. Here, the volume fraction $\gamma = 0.5$ is applied in the subsequent plots.

In the early stage of the flow at time $t = 1$ min (Figure 5.5), the phreatic surface at the front of the porous zone near the gate is about 0.05 m above the channel bed while the free surface elevation in the clear water zone has only slightly dropped. For all experiments, the blue dye interface is about 1 - 4 cm above the simulated phreatic surface. At later time (Figure 5.6 - 5.9), the phreatic surfaces along the channel drop below the initial value of 0.4 m. These phreatic surfaces (yellow lines) are also about 1 - 4 cm below the blue dye interfaces. The difference between the yellow lines and the blue dye interfaces could be explained by the capillary fringe zone. In this zone, the porous medium remains saturated under negative pore pressure, and the blue dye interfaces could be the upper end of this zone. The conceptual illustration of this zone is shown in Figure 5.10.

As pointed out earlier, by modeling porous flow using the *porousInterFoam* solver, it is not necessary to specify a boundary condition between the porous zone and the clear water zone. The process of water seeping from the clear water zone to the porous zone is taken care of by the solver. This can be verified by comparing the free surface elevations in the clear water zone obtained from the simulation and the experiment. The comparison plotted in Figure 5.11 shows that the two elevations drop at almost the same rate.

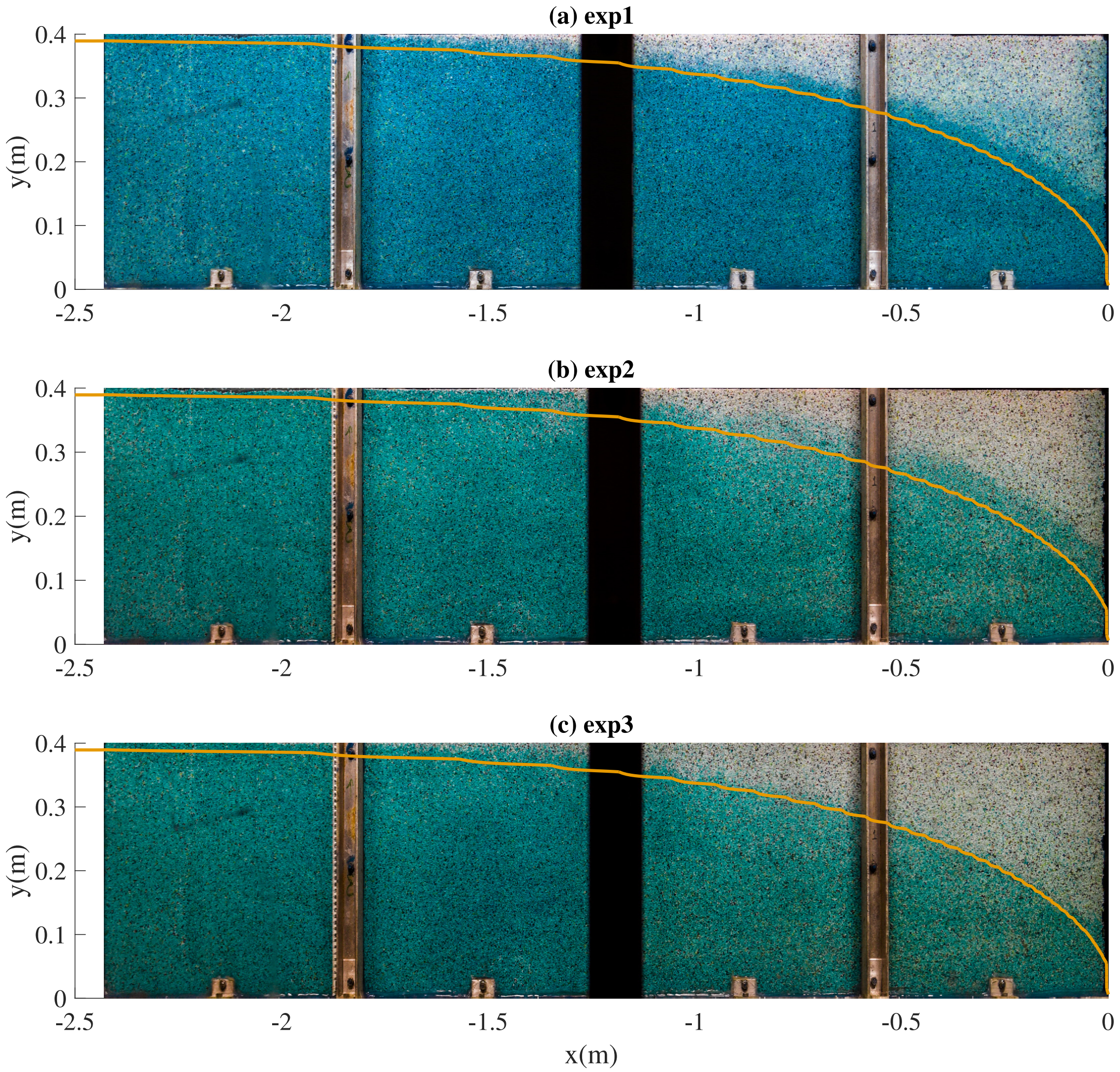

Figure 5.5: Plots of the simulated phreatic surface (yellow lines) obtained from *porousInterFoam* solver over snapshots of the experiments (exp1, exp2 and exp3) at time $t = 1$ min.

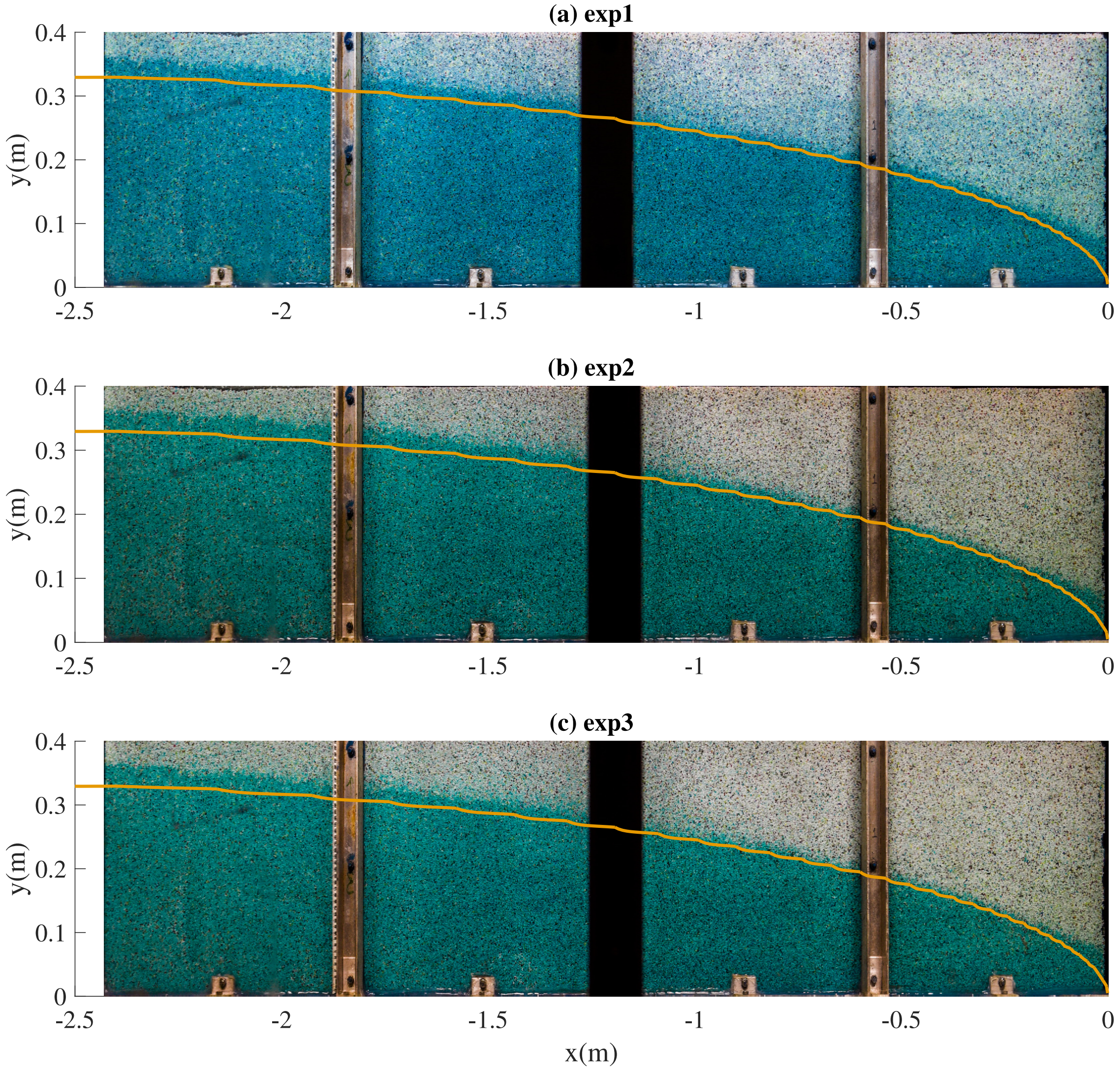

Figure 5.6: Plots of the simulated phreatic surface (yellow lines) obtained from *porousInterFoam* solver over snapshots of the experiments (exp1, exp2 and exp3) at time $t = 5$ min.

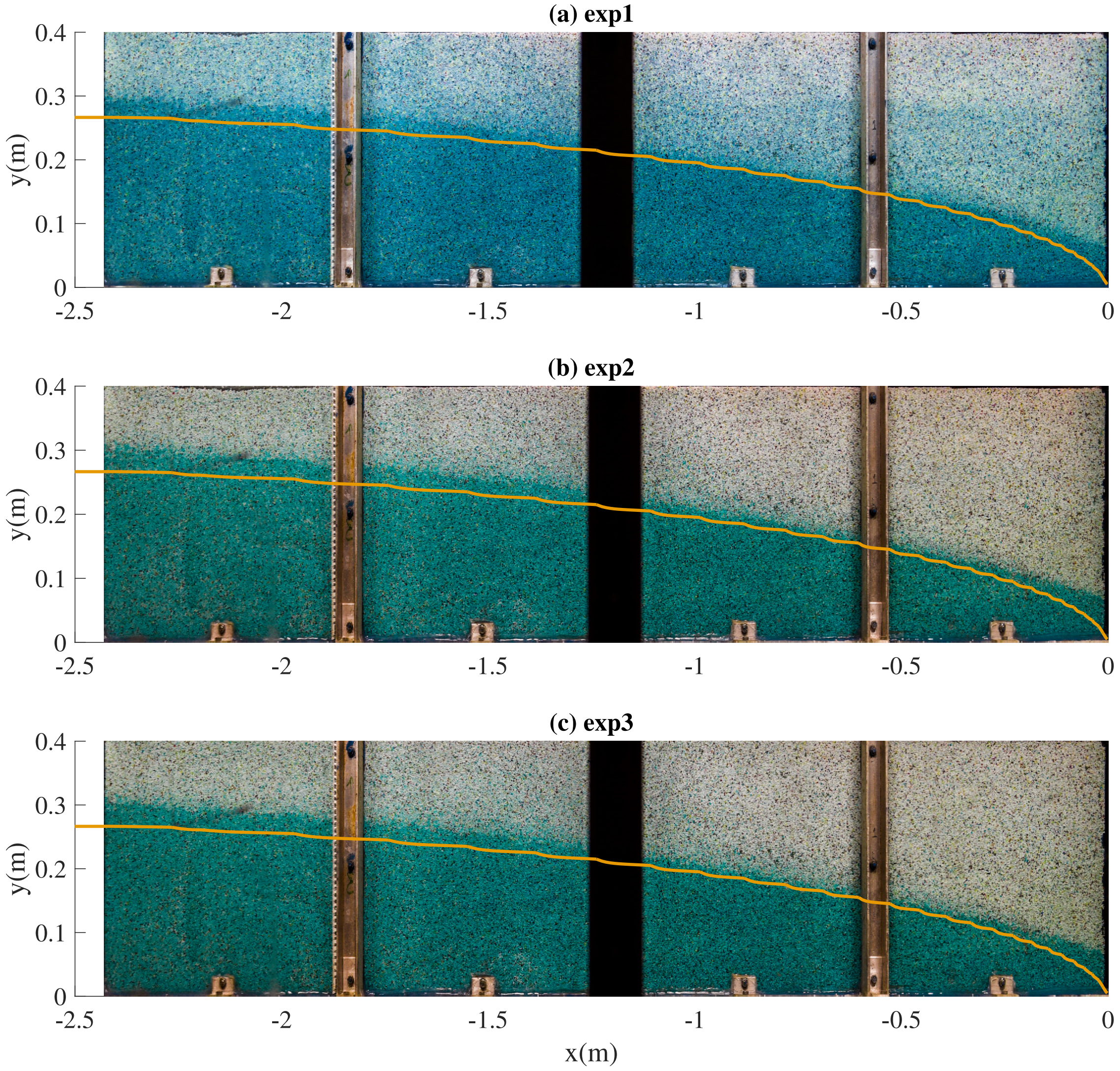

Figure 5.7: Plots of the simulated phreatic surface (yellow lines) obtained from *porousInterFoam* solver over snapshots of the experiments (exp1, exp2 and exp3) at time $t = 10$ min.

(a) exp1

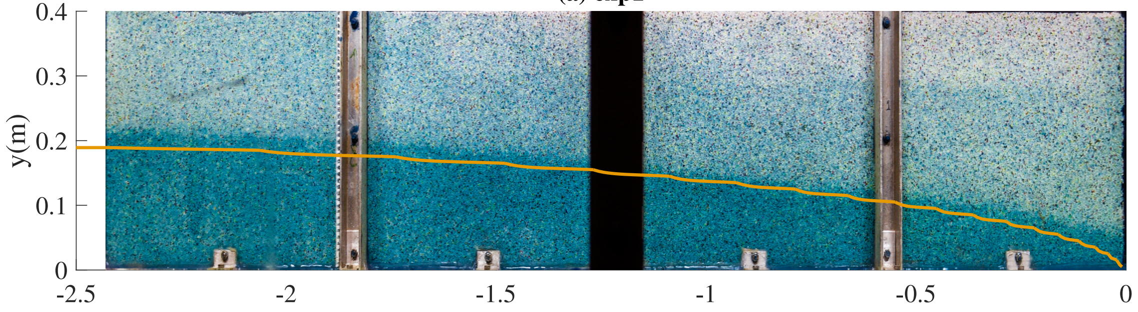

(b) exp2

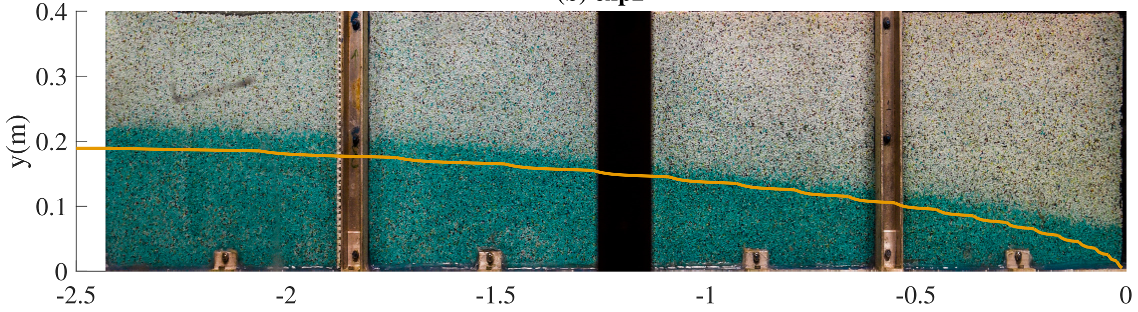

(c) exp3

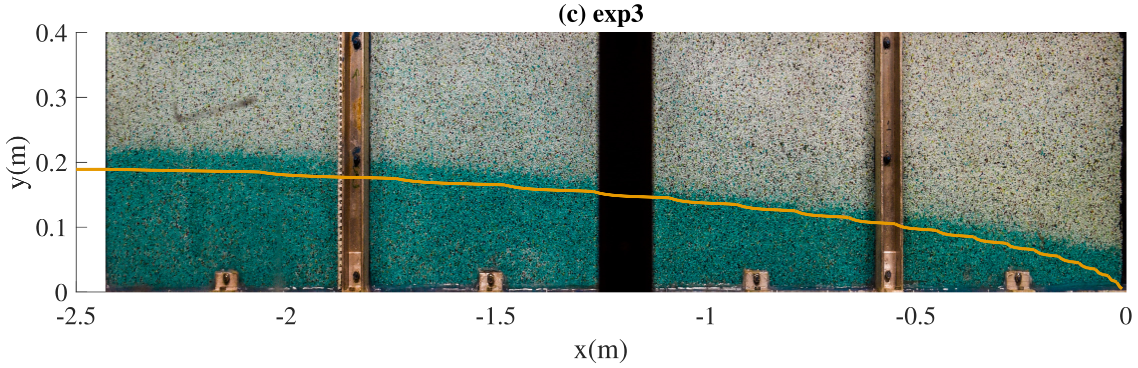

Figure 5.8: Plots of the simulated phreatic surface (yellow lines) obtained from *porousInterFoam* solver over snapshots of the experiments (exp1, exp2 and exp3) at time $t = 20$ min.

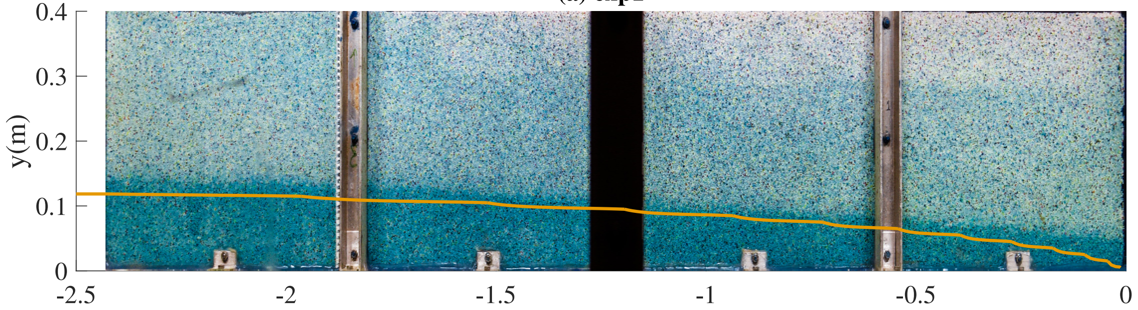

(a) exp1

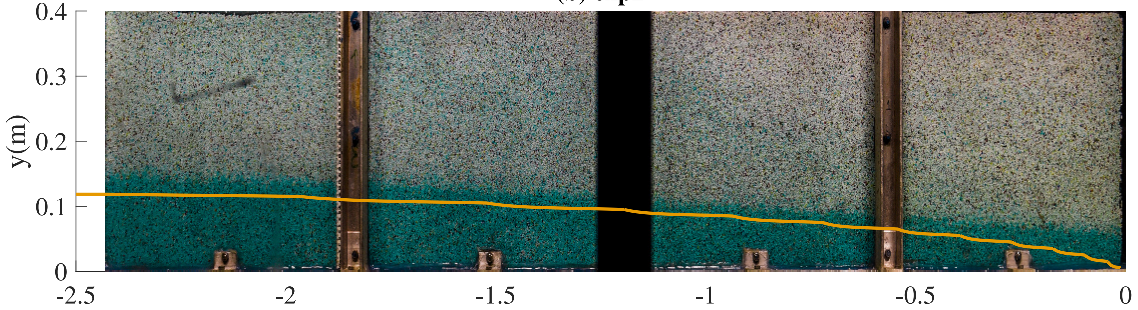

(b) exp2

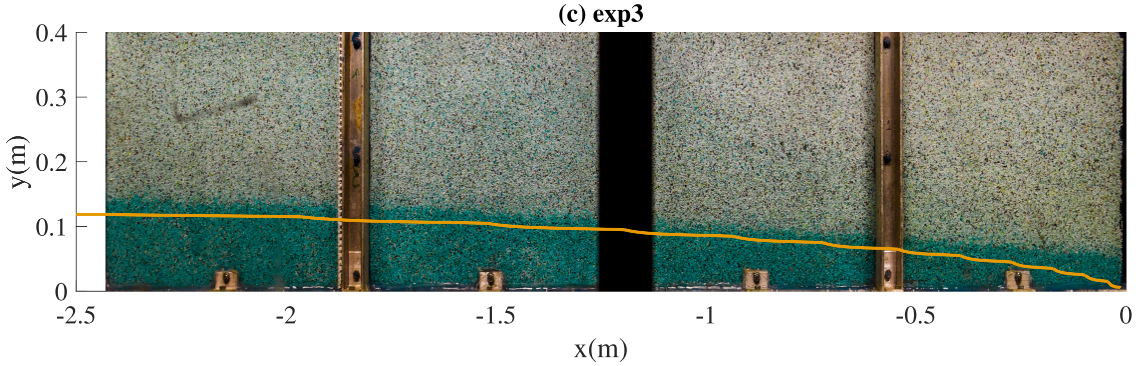

(c) exp3

Figure 5.9: Plots of the simulated phreatic surface (yellow lines) obtained from *porousInterFoam* solver over snapshots of the experiments (exp1, exp2 and exp3) at time $t = 40$ min.

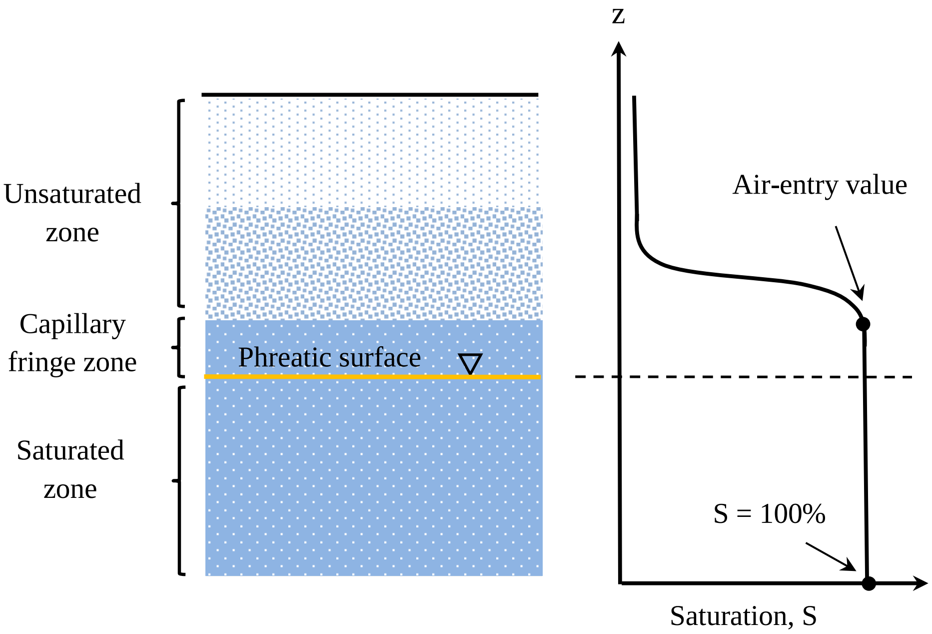

Figure 5.10: Conceptual illustration of the unsaturated porous medium (Lu and Likos [56]).

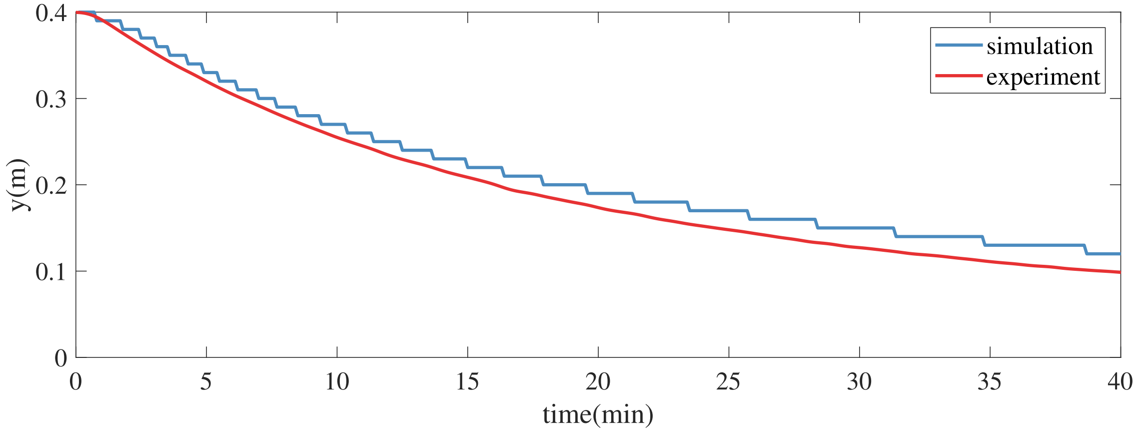

Figure 5.11: Time series of free surface elevations in the water reservoir obtained from the simulation and the experiment.

5.5 Simulation setup and results: Richards equations

5.5.1 Simulation setup

In the numerical simulation using *suGWFoam* solver, the computational domain (Figure 5.12) of a 2.43 m width and 0.4 m height contains the urea material saturated with water. It is noted that only the porous zone is included in the computational domain because the Richards' equation cannot handle the clear water zone. The boundary between the porous zone and the clear water zone is treated through a boundary condition. Properties of the urea material are described by the van Genuchten constitutive relationship. The van Genuchten parameters are listed in Table 5.2. The corresponding soil-water retention curve is plotted on Figure 5.13 based on the given pararameters. The no-flow ($q = 0$) boundary condition is used for the top and the bottom boundaries. The left side is the boundary between the porous zone and the clear water zone where the specified (transient) head boundary condition is used. This head obtained from the experiment is represented by the red line plot in Figure 5.11. The right boundary is where the gate is located in Figure 5.3. The dynamic seepage face boundary condition (see Subsection 5.2.3) is used. The time step is set to be 0.01 s. The cell size is 1 cm.

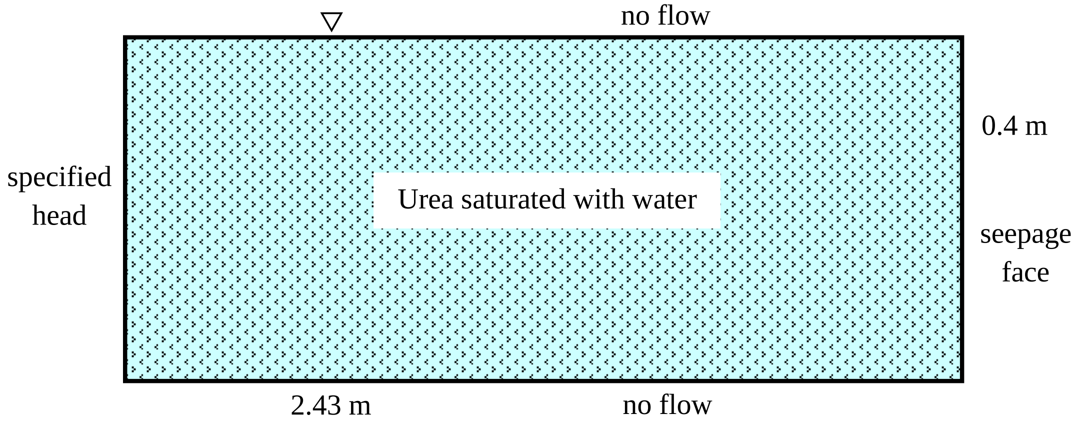

Figure 5.12: Simulation setup: Richards equations.

Table 5.2: Values of parameters for the porous media flow model.

Parameters	**Symbol**	**Urea**
Residual moisture content (-)	θ_r	0.01
Saturated moisture content (-)	θ_s	0.42
Van Genuchten model parameter (-)	n	10
Van Genuchten model parameter (m^{-1})	α	30
Specific storage (m^{-1})	S_s	0
Saturated hydraulic conductivity (m/s)	K_s	0.00851

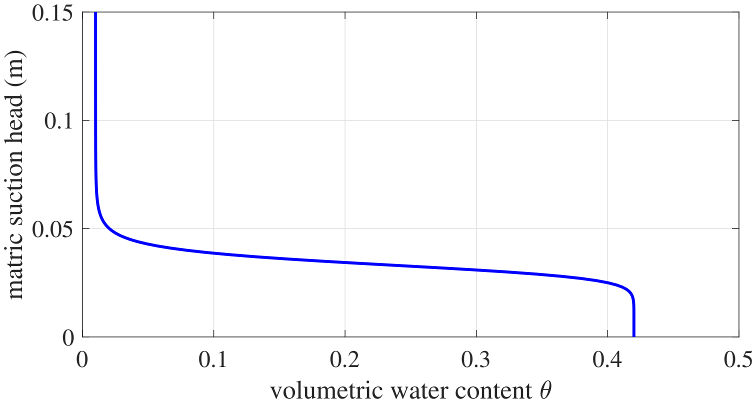

Figure 5.13: Water retention curve.

5.5.2 Simulation results

Figure 5.14 shows the simulated contours of pressure head over the snapshots of the experiment (exp2) at time t = 1, 10, 20 and 40 minutes. The contours labelled with zero represent the phreatic surfaces. These phreatic surfaces are found to be about 3 - 5 cm below the blue dye interface. As explained in Subsection 5.4.2, the zone above the zero pressure line and the blue dye interface could be the capillary fringe zone. In a numerical simulation, the height of this zone typically depends on the parameters of the van Genuchten model which has to be experimentally defined. At the blue dye interfaces, the capillary pressure (head) p_c described in Section 2.6 is about 0.04 m. This value is also dependent on the van Genutchen parameters. Figure 5.15 shows the simulated saturation ratio along cross-section x = -1 m (the red lines in Figure 5.14) at time t = 1, 10, 20 and 40 minutes.

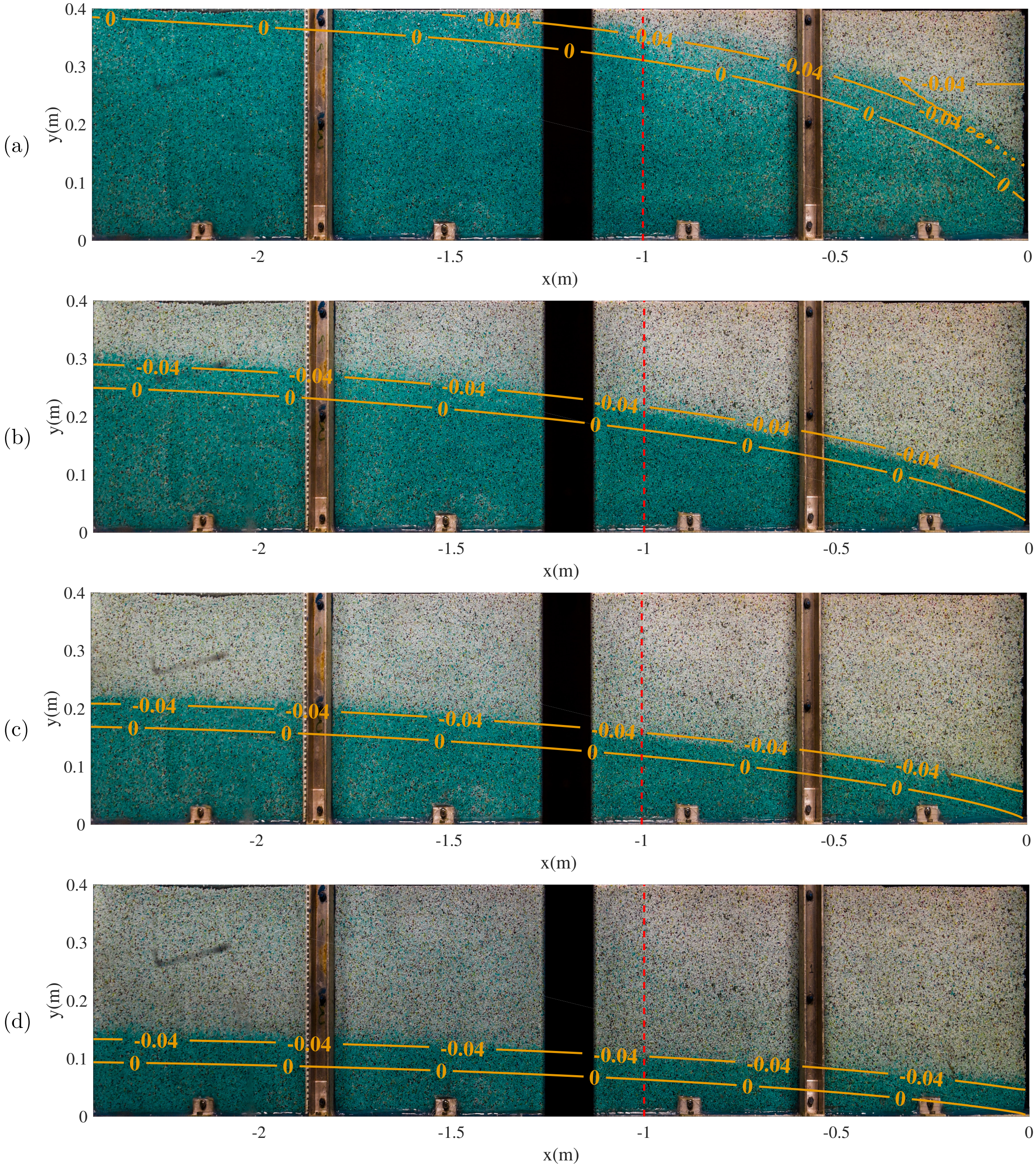

Figure 5.14: Plots of the simulated phreatic surfaces obtained from *suGWFoam* solver over snapshots of the experiment (exp2) at time (a) 1, (b) 10, (c) 20 and (d) 40 *min*.

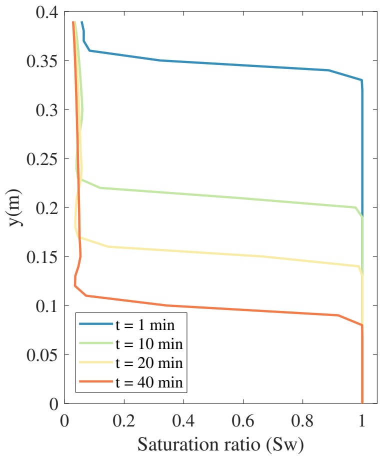

Figure 5.15: Plots of the (*suGWFoam*) simulated saturation ratio (Sw) along cross-section x = -1 m at time t = 1, 10, 20 and 40 min.

5.6 Comparison between *porousInterFoam* solver and *suGWFoam* solver for steady drainage from porous media

In this section, the simulation results for the steady drainage case using *porousInterFoam* solver (NS) and *suGWFoam* solver (RE) are presented. The simulation and experiment setup are the same as described above for the transient case except that water level in the clear water zone is kept constant at 0.35 m. The boundary condition in the simulations is adjusted accordingly. It can be seen in Figure 5.16 that the phreatic surfaces obtained from the two solvers are the same and match well with the measurement.

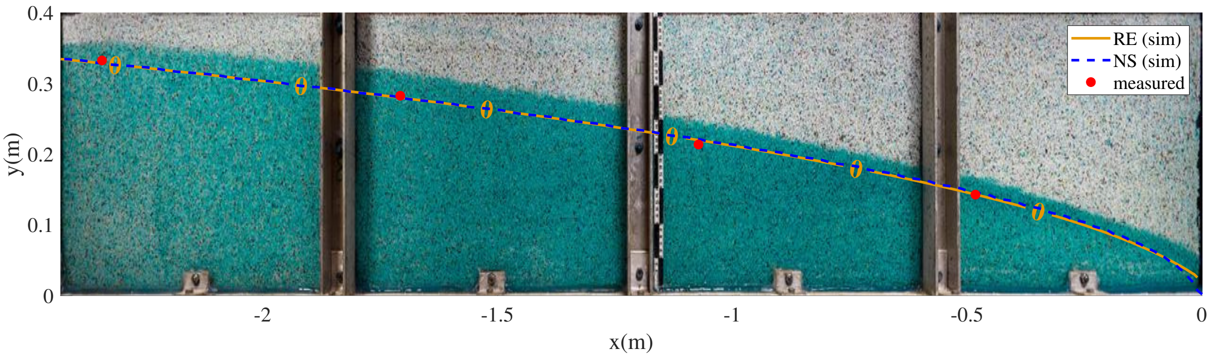

Figure 5.16: Plots of the simulated phreatic surfaces obtained from *porousInterFoam* solver (NS) and *suGWFoam* solver (RE) and the manometer measurement over snapshots of the experiment of steady drainage from porous media.

CHAPTER 6

SATURATED GRANULAR DAM-BREAK FLOWS

This chapter presents a numerical model *porousMixtureInterFoam* obtained by coupling *interFoam* for mixture flows and *porousInterFoam* for porous flows. The governing equations for each solver and the coupling algorithm are described in detail. The constitutive relation for the mixture and cohesion of granular material in partially saturated conditions are discussed. The coupled model (*porousMixtureInterFoam*) is validated using the saturated granular dam-break flow experiment conducted in the dam-break facility of NCCHE at the USDA-ARS National Sedimentation Laboratory in Oxford, Mississippi. Comparisons of numerical and experimental results are presented.

6.1 The coupled solver (*porousMixtureInterFoam*)

The *porousMixtureInterFoam* is the coupled solver between *interFoam* for flows of grain-fluid mixture and *porousInterFoam* for porous media flows. For modeling grain-fluid mixture flows, the differences in the governing equations used in dry granular flows in Chapter 4, and saturated granular flow in this Chapter are that: (i) The diffusion stress term is included for saturated granular flow (see Section 2.4 for details), (ii) the effective viscosity used in this Chapter includes both a frictional term and a viscous term, and (iii) the frictional part of the effective viscosity takes into account the effect of interstitial water through pore water pressure. This pore water pressure is obtained from the *porousInterFoam* solver. Details of governing equations for both solvers are presented below as well as the coupled algorithm.

6.1.1 Governing equation for mixture flows

As described in Section 2.4, the governing equation of the grain-fluid mixture can be obtained by adding the mass and momentum balance equations of the solid phase and the fluid phase. The resulting equation has the form similar to the equation of homogeneous mixture except the extra term ($\bigtriangledown \cdot \boldsymbol{T}'$) which is called the diffusion stress term. The mass and momentum equations can be written as follow:

$$\frac{\partial \rho}{\partial t} + \bigtriangledown \cdot (\rho \mathbf{u}) = 0 \tag{6.1}$$

$$\frac{\partial \rho \mathbf{u}}{\partial t} + \bigtriangledown \cdot (\rho \mathbf{u}\mathbf{u}) = \rho \mathbf{g} + \bigtriangledown \cdot (\boldsymbol{T}_s + \boldsymbol{T}_f + \boldsymbol{T}') \tag{6.2}$$

where $\boldsymbol{T}_s$ and $\boldsymbol{T}_f$ are the stress tensors of the solid and liquid phases,

$$\boldsymbol{T}' = -\phi_s \rho_s (\mathbf{u}_s - \mathbf{u})(\mathbf{u}_s - \mathbf{u}) - \phi_f \rho_f (\mathbf{u}_f - \mathbf{u})(\mathbf{u}_f - \mathbf{u}), \tag{6.3}$$

ρ is the mixture density and $\mathbf{u}$ is the velocity defined by

$$\rho = \phi_s \rho_s + \phi_f \rho_f, \tag{6.4}$$

$$\mathbf{u} = \frac{\phi_s \rho_s \mathbf{u}_s + \phi_f \rho_f \mathbf{u}_f}{\rho} \tag{6.5}$$

Implementation of the mixture model in OpenFOAM is fairly straightforward. The *interFoam* solver can be used to solve the velocity ($\mathbf{u}$) and pressure (p) of the mixture. The diffusion stress term has to be added to the momentum equation of *interFoam.* To calculate this term, velocity of water ($\mathbf{u_f}$) is obtained from the *porousInterFoam* solver and the grain velocity ($\mathbf{u_s}$) is then computed using equation 6.5.

6.1.2 Viscous shear stress of the mixture

In the case of a dry granular flow where interstitial fluid plays no significant role in the dynamic of the flow, it can be seen in Chapter 4 that, the simulation results show a good agreement with the experiments by using the effective viscosity defined as

$$\eta_{eff}(\|\boldsymbol{D}\|, p) = \frac{\mu p}{\|\boldsymbol{D}\|} \tag{6.6}$$

where $\|\boldsymbol{D}\|$ is second invariant of the strain rate tensor, μ is analogous to a coefficient of friction ($\mu = \tan\phi$, ϕ is the internal friction angle), and p is the total mixture pressure.

In the case of initially saturated grain-fluid mixture, the total mixture pressure (p) is replaced by the effective inter-particle normal stress (p_{eff}) which is approximated by taking the total mixture pressure and subtracting the pore water pressure (p_w) from it, yielding $p_{eff} = p - p_w$. This definition of effective stress correspond to Terzeghi's effective stress. The effective viscosity can be defined as:

$$\eta_{eff}(\|\boldsymbol{D}\|, p) = c + \frac{\mu p_{eff}}{\|\boldsymbol{D}\|} + k(\|\boldsymbol{D}\|)^{n-1} \tag{6.7}$$

where k is the consistency index, n is the flow index and c is the cohesion (see Section 6.1.3). The effective viscosity for the mixture is then the sum of a frictional term and a viscous term. The flow index $n = 0.33$ is chosen. The consistency index is a model calibration parameter. In this study, $k = 0.3$ gives promising results. The pore water pressure (p_w) is obtained by solving porous media flows through the mixture which is given in details in Section 6.1.4.

6.1.3 Cohesion of granular materials under variably saturated conditions

In soil mechanics and continuum mechanics, cohesion refers to shear resistance or strength under zero normal stress (Lu and Likos [54]). However, cohesion, by definition, is the stress or act of sticking together. This stress provides resistance to externally applied stress that is manifest in the form of either tensile or shear stress. In the form of shear stress,

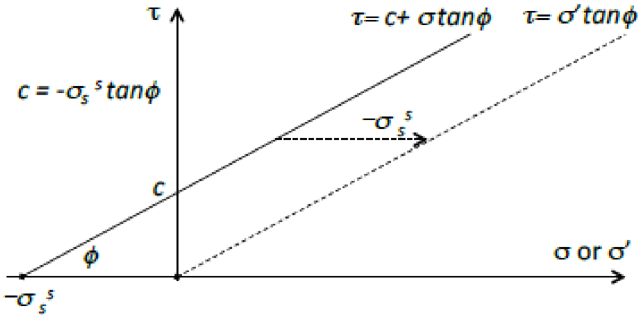

Figure 6.1: Relation between cohesion and isotropic tensile stress in saturated granular media. Picture taken from Lu and Likos [54].

it is cohesion (shear resistance) while isotropic tensile stress refers to normal resistance. The relation (see Figure 6.1) between cohesion and isotropic tensile stress is that cohesion (c) is the mobilized shear resistance of isotropic tensile stress (σ_s^s) mechanically through the internal friction angle (ϕ):

$$c = -\sigma_s^s \tan\phi \tag{6.8}$$

The shear strenght parameters, cohesion and friction angle, define the Mohr-Coulomb fail criterion:

$$\tau = (\sigma - \sigma_s^s)\tan\phi = \sigma' \tan\phi \tag{6.9}$$

where τ is the shear strength, σ is the total stress and σ' is the effective stress.

For variably saturated granular media, cohesion is caused by inter-particle physico-chemical forces (van der Waals, electric double layer repulsion and cementation) and capillary force. The isotropic tensile stress due to all these mechanisms is conceptualized as suction stress (Lu and Likos [55]). This suction stress is highly dependent on material type and degree of saturation, shown in Figure 6.2. For sandy soil, suction stress is zero for dry and fully saturation but could reach several kPa in minimum at intermediate saturation. For silty soil, suction stress is not zero at both dry and fully saturated conditions and, at intermediate saturation, it can reach several tens of kPa. For clayey soil, suction stress is maximum at fully saturated condition but decreases as saturation decreases. The PET pallets used in

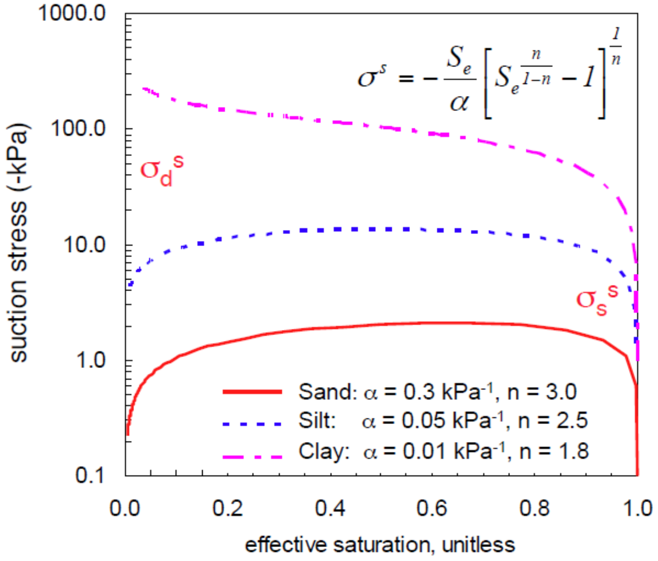

Figure 6.2: The suction stress characteristic curve (SSCC) for various soil types. Picture taken from Lu and Likos [54].

Rébillout et al. [74] is a coarse material with diameter of 2.867 mm. The suction stress would fall into the rang of sandy soil type with the values ranging from about 0 to 1 kPa.

6.1.4 Governing equation for porous flows

The macroscopic governing equations for flows in porous media derived by Wang et al. [85] are employed (see details in Section 5.1). The equations are written as follow:

$$\bigtriangledown \cdot \mathbf{u}_w = 0 \tag{6.10}$$

$$\frac{\partial\left(\rho_f \mathbf{u}_w\right)}{\partial t} + \bigtriangledown \cdot \left(\rho_f \mathbf{u}_w \mathbf{u}_w\right) = -\bigtriangledown p_w + \mu \bigtriangledown \cdot \left[\bigtriangledown\left(\mathbf{u}_w\right) + \left[\bigtriangledown\left(\mathbf{u}_w\right)\right]^T\right] + \mathbf{F} \tag{6.11}$$

where ρ_f is the fluid density, $\mathbf{u}_w$ is the intrinsic phase average velocity, p_f is the pressure, μ is the dynamic viscosity and $\boldsymbol{F}$ is the total body force including the resistance from the porous medium and other external forces and defined by

$$\mathbf{F} = -\frac{\mu n}{K}\left(\mathbf{u}_w - \mathbf{u}_s\right) + \rho_f \mathbf{g}. \tag{6.12}$$

6.1.5 The coupled algorithm

In order to couple *interFoam* and *porousInterFoam*, a python library was developed to integrate the two solvers into a main program. Detailed relationship of the coupled algorithm is presented in Figure 6.3. In the flowchart, after the main program starts, geometry, parameters, constants and coefficients are initialized. At half time step of the mixture solver (*interFoam*), the porous flow model (*porousInterFoam*) is solved. At this stage, pore water pressure (p_w) is obtained and sent to the mixture model to calculated the viscous shear stress. Then, the mixture model is solved for grain-fluid mixture flow. At this stage, geometry of the porous medium and mixture velocity are obtained and sent back to the porous flow model. These steps continue until the simulation ends.

6.2 Experimental setup

Figure 6.4: PET pellets.

One of the experiments [74] conducted in the dam-break facility of NCCHE at the USDA-ARS National Sedimentation Laboratory in Oxford, Mississippi is used to validate the coupled model. In this experiment, the channel consisting of a 0.5 m width, 0.6 m height and 7.6 m length was divided by a sliding gate into: (i) a 3.24 m length of upstream reservoir, and (ii) a 4.36 m length of dam-break channel. The PET pellets used in the experiment and the experimental setup are shown in Figure 6.4 and Figure 6.5. Some of the intrinsic and bulk properties of the material are summarized in Table 6.1. In the table, D_m is the mean nominal, Sf is the shape factor, diameter, n is the porosity, ρ_{PET} is the density of the PET pellets, K the (packed) hydraulic conductivity, and ϕ is the friction angle. At the beginning of the experiments, the sliding gate is pulled upward with a speed of about 8 m/s to release the mixture of PET pellets and water to downstream. Blue dye was added to the water in order to facilitate the tracking of the phreatic surface by

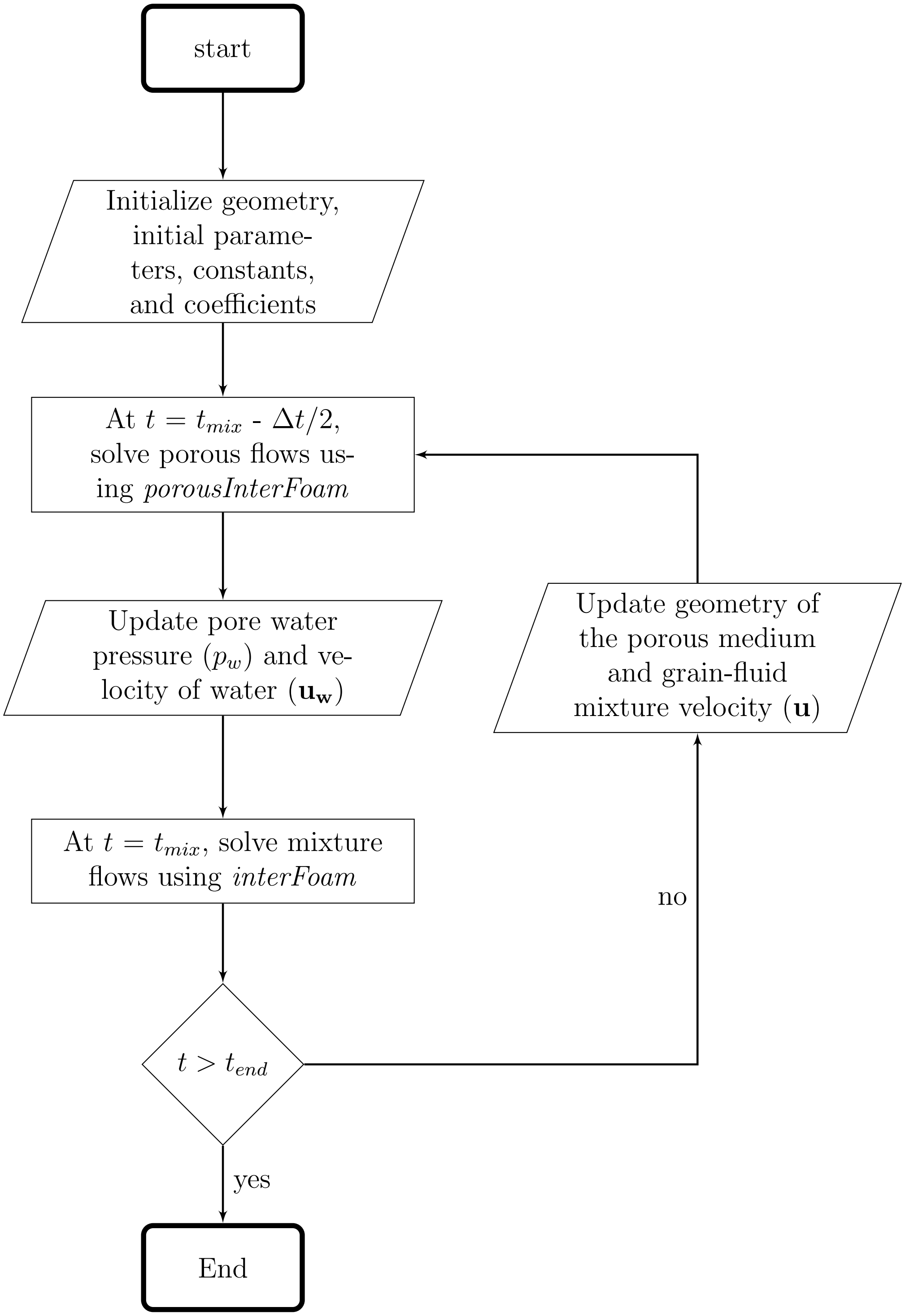

Figure 6.3: Detailed relationship of *porousMixtureInterFoam* algorithm.

imaging techniques. The flow fields in the upstream reservoir and the downstream channel were recorded using two and four high-speed cameras, respectively.

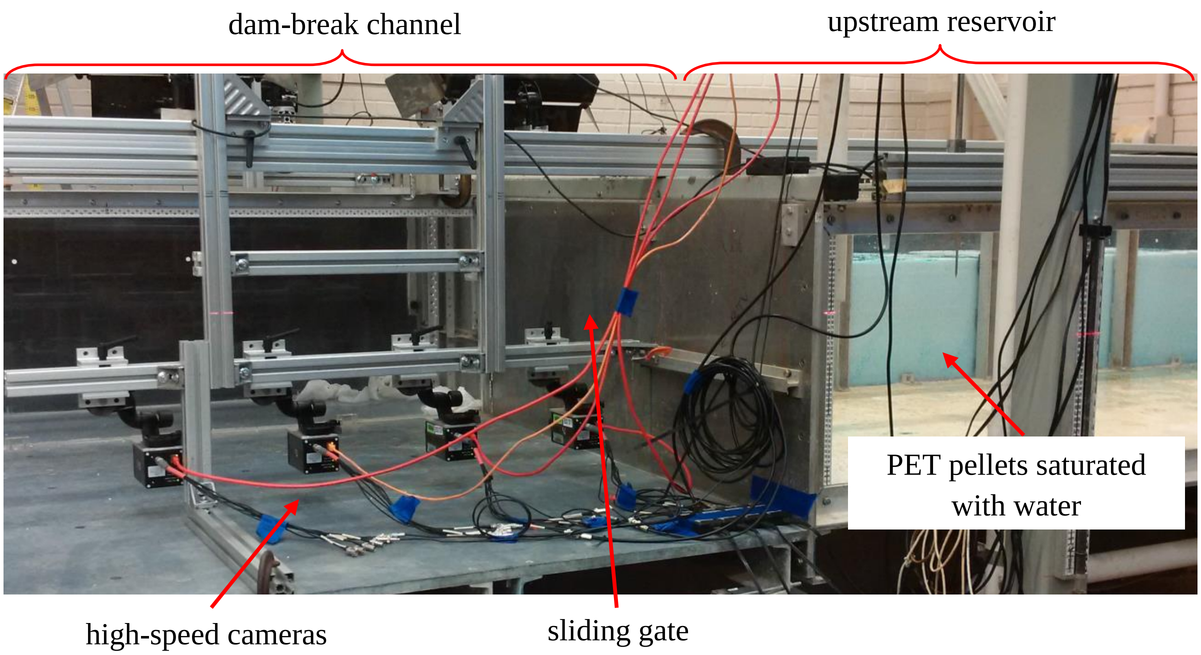

Figure 6.5: Experimental setup (Rébillout et al. [74]).

Table 6.1: Properties of the PET pellets (Ozeren et al. [67]).

d_{10} (mm)	d_{50} (mm)	d_{90} (mm)	D_m (mm)	Sf	n (packed)	ρ_{PET} (kg/m^3)	K (mm/s)	ϕ $(°)$
2.812	2.867	2.920	2.861	0.832	0.34	1422	21	30

6.3 Simulation setup

In the numerical simulation, the 3.93 m-long and 0.5 m-high computational domain (Figure 6.6) is initialized as two zones with different initial properties: (i) the mixture zone containing PET pellets saturated with water, and (ii) the empty cell zone. This domain is used for both the *interFoam* solver for mixture flow and the *porousInterFoam* solver for flow in porous media. In the mixture flow model, the wall boundary condition is used for the left boundary while atmosphere and open boundary conditions are used for the top and right boundaries. At the bottom, the Coulomb slip boundary condition is employed. For

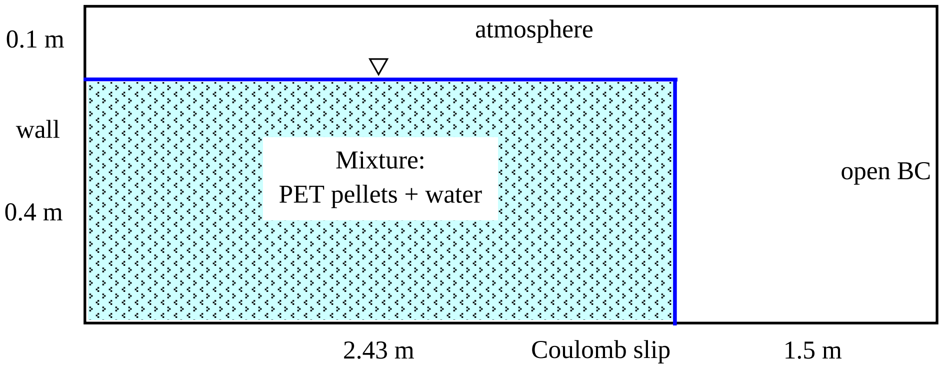

Figure 6.6: Computational domain (The boundary conditions shown in the Figure are for the mixture flow model (*interFoam*)).

the porous flow model, boundary conditions are the same as the mixture model except at the bottom where the slip boundary condition is used. For both solvers, the time step is set to 0.001 s while the cell size is 0.01 m. The parameters used in the mixture model are shown in Table 6.2. For the porous model, in Equation 6.12, porosity (n) is 0.34 and permeability is 2.4×10^{-9}. However, in the region where mixture velocity is greater than 0.01 m/s, porosity is set 0.42 and permeability is set to 2.4×10^{-8}. Comparison between simulation and experimental results are presented in the following section.

Table 6.2: Parameters used in the mixture model.

Particle diameter (mm)	Material density (kg/m^3)	Volume fraction	Repose angle (°)	Consistency index	Flow index	Cohesion (Pa)
2.867	1422	0.66	30, 35	0.3	0.33	0, 0.3, 0.5

6.4 Simulation results

This section presents simulation results of saturated granular dam-break flow obtained from the coupled solver *porousMixtureInterFoam* in comparison with the experiment conducted by Rébillout et al. [74]. In Section 6.4.1, the mixture profiles obtained from the simulations with different values of cohesion are presented along with the experimental results. Velocity vectors and magnitudes obtained from the simulation is presented in Section

6.4.2. In Section 6.4.4, the mixture profiles obtained from the simulations with different values of angle of repose are presented along with the experimental results. In Section 6.4.3, comparisons between the mixture profiles and the phreatic surfaces obtained from the simulation and the experiment are presented.

6.4.1 Mixture profiles and front propagation for different values of cohesion

To obtain simulation results for this section, the model parameters described above are used in the simulation runs. Angle of repose (ϕ) is set to 35°. Theoretically, the angle of repose is approximately equal to the macroscopic material internal friction angle. In the experiment, the angle of repose was measured and the value of $\phi = 30°$ was obtained. However, by using the direct shear test, the values of internal friction angle range from 31° to 35° were obtained. In the numerical simulation, $\phi = 35°$ gives better results. Sensitivity test of ϕ is presented in Section 6.4.4.

To investigate the effect of cohesion, the value of c in Equation 6.8 is set to 0, 0.3 and 0.5 Pa. The case with $c = 0$ corresponds to dry condition, meaning that the zone above the phreatic surface is assumed dry. When $c = 0.3$ Pa or $c = 0.5$ Pa, this zone is assumed partially saturated condition, and the values of suction stress (σ^s) obtained from Equation 6.8 are 0.43 and 0.71, respectively. These values of suction stress are within the range obtained for coarse particles like sandy soil (see Section 6.1.3). The simulation and experimental results are shown in Figure 6.7.

Figures 6.7(a)-(d) show that the mixture profiles obtained from the simulation with different values of cohesion are similar except at the locations near $x = 0$. There is no difference in the front propagation and only slightly difference in the slope of the mixture. However, at time $t = 1.2$ s (Figure 6.7(e)), the difference in the slope of the profiles can be observed. For higher values of cohesion, the slopes are steeper. This can also be seen in the final deposit at time $t = 2.5$ s (Figure 6.7(f)). Moreover, the difference is found in the run-out distances. The higher the value of cohesion, the less the run-out distances.

The saturated granular dam-break experiment by Rébillout et al. [74] used to study in this case was packed to an initial volume fraction of solid around 0.66. This solid volume fraction is greater than a solid volume fraction in the critical state in the context of Critical State Soil Mechanics (Schofield and Wroth [80]). The critical state refers to the condition in which no volume change occurs when undergoes shearing deformation. The critical state at low confining pressure corresponds to a solid volume fraction of around 0.55 for uniform sized spheres. If the material is initially under an over-consolidated condition, then dilation will occur when the material is subject to a shearing deformation (Savage et al. [78]). Due to the dilation, the pore volume increases giving rise to a negative pore pressure. The negative pore pressure causes a positive contribution to the effective stress and produces an increase in the effective Coulomb shear strength. This could explain the delay in the collapse observed in the early stage of the experiment. This delay is quantified in Figure 6.8.

In the simulation, the model is not able to capture the delayed response of the mixture in the early stage of the collapse process as can be seen in Figure 6.7(a)-(b) and in Figure 6.8, the front in the simulations start moving at time about 0.1 s as compared to 0.3 s in the experiment. This may be partly due to the fact that the model does not account for dilation. The pore water pressure dissipation in the early stage of the collapse process is not appropriately simulated by the model (see Section 6.4.3). As suggested by George and Iverson [24] that granular dilation causes dissipation of pore pressure, thus further stabilizing granular flow motion. Although cohesion of granular material in partially saturated zone is included, it is not enough to describe this high viscous behavior in the early stage. Moreover, the effect of dilation should also be considered in the constitutive model for the mixture. Although the model fails to capture this behavior, it can predict well the front propagation as shown in Figure 6.8. As shown in Figure 6.7(f), the final profile is also well captured. Another important difference between the simulation and the experiment is concave and convex fronts. The simulation shows more fluid-like behavior with friction at the bottom.

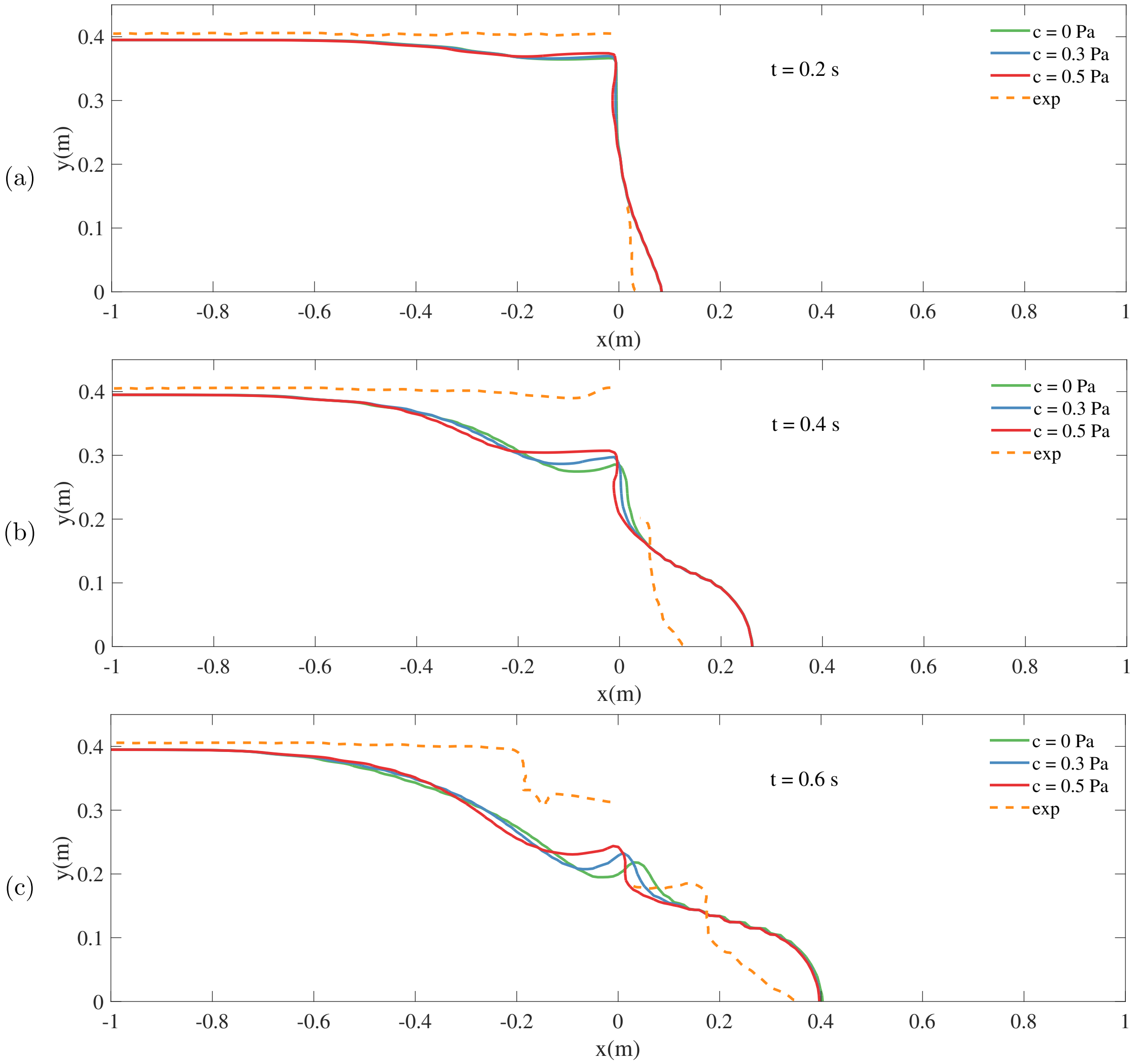

Figure 6.7: Comparison of the mixture profiles between the simulations with different values cohesion (c) and the experiment time 0.2, 0.4 and 0.6 s.

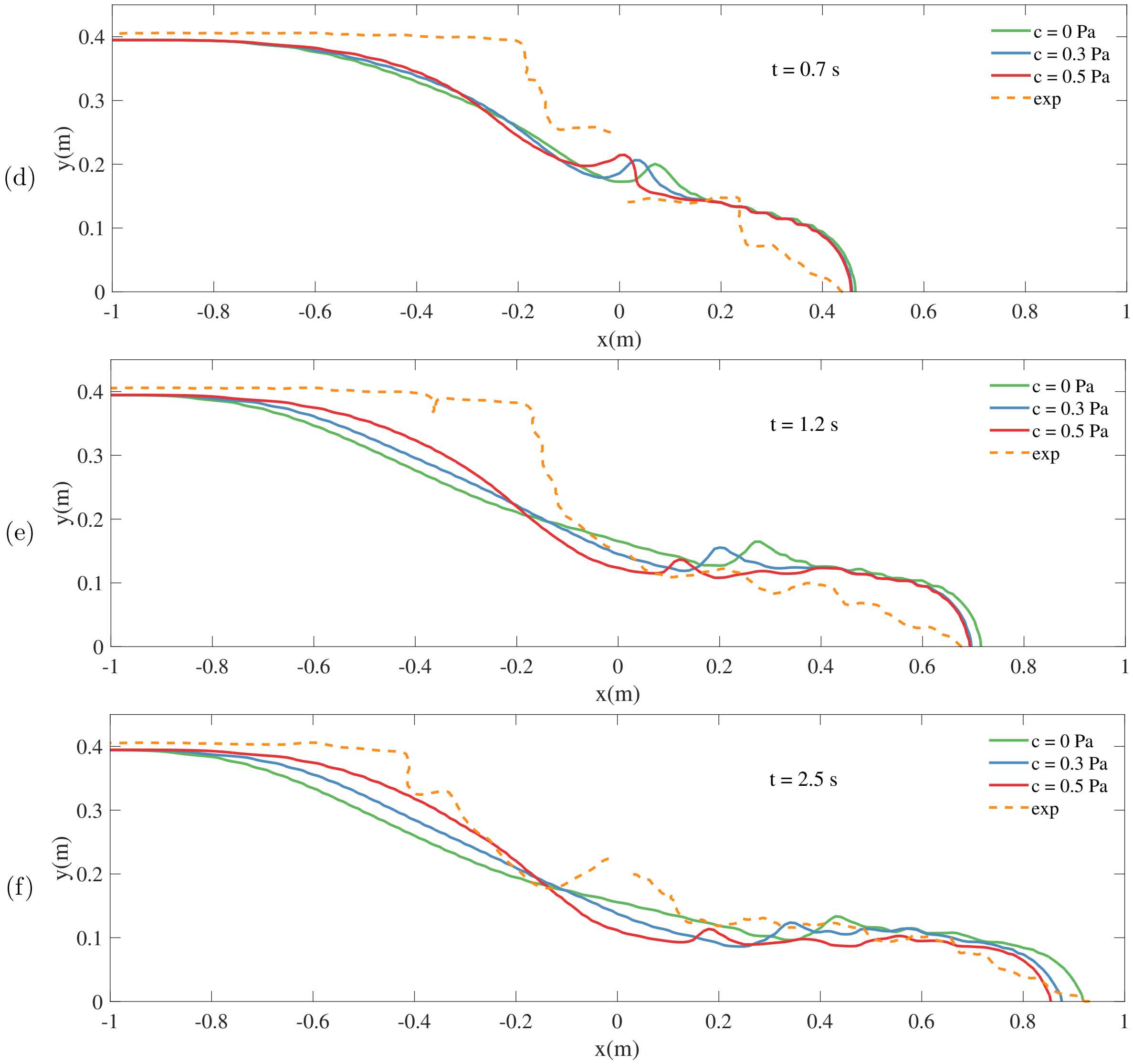

Figure 6.7: Comparison of the mixture profiles between the simulations with different values of cohesion (c) and the experiment time 0.7, 1.2 and 2.5 s.

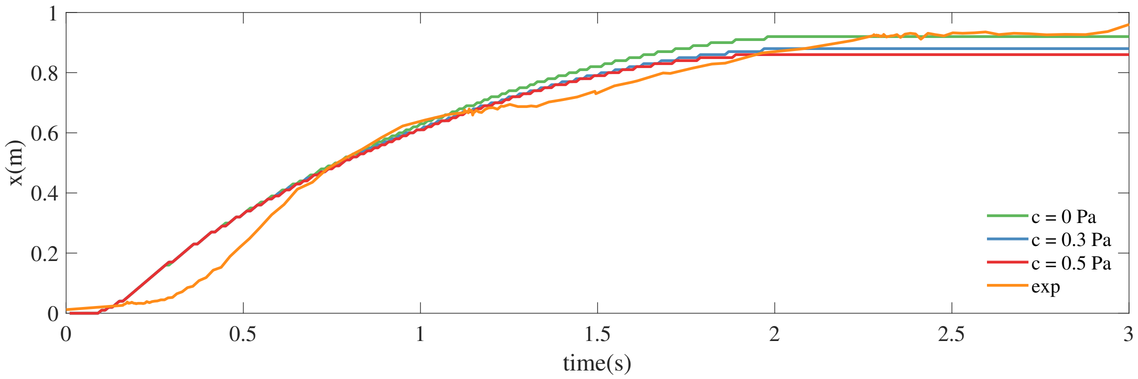

Figure 6.8: Propagation of the fronts for the simulations with different values of cohesion (c) and the experiment.

6.4.2 Velocity vectors and velocity magnitudes

Figure 6.9 shows velocity vectors and velocity magnitudes obtained from the simulation with $c = 0.5$ Pa at time 0.4, 0.6, 0.7 and 1.2 s. In all figures, the maximum velocities concentrate near the front of the mixture. In the downstream of the gate location ($x > 0$), horizontal velocity is dominant while in the upstream the flow is in both horizontal and vertical downward directions. At time $t = 0.4$ s, the maximum velocity is about 0.8 m/s. Later, the maximum is about 0.6, 0.5 and 0.4 m/s at time 0.6, 0.7 and 1.2 s, respectively.

6.4.3 Mixture profiles and phreatic surfaces

As the mixture falls downwards and spread horizontally, motion of interstitial water occurs in the same regions as the moving mixture. Figure 6.10 shows the mixture profiles and phreatic surfaces of the simulation and the experiment at different times. At time $t = 0.2$ s (Figure 6.10(a)), water level in the simulation near the gate location ($x = 0$) drops below the mixture height. The shape of the water profile is similar to that of the mixture. At time $t = 0.4$ s (Figure 6.10(b)), the shape of the simulated water surface follows the shape of the mixture. The mixture front in the simulation is saturated with water, while in the experiment the mixture moves with the dry front. This may be to a dilation of dense granular material when the material is subjected to a shearing deformation. As a result of the dilation, the interstitial pore volume is increased giving rise to water to be drawn into

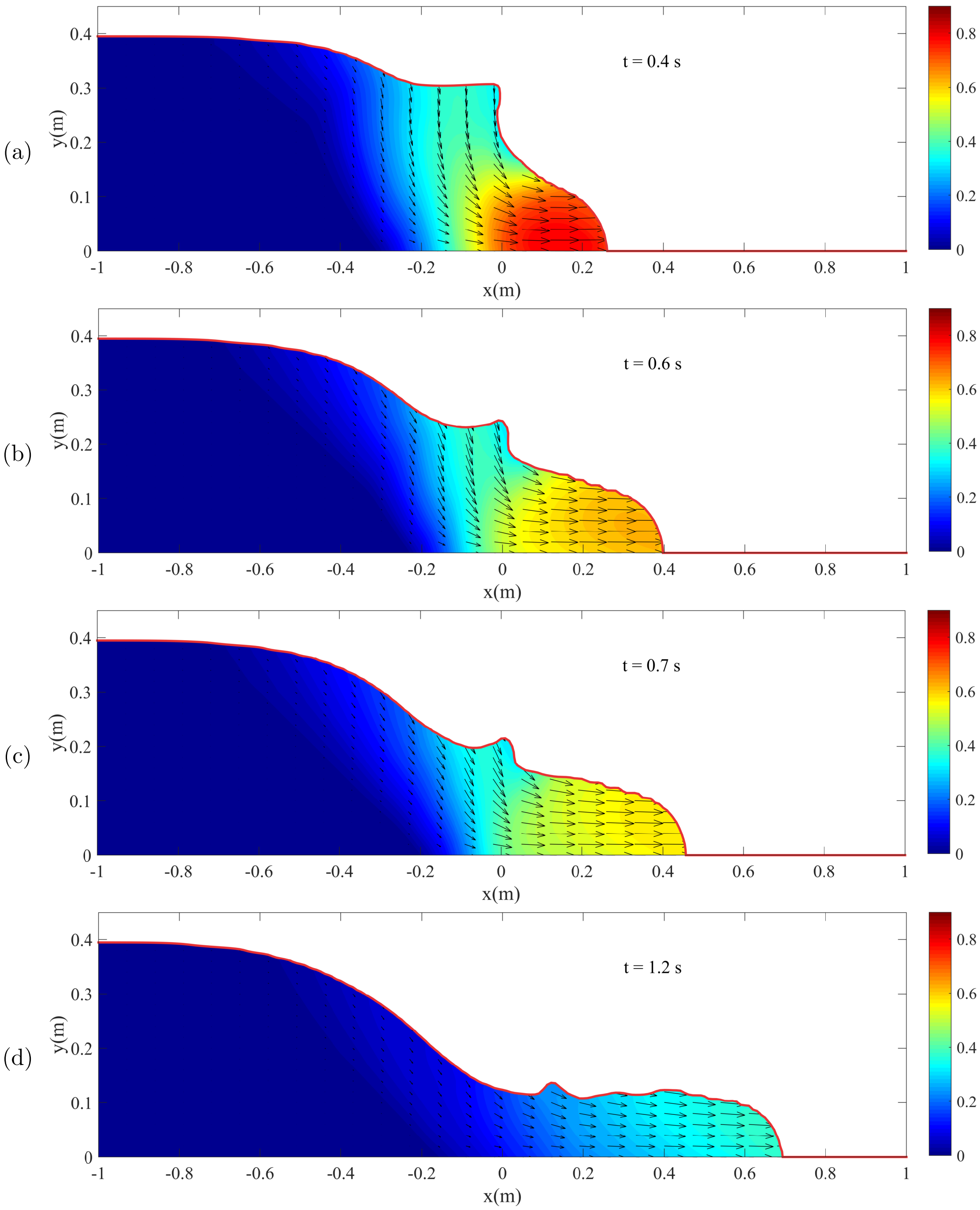

Figure 6.9: Velocity vectors and velocity magnitudes obtained from the simulation at time 0.4, 0.6, 0.7 and 1.2 s.

the interstitial space. Since the model does not include this effect, it cannot capture well this phenomenon, especially in the early stage of the flow. However, at later time $t = 0.8$ s (Figure 6.10(d)), the simulated water profile matches with the experiment.

6.4.4 Mixture profiles for different values of angle of repose

Figure 6.11 shows the mixture profiles obtain from the simulation with different values of angle of repose (ϕ) and the experiments at time 0.7, 1.2 and 2.5 s. At time 0.7 and 1.2 s, the fronts of the mixture in the simulations and the experiment are in the same location. However, at time $t = 2.5$ s, the run-out distance is more in the simulation with $\phi = 30°$. This result agree with the simulation of dry granular flow presented in Section 4.10.1 in that a decrease of ϕ increases the displacement and decreases the column height. The final profile of the simulation with $\phi = 35°$ is closer to the experiment than the final profile of the simulation with $\phi = 30°$.

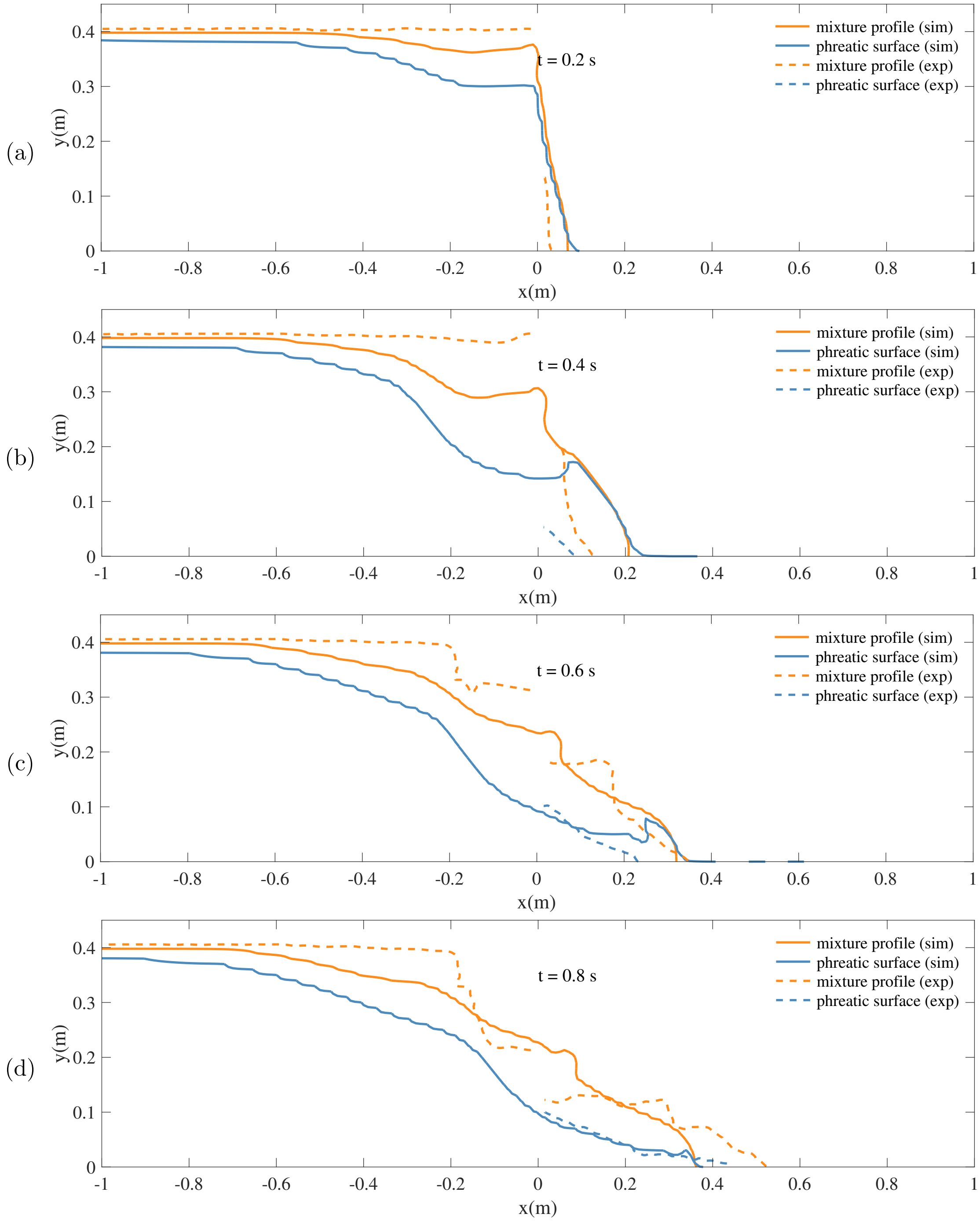

Figure 6.10: Comparison of the mixture profiles and the phreatic surfaces between the simulation and the experiment at time $t = 0.2$, 0.4, 0.6 and 0.8 s.

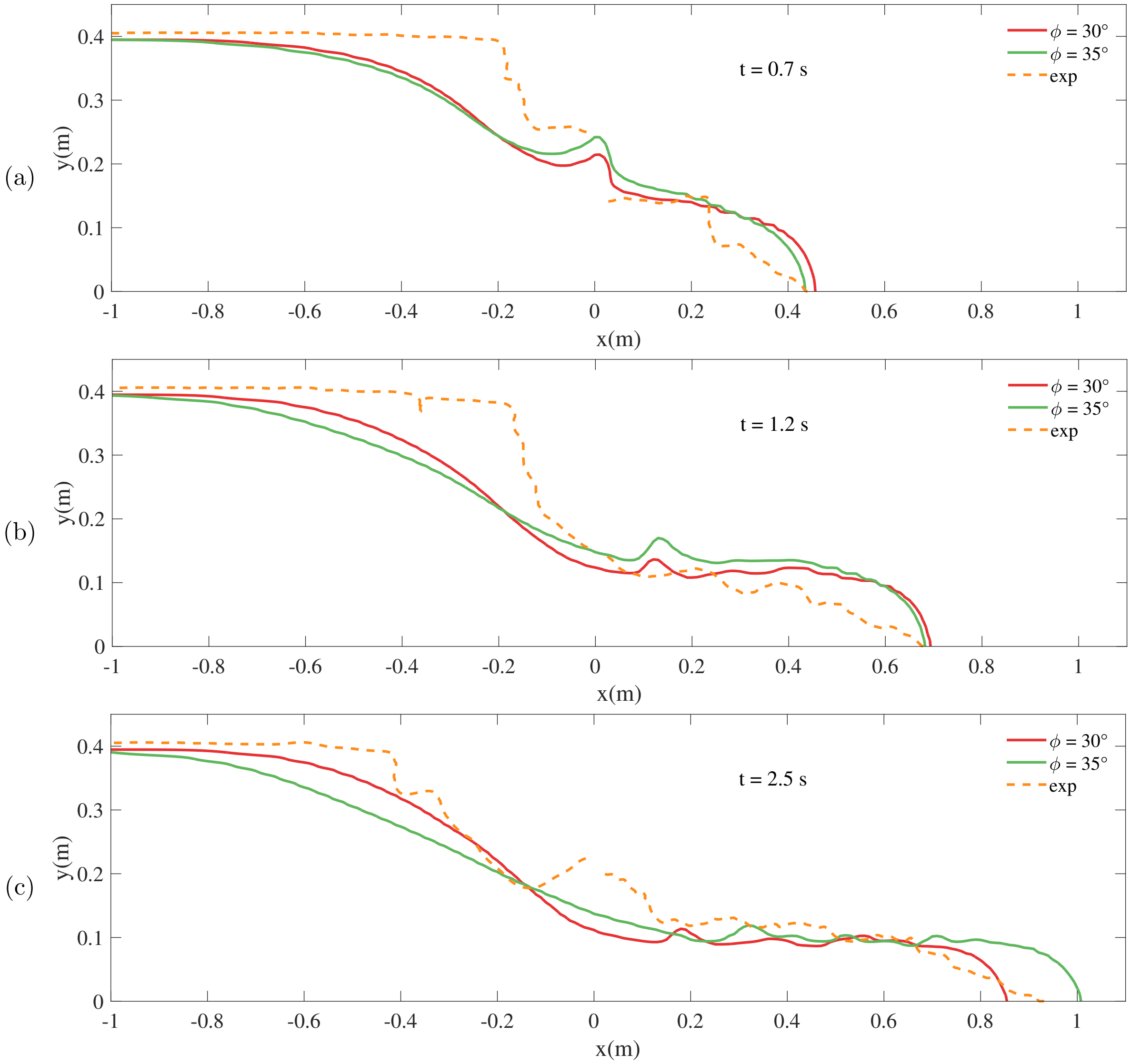

Figure 6.11: Comparison of the mixture profiles between the simulations with different values of angle of repose (ϕ) and the experiment time 0.7, 1.2 and 2.5 s.

CHAPTER 7

SUMMARY, CONCLUSION, AND FUTURE RESEARCH

7.1 Summary and conclusion

In this PhD dissertation, the main focus is on the development of a coupled numerical model for dam-break flows of saturated granular materials. The coupled model is built using the existing solvers in OpenFOAM. The two main solvers used in this study are the *interFoam* for grain-fluid mixture flows, and the *porousInterFoam* for flows in porous media. These two solvers solve the governing equations analogous to the Navier-Stokes equations with additional terms and different physical interpretation of an existing term. To accomplish the task, it is divided into three main parts. First, dry granular dam-break flow model is studied and compared with laboratory experiments. These cases represent granular flows where an interstitial fluid plays no significant role in the dynamic of the flows. The homogeneous model is employed for this case. Second, porous media flows through a static medium are studied. Third, the coupled model of grain-fluid mixture flows and porous media flows is developed by using the elements developed in the first and second phases to study saturated granular dam-break flows. The mixture model is adopted, leading to an additional term called the diffusion stress term.

For dry granular dam-break flows, the *interFoam* solver with some modifications is used in the study. Two new modules for constitutive relations: the constant friction model (Coulomb-type model) and the μ(I) rheology model are implemented in OpenFOAM. A python library is developed to simulate movement of the sliding gate and used to investigate the influence of the gate on granular dam-break flow problems. The model is validated using several laboratory experiments of dry granular dam-break flows with different granular materials. The comparisons between the simulated and measured granular mass profile and front propagation are in good agreement, indicating the successful application of the model.

In the study of flows through static porous medium, the two solvers: *porousInterFoam* and *suGWFoam* are used. The difference between the two solvers is that the *porousInterFoam* solves the Navier-Stokes equation with a pressure drop term while the *suGWFoam* solves the nonlinear Richards' equation. By using the Navier-Stokes solver, flows in both the clear water zone and the porous zone can be solved with the same set of equations. This capability is not directly obtained by using the Richards' equation solver. However, if the interest is to focus on modelling partially saturated zone, the Richards' equation solver has to be used. In the *porousInterFoam*, the approach to define a porous zone and it properties is modified so that the solver can be used in the case of deforming porous medium. The seepage boundary condition is implemented in *suGWFoam*. Both solvers are tested against laboratory experiments of steady and transient drainages from porous medium. The results show that the phreatic surfaces are well captured by the models, which reveals the capability of the solvers to solve porous media flows. Due to difficulty in treating clear water zone and moving boundary condition using the Richards' equation, the Navier-Stokes solver is chosen to couple with the mixture model in the next task.

The coupled numerical model developed in this study is based on the mixture theory in which the solid and fluid constituents are kept distinct and a two-phase mixture is assumed. The resulting governing equation is different from that obtained from the homogeneous model with an additional term called a diffusion stress term. A response from the interstitial fluid and the solid phase is taken into account, leading to decomposing the normal stress as an effective stress and pore fluid pressure. This pore pressure is obtained from the porous medium solver. In this way, the mixture solver and the porous solver are coupled and exchange necessary information. Apparent cohesion in the partially saturated zone is considered. The coupled model is validated against laboratory experiment. The mixture profiles and front propagation obtained from the simulations and the experiment show a good agreement, which reveals the validity of the developed model to simulate saturated granular dam-break flows.

7.2 Future Research

1. It can be seen in Figure 7.1 and 7.2 that, in the experiment, volume of the mixture gained in the downstream floodplain is greater than volume of the mixture lost in the upstream reservoir while there is no different between the two in the simulation. Thus, some further effort should be devoted to the development of mixture model and constitutive relationship that could describe the behavior of dense granular flow. The mixture model should allow for the increase in volume of the mixture. The constitutive relationship should include effect of dilation and be capable of exhibiting the very high viscosity of the grain-fluid mixture causing the delayed collapse during the early stage of the flow.

2. The modeling of variably saturated flows using a two-phase approach such as Richards' equation solver will be challenging task when the medium is deforming. This would require treating moving boundary condition to locate the free surface of the porous medium. Moreover, when coupling with the mixture model, the effective stress in the viscous stress term need to be redefined. In a partially saturated material, the stress state is not only defined by the effective stress but also the so-called suction stress (Lu et al. [53]).

3. The developed model can be applied to simulate a real event of geophysical flows and tailings dam-break flows to test its performance. This would require increasing the number of cells in the model and thus increase the computational cost significantly. The simulations in the current study are run on a desktop PC with single processor. For

larger simulations, it is suggested to use computer cluster to carry out the simulation and enable parallel functionality of OpenFOAM.

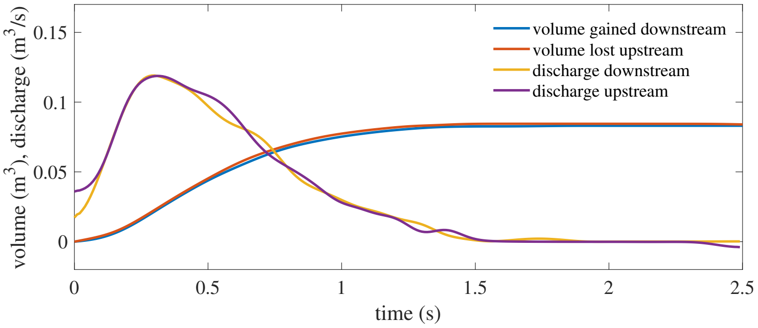

Figure 7.1: Time series of volume gained downstream, volume lost upstream, discharge downstream, and discharge upstream of the gate obtained from the simulation.

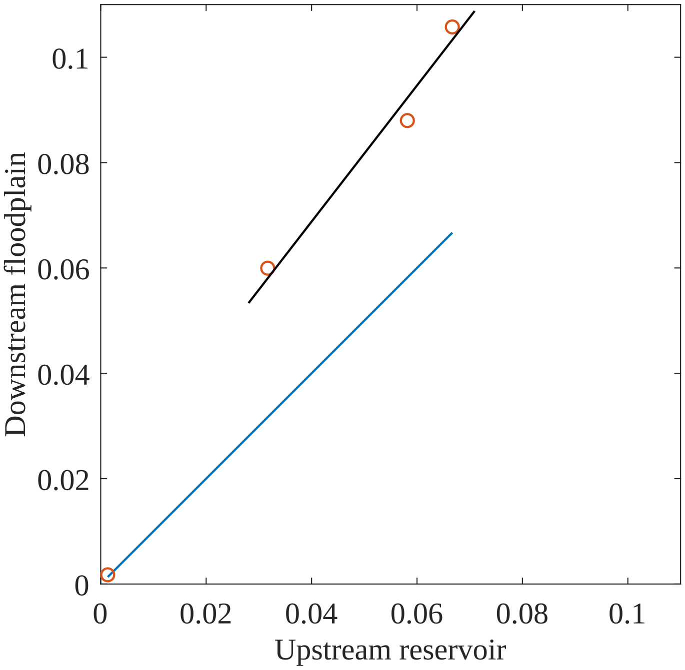

Figure 7.2: Comparison between volume gained downstream and volume lost upstream of the gate obtained from the experiment by [74].

BIBLIOGRAPHY

[1] Aronne Armanini. “Granular flows driven by gravity”. In: *Journal of Hydraulic Research* 51.2 (2013), pp. 111–120.

[2] RJ Atkin and RE Craine. “Continuum theories of mixtures: basic theory and historical development”. In: *The Quarterly Journal of Mechanics and Applied Mathematics* 29.2 (1976), pp. 209–244.

[3] Ralph A Bagnold. “Experiments on a gravity-free dispersion of large solid spheres in a Newtonian fluid under shear”. In: *Proceedings of the Royal Society of London. Series A. Mathematical and Physical Sciences* 225.1160 (1954), pp. 49–63.

[4] Diego Berzi, James T Jenkins, and Michele Larcher. “Debris flows: Recent advances in experiments and modeling”. In: *Advances in Geophysics*. Vol. 52. Elsevier, 2010, pp. 103–138.

[5] Joseph P Beverage and James K Culbertson. “Hyperconcentrations of suspended sediment”. In: *Journal of the Hydraulics Division* 90.6 (1964), pp. 117–128.

[6] Eugene Cook Bingham. *Fluidity and plasticity*. Vol. 2. McGraw-Hill, 1922.

[7] R Byron Bird, Warren E Stewart, and Edwin N Lightfoot. *Transport phenomena*. John Wiley & Sons, 2007.

[8] R Brooks and T Corey. “HYDRAU uc properties of porous media”. In: *Hydrology Papers, Colorado State University* 24 (1964), p. 37.

[9] Michael A Celia, Efthimios T Bouloutas, and Rebecca L Zarba. “A general mass-conservative numerical solution for the unsaturated flow equation”. In: *Water resources research* 26.7 (1990), pp. 1483–1496.

[10] AW Cense and S Berg. “The viscous-capillary paradox in 2-phase flow in porous media”. In: *International Symposium of the Society of Core Analysts held in Noordwijk, The Netherlands*. 2009, pp. 27–30.

[11] S Márquez Damián. *Description and utilization of interfoam multiphase solver*. 2012.

[12] Renaud Delannay, Alexandre Valance, Anne Mangeney, Olivier Roche, and Patrick Richard. “Granular and particle-laden flows: from laboratory experiments to field observations”. In: *Journal of Physics D: Applied Physics* 50.5 (2017), p. 053001.

[13] Martin Depken, Jeremy B Lechman, Martin van Hecke, Wim van Saarloos, and Gary S Grest. “Stresses in smooth flows of dense granular media”. In: *EPL (Europhysics Letters)* 78.5 (2007), p. 58001.

[14] Joshua A Dijksman and Martin van Hecke. “Granular flows in split-bottom geometries”. In: *Soft Matter* 6.13 (2010), pp. 2901–2907.

[15] Daniel Charles Drucker and William Prager. “Soil mechanics and plastic analysis or limit design”. In: *Quarterly of applied mathematics* 10.2 (1952), pp. 157–165.

[16] Anders Elverhøi, Dieter Issler, Fabio V De Blasio, Trygve Ilstad, Carl Bonnevie Harbitz, and Peter Gauer. “Emerging insights into the dynamics of submarine debris flows”. In: *Natural Hazards and Earth System Science* 5.5 (2005), pp. 633–648.

[17] STEFANIA Evangelista, GIOVANNI de Marinis, CRISTIANA Di Cristo, and ANGELO Leopardi. “Dam-break dry granular flows: Experimental and numerical analysis”. In: *WSEAS Trans. Environ. Dev* 10 (2014), pp. 382–392.

[18] Rui Jorge Ferreira Aleixo, Sandra Soares Frazao, Mustafa Altinakar, and Yves Zech. “The Gate Removal Effect in the Initial Instants of the Dam-break Flow”. In: *Proceedings 35th World Congress International Association of Hydraulic Engineering and Research*. 2013.

[19] Abbas Firoozabadi and Donald L Katz. “An analysis of high-velocity gas flow through porous media”. In: *Journal of Petroleum Technology* 31.02 (1979), pp. 211–216.

[20] Ansys Fluent. “12.0 Theory Guide”. In: *Ansys Inc* 5.5 (2009).

[21] Philipp Forchheimer. “Wasserbewegung durch boden”. In: *Z. Ver. Deutsch, Ing.* 45 (1901), pp. 1782–1788.

[22] Yoël Forterre and Olivier Pouliquen. “Flows of dense granular media”. In: *Annu. Rev. Fluid Mech.* 40 (2008), pp. 1–24.

[23] Luigi Fraccarollo, Michele Larcher, and Aronne Armanini. “Depth-averaged relations for granular-liquid uniform flows over mobile bed in a wide range of slope values”. In: *Granular Matter* 9.3-4 (2007), pp. 145–157.

[24] DAVID L George and RICHARD M Iverson. “A two-phase debris-flow model that includes coupled evolution of volume fractions, granular dilatancy, and pore-fluid pressure”. In: *Italian Journal of Engineering Geology and Environment* 43 (2011), pp. 415–424.

[25] JD Goddard. “Dissipative materials as constitutive models for granular media”. In: *Acta Mechanica* 63.1-4 (1986), pp. 3–13.

[26] Isaac Goldhirsch. “Rapid granular flows”. In: *Annual review of fluid mechanics* 35.1 (2003), pp. 267–293.

[27] JMNT Gray, M Wieland, and K Hutter. “Gravity-driven free surface flow of granular avalanches over complex basal topography”. In: *Proceedings of the Royal Society of London A: Mathematical, Physical and Engineering Sciences*. Vol. 455. 1985. The Royal Society. 1999, pp. 1841–1874.

[28] Xinmei Hao, Renduo Zhang, and Alexandra Kravchenko. “A mass-conservative switching method for simulating saturated–unsaturated flow”. In: *Journal of hydrology* 311.1-4 (2005), pp. 254–265.

[29] Majid Hassanizadeh and William G Gray. “General conservation equations for multiphase systems: 1. Averaging procedure”. In: *Advances in water resources* 2 (1979), pp. 131–144.

[30] RG Hills, I Porro, DB Hudson, and PJ Wierenga. “Modeling one-dimensional infiltration into very dry soils: 1. Model development and evaluation”. In: *Water Resources Research* 25.6 (1989), pp. 1259–1269.

[31] Tobias Holzmann. “Mathematics, Numerics, Derivations and OpenFOAM®”. In: *Loeben, Germany: Holzmann CFD, URl: https://holzmann-cfd. de (visited on Nov. 29, 2017)* (2016).

[32] K Hutter, M Siegel, SB Savage, and Y Nohguchi. “Two-dimensional spreading of a granular avalanche down an inclined plane Part I. Theory”. In: *Acta Mechanica* 100.1-2 (1993), pp. 37–68.

[33] Kolumban Hutter. “Geophysical granular and particle-laden flows: review of the field”. In: *Philosophical Transactions of the Royal Society of London A: Mathematical, Physical and Engineering Sciences* 363.1832 (2005), pp. 1497–1505.

[34] Kolumban Hutter and Thilo Koch. “Motion of a granular avalanche in an exponentially curved chute: experiments and theoretical predictions”. In: *Phil. Trans. R. Soc. Lond. A* 334.1633 (1991), pp. 93–138.

[35] Fumitoshi Imaizumi, Satoshi Tsuchiya, and Okihiro Ohsaka. “Behaviour of debris flows located in a mountainous torrent on the Ohya landslide, Japan”. In: *Canadian Geotechnical Journal* 42.3 (2005), pp. 919–931.

[36] Ioan R Ionescu, Anne Mangeney, François Bouchut, and Olivier Roche. “Viscoplastic modeling of granular column collapse with pressure-dependent rheology”. In: *Journal of Non-Newtonian Fluid Mechanics* 219 (2015), pp. 1–18.

[37] Richard M Iverson. “Debris flows: behaviour and hazard assessment”. In: *Geology today* 30.1 (2014), pp. 15–20.

[38] Richard M Iverson. “The physics of debris flows”. In: *Reviews of geophysics* 35.3 (1997), pp. 245–296.

[39] Richard M Iverson and Roger P Denlinger. “Flow of variably fluidized granular masses across three-dimensional terrain: 1. Coulomb mixture theory”. In: *Journal of Geophysical Research: Solid Earth* 106.B1 (2001), pp. 537–552.

[40] Roy Jackson. *The dynamics of fluidized particles.* Cambridge University Press, 2000.

[41] Rashid Jamshidi and Luca Mazzei. "CFD Modeling of Fluidized Beds". In: *Reference Module in Chemistry, Molecular Sciences and Chemical Engineering* (2018).

[42] Hrvoje Jasak. "Error analysis and estimation for the finite volume method with applications to fluid flows." In: (1996).

[43] James T Jenkins and Stuart B Savage. "A theory for the rapid flow of identical, smooth, nearly elastic, spherical particles". In: *Journal of fluid mechanics* 130 (1983), pp. 187–202.

[44] Manuel del Jesus, Javier L Lara, and Inigo J Losada. "Three-dimensional interaction of waves and porous coastal structures: Part I: Numerical model formulation". In: *Coastal Engineering* 64 (2012), pp. 57–72.

[45] Jey K Jeyapalan, J Michael Duncan, and H Bolton Seed. "Investigation of flow failures of tailings dams". In: *Journal of geotechnical engineering* 109.2 (1983), pp. 172–189.

[46] Pierre Jop, Yoël Forterre, and Olivier Pouliquen. "A constitutive law for dense granular flows". In: *Nature* 441.7094 (2006), p. 727.

[47] David Kossoff, WE Dubbin, Maria Alfredsson, SJ Edwards, MG Macklin, and Karen A Hudson-Edwards. "Mine tailings dams: characteristics, failure, environmental impacts, and remediation". In: *Applied Geochemistry* 51 (2014), pp. 229–245.

[48] P-Y Lagrée, Lydie Staron, and Stéphane Popinet. "The granular column collapse as a continuum: validity of a two-dimensional Navier–Stokes model with a μ (I)-rheology". In: *Journal of Fluid Mechanics* 686 (2011), pp. 378–408.

[49] Guido Lauber and Willi H Hager. "Experiments to dambreak wave: Horizontal channel". In: *Journal of Hydraulic research* 36.3 (1998), pp. 291–307.

[50] X Liu. “Parallel modeling of three-dimensional variably saturated ground water flows with unstructured mesh using open source finite volume platform OpenFOAM”. In: *Engineering Applications of Computational Fluid Mechanics* 7.2 (2013), pp. 223–238.

[51] G Lois, A Lemaitre, and JM Carlson. “Emergence of multi-contact interactions in contact dynamics simulations of granular shear flows”. In: *EPL (Europhysics Letters)* 76.2 (2006), p. 318.

[52] Giulio Lorenzini and Natascia Mazza. *Debris flow: Phenomenology and rheological modelling*. Wit Press, 2004.

[53] Ning Lu, Jonathan W Godt, and David T Wu. “A closed-form equation for effective stress in unsaturated soil”. In: *Water Resources Research* 46.5 (2010).

[54] Ning Lu and William J Likos. “Origin of cohesion and its dependence on saturation for granular media”. In: *Poromechanics V: Proceedings of the Fifth Biot Conference on Poromechanics*. 2013, pp. 1669–1675.

[55] Ning Lu and William J Likos. “Suction stress characteristic curve for unsaturated soil”. In: *Journal of geotechnical and geoenvironmental engineering* 132.2 (2006), pp. 131–142.

[56] Ning Lu and William J Likos. *Unsaturated soil mechanics*. Wiley, 2004.

[57] A.P. Mainali and N. Rajaratnam. *Hydraulics of Debris Flows: A Review*. Technical report (University of Alberta. Department of Civil Engineering). University of Alberta, Department of Civil Engineering, 1991. URL: `https://books.google.com/books?id=NdALGwAACAAJ`.

[58] A Mangeney, Olivier Roche, O Hungr, N Mangold, G Faccanoni, and A Lucas. “Erosion and mobility in granular collapse over sloping beds”. In: *Journal of Geophysical Research: Earth Surface* 115.F3 (2010).

[59] Mikko Manninen, Veikko Taivassalo, Sirpa Kallio, et al. *On the mixture model for multiphase flow*. 1996.

[60] Xiannan Meng and Yongqi Wang. "Modelling and numerical simulation of two-phase debris flows". In: *Acta Geotechnica* 11.5 (2016), pp. 1027–1045.

[61] Xiannan Meng, Yongqi Wang, Chun Wang, and Jan-Thomas Fischer. "Modeling of unsaturated granular flows by a two-layer approach". In: *Acta Geotechnica* 12.3 (2017), pp. 677–701.

[62] Sabrina Meninno. "Mechanics of dry granular flows driven by gravity". PhD thesis. University of Trento, 2015.

[63] GDR MiDi. "On dense granular flows". In: *The European Physical Journal E* 14.4 (2004), pp. 341–365.

[64] D Naef, D Rickenmann, P Rutschmann, and BW McArdell. "Comparison of flow resistance relations for debris flows using a one-dimensional finite element simulation model". In: *Natural Hazards and Earth System Sciences* 6.1 (2006), pp. 155–165.

[65] Donald A Nield and Adrian Bejan. *Convection in porous media*. Vol. 3. Springer, 2006.

[66] OpenFOAM. *OpenFOAM: the open source CFD toolbox programmer's guide*. ESI-Group, 2012.

[67] Yavuz Ozeren, Rui Aleixo, Reza Marsooli, and Mustafa Altinakar. *Physical Properties of Artificial Sediments*. 2014.

[68] Yavuz Ozeren, Rui Aleixo, and Danial Wren. *The Influence of Gate Removal Time on Dam-Break Flow Characteristics*. 2014.

[69] Abani K Patra et al. "Parallel adaptive numerical simulation of dry avalanches over natural terrain". In: *Journal of Volcanology and Geothermal Research* 139.1-2 (2005), pp. 1–21.

[70] Thomas C Pierson and John E Costa. "A rheologic classification of subaerial sediment-water flows". In: *Debris flows/avalanches: process, recognition, and mitigation. Reviews in Engineering Geology* 7 (1987), pp. 1–12.

[71] E Bruce Pitman and Long Le. "A two-fluid model for avalanche and debris flows". In: *Philosophical Transactions of the Royal Society of London A: Mathematical, Physical and Engineering Sciences* 363.1832 (2005), pp. 1573–1601.

[72] Olivier Pouliquen and Yoel Forterre. "Friction law for dense granular flows: application to the motion of a mass down a rough inclined plane". In: *Journal of fluid mechanics* 453 (2002), pp. 133–151.

[73] Shiva P Pudasaini and Kolumban Hutter. "Rapid shear flows of dry granular masses down curved and twisted channels". In: *Journal of Fluid Mechanics* 495 (2003), pp. 193–208.

[74] Luc Rébillout, Yavuz Özeren, and Mustafa Altinakar. *Dam break experiments with granular material*. University of Mississippi, 2017.

[75] Lorenzo Adolph Richards. "Capillary conduction of liquids through porous mediums". In: *physics* 1.5 (1931), pp. 318–333.

[76] Mayte Rico, Gerardo Benito, and A Díez-Herrero. "Floods from tailings dam failures". In: *Journal of hazardous materials* 154.1-3 (2008), pp. 79–87.

[77] Henrik Rusche. "Computational fluid dynamics of dispersed two-phase flows at high phase fractions". PhD thesis. Imperial College London (University of London), 2002.

[78] Stuart B Savage, MH Babaei, and T Dabros. "Modeling gravitational collapse of rectangular granular piles in air and water". In: *Mechanics Research Communications* 56 (2014), pp. 1–10.

[79] Stuart B Savage and K Hutter. "The motion of a finite mass of granular material down a rough incline". In: *Journal of fluid mechanics* 199 (1989), pp. 177–215.

[80] Andrew Schofield and Peter Wroth. *Critical state soil mechanics.* Vol. 310. McGraw-Hill London, 1968.

[81] Carlotta Scudeler, Claudio Paniconi, Damiano Pasetto, and Mario Putti. "Examination of the seepage face boundary condition in subsurface and coupled surface/subsurface hydrological models". In: *Water Resources Research* 53.3 (2017), pp. 1799–1819.

[82] Karl Terzaghi. "The shearing resistance of saturated soils and the angle between the planes of shear". In: *First international conference on soil Mechanics, 1936.* Vol. 1. 1936, pp. 54–59.

[83] M Th Van Genuchten. "A closed-form equation for predicting the hydraulic conductivity of unsaturated soils 1". In: *Soil science society of America journal* 44.5 (1980), pp. 892–898.

[84] David J Varnes. "Landslide types and processes". In: *Landslides and engineering practice* 29.3 (1958), pp. 20–45.

[85] Liang Wang, Lian-Ping Wang, Zhaoli Guo, and Jianchun Mi. "Volume-averaged macroscopic equation for fluid flow in moving porous media". In: *International Journal of Heat and Mass Transfer* 82 (2015), pp. 357–368.

[86] S Watanabe. "Influence of the mixing ratio of water to sediment on the threshold slope of debris flows: a laboratory experiment". In: *Transactions, Japanese Geomorphological Union* 15 (1994), pp. 349–369.

[87] Henry G Weller, Gavin Tabor, Hrvoje Jasak, and Christer Fureby. "A tensorial approach to computational continuum mechanics using object-oriented techniques". In: *Computers in physics* 12.6 (1998), pp. 620–631.

[88] Xiaofan Yang, Zhongquan Charlie Zheng, Slawomir Winecki, and Steve Eckels. "Model simulation and experiments of flow and mass transport through a nano-material gas filter". In: *Applied Mathematical Modelling* 37.20-21 (2013), pp. 9052–9062.

[89] Zhouteng Ye, Xizeng Zhao, and Zhengzhi Deng. “Numerical investigation of the gate motion effect on a dam break flow”. In: *Journal of Marine Science and Technology* 21.4 (2016), pp. 579–591.

[90] Yueping Yin, Fawu Wang, and Ping Sun. “Landslide hazards triggered by the 2008 Wenchuan earthquake, Sichuan, China”. In: *Landslides* 6.2 (2009), pp. 139–152.

APPENDIX

A.1 The Cauchy stress tensor

In equation 4.16, the Cauchy stress tensor $\boldsymbol{\sigma}$ is introduced. This stress tensor consists of nine components that includes all stresses acting on the volume element dV. That means, shear and pressure forces because both can related to stresses. Relation between the total stress ($\boldsymbol{\sigma}$), shear-rate stress ($\boldsymbol{\tau}$) and pressure (p) is discussed here.

$$\boldsymbol{\sigma} = \begin{bmatrix} \sigma_{xx} & \sigma_{xy} & \sigma_{xz} \\ \sigma_{yx} & \sigma_{yy} & \sigma_{yz} \\ \sigma_{zx} & \sigma_{zy} & \sigma_{zz} \end{bmatrix} \tag{A.1}$$

The stress tensor σ can be split into a hydrostatic σ^{hyd} and deviatoric σ^{dev} part:

$$\boldsymbol{\sigma} = \boldsymbol{\sigma}^{hyd} + \boldsymbol{\sigma}^{dev} \tag{A.2}$$

The hydrostatic part is given by

$$-p\boldsymbol{I} = \boldsymbol{\sigma}^{hyd} = \frac{1}{3}\mathrm{tr}(\boldsymbol{\sigma})\boldsymbol{I} \tag{A.3}$$

where $\boldsymbol{I}$ is the identity matrix. The deviatoric part is given by

$$\boldsymbol{\tau} = \boldsymbol{\sigma}^{dev} = \boldsymbol{\sigma} - \frac{1}{3}\mathrm{tr}(\boldsymbol{\sigma})\boldsymbol{I} \tag{A.4}$$

Using the above definition, Equation A.2 can be rewritten:

$$\boldsymbol{\sigma} = -p\boldsymbol{I} + \boldsymbol{\tau} \tag{A.5}$$

The correct expression of $\boldsymbol{\tau}$ has to be chosen depending on the behavior of the fluid.

A.2 The shear-rate tensor

The shear-rate tensor is expressed by different equations depending on the behavior of the fluid. For Newtonian fluids, the nine components of the shear-rate tensor can be described as:

$$\tau_{xx} = -2\mu\frac{\partial u_x}{\partial x} + \left(\frac{2}{3}\mu - \kappa\right)(\bigtriangledown \cdot \boldsymbol{u}), \tag{A.6}$$

$$\tau_{yy} = -2\mu\frac{\partial u_y}{\partial y} + \left(\frac{2}{3}\mu - \kappa\right)(\bigtriangledown \cdot \boldsymbol{u}), \tag{A.7}$$

$$\tau_{zz} = -2\mu\frac{\partial u_z}{\partial z} + \left(\frac{2}{3}\mu - \kappa\right)(\bigtriangledown \cdot \boldsymbol{u}), \tag{A.8}$$

$$\tau_{xy} = \tau_{yx} = -\mu\left(\frac{\partial u_x}{\partial y} + \frac{\partial u_y}{\partial x}\right), \tag{A.9}$$

$$\tau_{yz} = \tau_{zy} = -\mu\left(\frac{\partial u_y}{\partial z} + \frac{\partial u_z}{\partial y}\right), \tag{A.10}$$

$$\tau_{zx} = \tau_{xz} = -\mu\left(\frac{\partial u_z}{\partial x} + \frac{\partial u_x}{\partial z}\right), \tag{A.11}$$

where the quantity κ is described by Bird et al. [7] as the bulk viscosity. Nevertheless, Bird et al. [7] mentioned that the quantity κ is not really important for dense gases and liquids and can be neglected.

By introducing the strain-rate tensor D,

$$\boldsymbol{D} = \frac{1}{2}[\bigtriangledown \boldsymbol{u} + (\bigtriangledown \boldsymbol{u})^T] \tag{A.12}$$

the shear-rate tensor can be defined as:

$$\boldsymbol{\tau} = 2\mu\boldsymbol{D} - \frac{2}{3}\mu(\bigtriangledown \cdot \boldsymbol{u})\boldsymbol{I}. \tag{A.13}$$

Derivation of Equation A.13 can be found in Holzmann [31]. The second term $(-\frac{2}{3}\mu(\bigtriangledown \cdot \boldsymbol{u}))$ in Equation A.13 represents expansion and compression phenomena. To demonstrate the meaning of this term and the correlation to both phenomena, the continuity equation is used to modified this equation. By using the product law, the continuity equation can be written as:

$$\triangledown \cdot \boldsymbol{u} = -\frac{1}{\rho}\left[\frac{\partial \rho}{\partial t} + \boldsymbol{u} \cdot \triangledown \rho\right]. \tag{A.14}$$

By substituting Equation A.14 into Equation A.13, the shear-rate tensor ($\boldsymbol{\tau}$) can be written as:

$$\boldsymbol{\tau} = 2\mu \boldsymbol{D} - \frac{2}{3}\mu \underbrace{\left\{ -\frac{1}{\rho}\left[\frac{\partial \rho}{\partial t} + \boldsymbol{u} \cdot \triangledown \rho\right]\right\}}_{\text{expansion and compression}} \boldsymbol{I}. \tag{A.15}$$

It can be clearly seen that the second term on the RHS is related to the density change. Thus, it is related to expansion and compression phenomena. If incompressible of fluid is assume, this term will vanish based on the fact that the density will not change during time and the gradient of a constant number is zero. The shear-rate tensor can be written as:

$$\boldsymbol{\tau} = 2\mu \boldsymbol{D}. \tag{A.16}$$

The expression of $\boldsymbol{\tau}$ in Equation A.16 is similar to that in Equation 4.17. The difference between the two equations is the viscosity. In Equation 4.17, the effective viscosity η_{eff} is used.

VITA

Education

- Ph.D. in Engineering Science.
  - National Center for Computational Hydroscience and Engineering (NCCHE), The University of Mississippi, MS, USA.
  - Dissertation title: A numerical study of granular dam-break flows.
- M.S. in Ocean Engineering.
  - Center for Applied Coastal Research (CACR), University of Delaware, DE, USA.
  - Thesis title: Parallel implementation of a 3D nonlinear wave model for random directional seas.
- B.Ed. in General Science and Mathematics.
  - Chulalongkorn University, Bangkok, Thailand.
  - Areas of emphasis: mathematics and general science.

Publications

- Mard Karlsson, J., A. Skelton, M. Sanden, M. Ioualalen, N. Kaewbanjak, N. Pophet, J. Asavanant, and A. von Matern, 2009, "Reconstructions of the coastal impact of the 2004 Indian Ocean tsunami in the Khao Lak area, Thailand," *J. Geophys. Res.*, 114, C10023, doi:10.1029/2009JC005516.
- Grilli, S. T., Dubosq, S., Pophet, N., Perignon, Y., Kirby, J. T. and Shi, F., 2010, "Numerical simulation and first-order hazard analysis of large co-seismic

tsunamis generated in the Puerto Rico trench: Near-field impact on the North shore of Puerto Rico and far-field impact on the US East Coast," *Nat. Haz. Earth Syst. Sci.*, 10, 2109-2125.

- Ioualalen, M., P. Arreaga-Vargas, N. Pophet, M. Chlieh, K. Ilayaraja, J. Ordonez, W. Renteria and N. Pazmino, 2010, "Numerical Modeling of the 26th December 2004 Indian Ocean Tsunami for the Southeastern Coast of India," *Pure Appl. Geophys.*, 167, 1205-1214.
- Pophet, N., Kaewbanjak, N., Asavanant, J. and Ioualalen, M., 2011, "High grid resolution and parallelized tsunami simulation with fully nonlinear Boussinesq equations," *Computer and Fluids*, 40(1), 258-268.
- Altinakar, M., Pophet, N., Chao, X. and Marsooli, R., 2018, "One-dimensional modeling of transport of coal ash in a river-reservoir system," *E3S Web of Conferences*, 40.
- Pophet, N., Altinakar, M. and Ozeren, Y., 2019, "Dam-break flows of water-granular mixtures: A numerical study," submitted to *SEDHYD 2019 Conference*, Nevada, June 24-28.